

R-matrix Analysis of CNO Cycle Reactions

Edward Charles Simpson

A dissertation submitted to the Department of Physics at the
University of Surrey in partial fulfilment of the degree of
Master in Physics.

Department of Physics
University of Surrey

April 22, 2006

Abstract

A multi-channel R-matrix code has been developed and used to analyse two key reactions in the CNO cycle. The $^{14}\text{N}(p,\gamma)^{15}\text{O}$ reaction determines the rate of operation of the CN cycle and is critical in determining the age of globular clusters, which give estimates for the age of the universe. The low energy S-factors determined are in good agreement with recent estimates. A preliminary analysis of the elastic scattering channel has shown that it may offer additional constraint on the radiative capture channels, though further analysis is required.

The $^{15}\text{N}(p,\gamma)^{16}\text{O}$ and $^{15}\text{N}(p,\alpha)^{12}\text{C}$ reactions are the branching point between the first and second CNO cycles and their relative reaction cross-sections determine the transit of catalytic material to higher cycles. The (p,α) astrophysical S-factor found is in very good agreement with recent estimates, but the (p,γ) low energy S-factor is found to be lower than the most recently reported values.

Acknowledgements

I would like to acknowledge the guidance of Prof. R. E. Azuma, without which this project would not have been possible. I'd also like to thank my supervisors Prof. M. Wiescher, Prof. J. Tostevin and Dr. P. H. Regan and thank Dr. H. -P. Trautvetter, Prof. A. Champagne, P. Bertone, H. Costantini, P. J. LeBlanc and C. Ugalde for their assistance.

Contents

1	Theoretical background	2
1.1	Hydrogen burning in main sequence stars	2
1.1.1	Proton-proton fusion	2
1.1.2	The CNO cycle	4
1.2	Reaction rate, cross-section and S-factor	7
1.3	Breit-Wigner cross-section formula	12
1.4	R-matrix theory	13
1.4.1	Overview	13
1.4.2	Internal wavefunctions	15
1.4.3	External wavefunctions	17
1.4.4	The W-matrix	19
1.4.5	The T-matrix	21
1.4.6	The A-matrix	23
1.4.7	Alternative parameterization of R-matrix theory	23
1.5	Direct reaction theories	23
1.5.1	Barker and Kajino nonresonant channel contributions	24
1.5.2	Angulo and Descouvemont direct capture	25
2	The AZURE R-matrix code	28
2.1	Program structure	28
2.1.1	Subroutine files	30
2.1.2	Configuration and input files	31
2.2	Code concepts	33
2.2.1	Reaction pathways	33
2.2.2	Background poles	34
2.3	Development of the code	34
2.3.1	Longform input code	34
2.3.2	Output code	36
2.3.3	Changes to <code>segmentcontrol.dat</code> and <code>testlimits.dat</code>	36
3	Nonresonant contribution development code	38
3.1	Energy dependence of nonresonant channel contributions	38
3.1.1	Whittaker functions for various binding energies	39
3.1.2	Energy dependence	39

4	$^{14}\text{N}(\text{p},\gamma)^{15}\text{O}$ reactions	45
4.1	Summary of experimental measurements	45
4.1.1	^{15}O compound nucleus	45
4.1.2	Experimental measurements	46
4.1.3	Previous analysis	48
4.2	R-matrix analysis	52
4.2.1	The ground state and 6.18 MeV transitions	52
4.2.2	The 6.79 MeV transition	58
4.2.3	Elastic scattering	60
4.3	Comparisons of results	64
4.3.1	Comparison of fitted $S(0)$ values	64
4.4	Further constraints	65
4.4.1	Subthreshold state lifetime measurements	65
4.4.2	Total cross-section measurements	66
4.4.3	Elastic scattering data	66
4.5	Conclusions and astrophysical implications	67
5	$^{15}\text{N}(\text{p},\gamma)^{16}\text{O}$ and $^{15}\text{N}(\text{p},\alpha)^{12}\text{C}$ reactions	70
5.1	Summary of experimental measurements	70
5.1.1	The ^{16}O compound nucleus	70
5.1.2	Experimental measurements	71
5.1.3	Previous analysis	72
5.2	R-matrix analysis	74
5.2.1	Identifying the correct minimum	74
5.2.2	$S(0)$ estimates	78
5.3	Comparison of extrapolated $S(0)$	82
5.4	Conclusions and astrophysical implications	85
A	Corrections to Lane and Thomas R-matrix theory	89
A.1	C. Ugalde	89
A.2	L. Buchmann	89
B	NuclearInput.for	91
C	BarkerKajino.for	95
D	Tables of fitted parameters	98

Introduction

The cross-sections of hydrogen burning reactions at the energies relevant to stellar environments are typically very small. Consequently they are very difficult to measure. To make accurate estimates of the cross-sections at energies relevant to nuclear astrophysics, we must make extrapolations to low energies based on higher energy data. We develop and use theoretical frameworks to describe nuclear reactions, allowing us to calculate cross-sections in the energy range of interest.

R-matrix theory is a well established-method of calculating cross-sections for resonance reactions. A new R-matrix computer code (AZURE) has been written and is designed to be easily applied to a wide variety of reactions of interest in nuclear astrophysics. It is capable of analysing all scattering, particle and γ -channels simultaneously, which can improve the reliability of the calculations. The development of this code and demonstration of its reliability forms a part of this dissertation.

The CNO cycle is the dominant hydrogen burning process in larger stars. Two critical reactions are the rate determining reaction and the reactions which determine the transit of catalytic material to higher cycles. The application of the AZURE code to these well known problems has been an excellent test of the code and a good demonstration of the benefits multi-channel analysis. This analysis has motivated the next stage of development of the code and helped guide the next generation of experiments on the relevant reactions.

Chapter 1

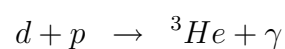
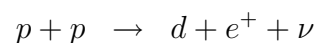
Theoretical background

1.1 Hydrogen burning in main sequence stars

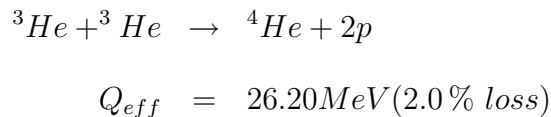
Main sequence stars produce energy by burning hydrogen to form helium. The reaction sequence by which this occurs depends on the temperature, density and initial composition of the star. Smaller stars burn hydrogen through proton-proton fusion, which proceeds very slowly. Larger stars have higher temperatures and, provided catalytic material is available, burn hydrogen through the CNO cycle.

1.1.1 Proton-proton fusion

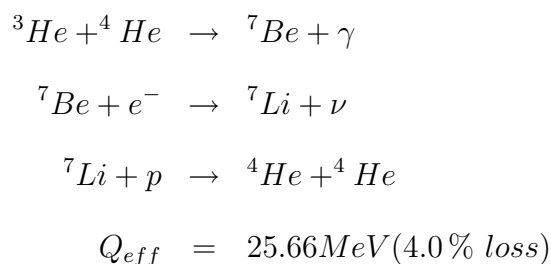
Proton-proton fusion is the principal process for burning hydrogen for stars with mass $< 1.5M_{\odot}$. The reaction chain begins with two protons fusing and a simultaneous β decay to form a deuteron nucleus. The weak reaction to form deuteron is the slowest step in the proton-proton fusion chain. The deuteron then fuses with another proton to form ${}^3\text{He}$.



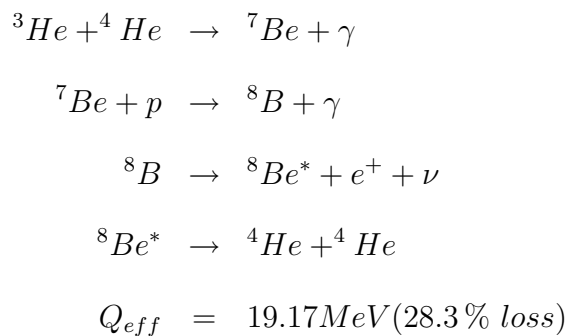
Once ${}^3\text{He}$ has been formed three different reaction chains are thought to produce ${}^4\text{He}$. The first chain is reported to occur 86% of the time and so dominates the energy production. Two ${}^3\text{He}$ nuclei fuse to form ${}^4\text{He}$ and two protons:



The second chain occurs $\sim 14\%$ of the time and requires ${}^4\text{He}$ to act as a catalyst.



The third chain occurs only 0.02% of the time and again requires ${}^4\text{He}$ as a catalyst.



The rate of operation of each chain depends the density, temperature and chemical composition of the star, though the second and third chains require ${}^4\text{He}$ to act as a catalyst. Each of the chains produces the same amount of energy (26.73 MeV), but the energy of the neutrinos produced cannot be retained in the star and so is effectively lost. The energy carried away by the neutrinos is different for each reaction chain, so the net energy released Q_{eff} varies.

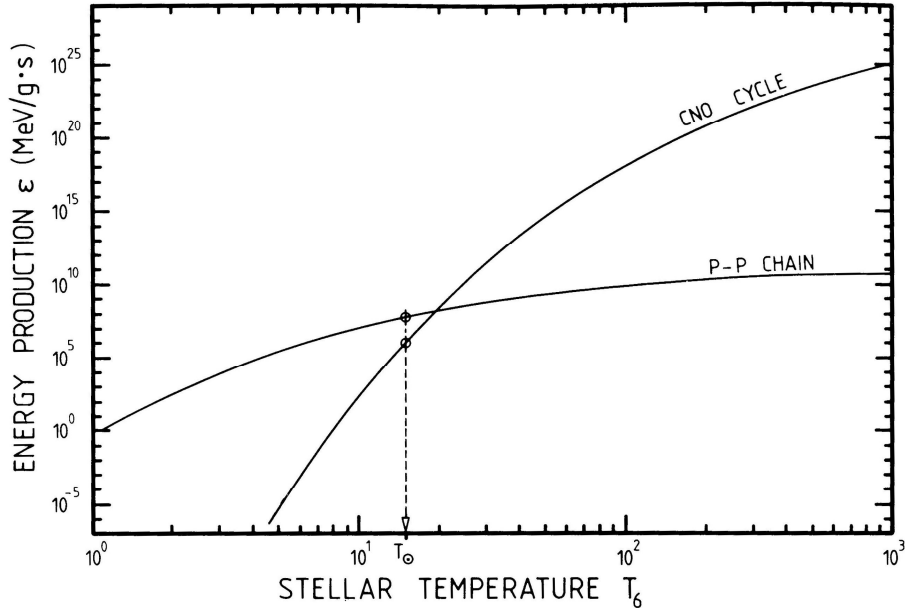


Figure 1.1: Comparison of the reaction rates of proton-proton fusion and the CNO cycle (taken from Ref. [1]). The CNO reaction rate increases more quickly with temperature than the p-p fusion rate and dominates above $T=20\times 10^6\text{K}$.

1.1.2 The CNO cycle

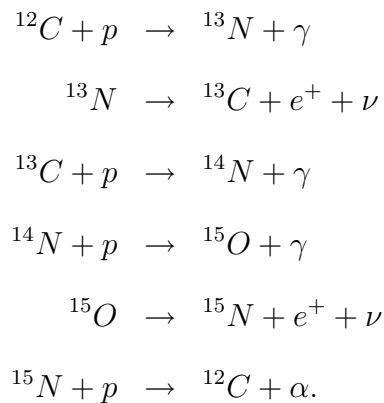
The CNO cycle is an alternative method of burning hydrogen to form helium and is the dominant process of hydrogen burning in stars of mass $>1.5M_{\odot}$. It uses carbon to catalyse the burning of hydrogen, through a series of proton captures and beta decays. The process is more sensitive to temperature than proton-proton fusion; the p-p fusion rate varies as T^4 for stars of mass $\sim 1.5M_{\odot}$, whereas the CNO cycle varies as T^{17} (Ref [1])! A comparison of the rates of the CNO cycle and proton-proton fusion is shown in Fig. 1.1.

Whilst the CNO does not proceed by the weak interaction as the proton-proton chain does, the rate of the reaction is not higher than the p-p chain at all temperatures as one might expect. This is due to the Coulomb barrier, which is much higher for carbon than it is for hydrogen. The probability of an incident particle tunnelling through this barrier is related to the height of the barrier, determined by the charge and relative energy of the nuclides, the latter being related to the temperature.

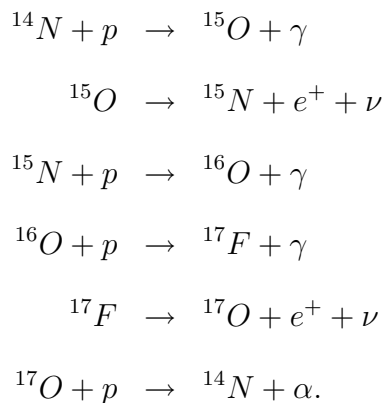
Stars require the catalysts to be present in their initial composition for CNO burn-

ing to occur, regardless of the size and temperature of the star. First generation stars contained only primordial hydrogen and helium, but produced heavier elements which were then ejected into the interstellar medium at the end of the stars lives. Gradually the initial composition of new stars becomes metal-enriched, allowing CNO burning to occur more readily. It is also important to know how much catalytic material will be lost from the CNO cycle during main sequence burning, as it cannot be replenished. This may affect the hydrogen burning processes as stars age.

The first CNO (or CN) cycle was proposed by Bethe and von Weizsäcker in the late 1930s and is commonly envisaged as a chain of reactions, starting and ending with ^{12}C :



Later it was realised that other cycles were possible, using a variety of heavier isotopes as catalysts. The second cycle is often thought of as a chain of reactions beginning and ending with ^{14}N :



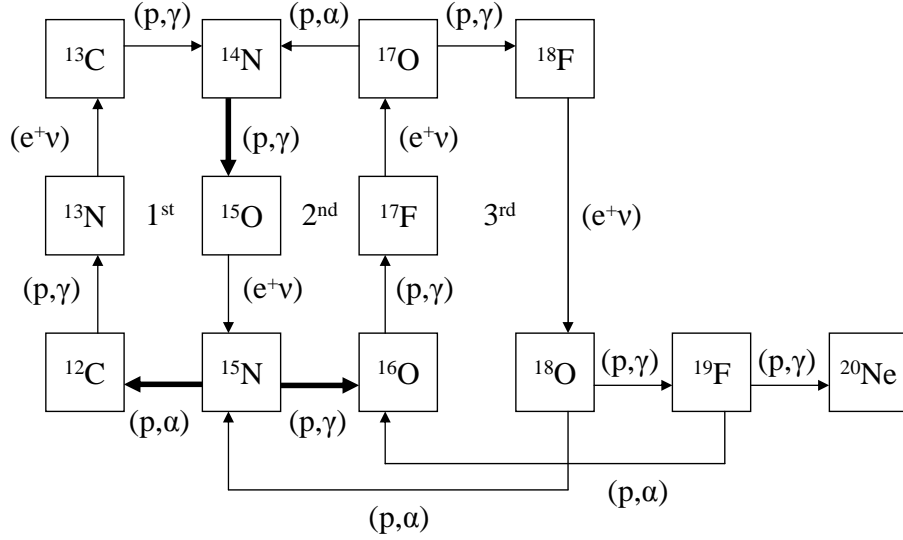


Figure 1.2: The first, second and third CNO Cycles. The reactions studied here are highlighted by bold arrows.

The first, second and third CNO cycles are illustrated in Fig 1.2. The net energy retained in the stellar interior from the first cycle is 26.73MeV, which compares to <26.20MeV for the proton-proton fusion process, though both processes have the net result, shown in Eq. 1.1. This is because the neutrinos in proton-proton fusion are of higher energy than those in the CNO cycle, so more energy is lost from the stellar interior.

$$4p \rightarrow {}^4\text{He} + 2e^+ + 2\nu + Q_{eff}. \quad (1.1)$$

The ${}^{14}\text{N}(p,\gamma){}^{15}\text{O}$ Reaction

The slowest reaction in the first CNO cycle is ${}^{14}\text{N}(p,\gamma){}^{15}\text{O}$. It determines the rate of the first CNO cycle and, as most catalytic material remains in the first cycle, it determines the overall energy production of CNO burning.

The most significant contributions to the cross-section come from the transitions to the 6.79 MeV $3/2^+$ state, the $1/2^-$ ground state and the 6.18 $3/2^-$ state. The largest contribution is thought to come from the transition to the 6.79 MeV state.

As the ${}^{14}\text{N}(p,\gamma){}^{15}\text{O}$ reaction is the slowest in the CNO cycle, the majority of catalytic material during CNO burning is in the form of ${}^{14}\text{N}$. Typically, at the start of hydrogen

CNO burning, the catalytic material is in the form of ^{12}C and ^{16}O from helium burning in previous generations of stars (see Ref. [1]).

The $^{15}\text{N}(\text{p},\gamma)^{16}\text{O}$ and $^{15}\text{N}(\text{p},\alpha_0)^{12}\text{C}$ Reactions

The $^{15}\text{N}(\text{p},\gamma)^{16}\text{O}$ reaction is the branching point between the first and second CNO cycles. The ratio of the (p,γ) and (p,α_0) reactions determines the amount of catalytic material that is available to the higher cycles. The ratio is reported to be about 1000:1, meaning that the first cycle occurs 1000 times for every time the second cycle occurs (see Ref. [1]). Clearly this means that the vast majority of energy production comes from the first cycle, highlighting the importance of the $^{14}\text{N}(\text{p},\gamma)^{15}\text{O}$ reaction.

The $^{15}\text{N}(\text{p},\alpha_1)^{12}\text{C}$ reaction has been measured experimentally and has been found to contribute negligibly to the total $^{15}\text{N}(\text{p},\alpha)^{12}\text{C}$ cross-section.

The higher CNO cycles are important to the nucleosynthesis of elements up to ^{23}Na , particularly ^{16}O and ^{17}O (Ref. [1]). The more catalytic material that is available to these cycles, the greater the production of these heavier elements. As it is possible for catalytic material to be lost from higher CNO cycles, then the more catalytic material in these cycles, the greater the rate of loss. This might affect the evolution of a star through the main sequence, as the CNO energy production rate could fall as the star ages due to loss of catalytic material.

1.2 Reaction rate, cross-section and S-factor

The reaction rate is related to the reaction cross-section σ , which can be measured experimentally. The cross-section is essentially a measure of reaction probability and is classically thought of as the literal cross-sectional area of the target nucleus. However, it is hard to accurately measure some of the cross-sections relevant to stellar burning, as they are extremely small at low energies. Let us consider the reaction between a charged projectile and a charged target. For the reaction to take place the projectile must pene-

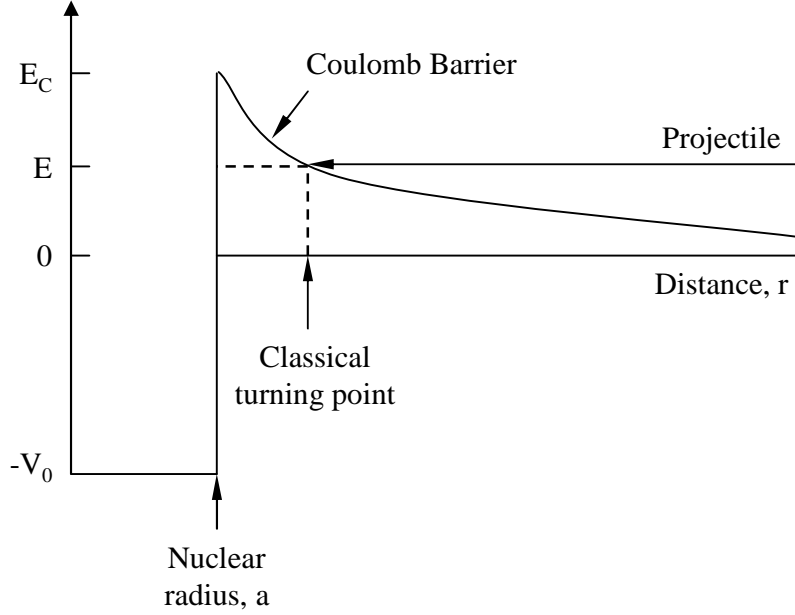


Figure 1.3: Sketch of the Coulomb barrier. Classically, if the projectile has energy less than E_C , the Coulomb barrier height, it is turned away at the classical turning point. However, it is possible for a projectile of $E < E_C$ to quantum mechanically tunnel through the Coulomb barrier. The higher the energy of the projectile, the higher the tunnelling probability. Adapted from Figure 4.2 Ref. [1].

trate the Coulomb barrier of the target nucleus. The Coulomb potential has the form of Eq. 1.2 and is illustrated in Fig. 1.3.

$$V_C(r) = \frac{Z_1 Z_2 e^2}{r}. \quad (1.2)$$

The Coulomb barrier height is related to the charges of projectile and target nuclides, so burning involving higher Z nuclides requires higher energies and so higher temperatures. A particle will very rarely have an energy greater than the Coulomb barrier, so most reactions would be classically forbidden. However the projectile is allowed in quantum mechanics to tunnel through the barrier and react, even though its energy is less than the Coulomb barrier. The rate of reaction per particle pair $\langle \sigma v \rangle$ is given by Eq. 1.3,

$$\langle \sigma v \rangle = \left(\frac{8}{\pi \mu} \right)^{1/2} \frac{1}{(kT)^{3/2}} \int_0^\infty \sigma(E) E \exp\left(-\frac{E}{kT}\right) dE, \quad (1.3)$$

where k is the Stefan-Boltzmann constant, T is the temperature, E is the centre-of-mass

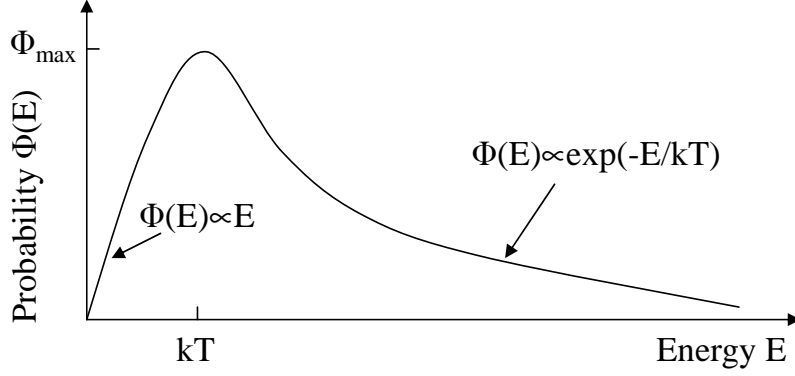


Figure 1.4: Schematic of the Maxwell-Boltzmann distribution. The peak occurs at $E=kT$, so the higher the temperature, the higher the average energy. Adapted from Figure 3.2 Ref. [1].

energy of the particles given by Eq. 1.4 and μ is the reduced mass given by Eq. 1.5.

$$E = \frac{1}{2}\mu v^2. \quad (1.4)$$

$$\mu = \frac{M_1 M_2}{M_1 + M_2}. \quad (1.5)$$

M_1 and M_2 are the masses of particles 1 and 2 respectively and v is the relative velocity between the interacting nuclei. The particles within the star have a distribution of velocities, related to the temperature. The distribution is of Maxwell-Boltzmann form, illustrated in Fig 1.4.

Essentially, the reaction rate per particle pair is the probability σ that a particle pair of energy E will react, multiplied by the probability of a particle having that energy, given by the Maxwell-Boltzmann distribution, multiplied by the energy of the particles, integrated over all energies.

The energy dependence of the cross-section for charged particle reactions is dominated by the penetrability, which is related to the probability of tunnelling through the Coulomb barrier. It causes the cross-section to fall very rapidly at low energies. The cross-section may vary by two orders of magnitude for particle energies between 0.5 and 4 MeV, but by eight orders of magnitude between 0.05 and 0.5 MeV. The S-factor $S(E)$ removes

much of this energy dependence, by taking out the entrance channel penetrability for two particles in a relative s-state ($l = 0$). An example of this is shown in Fig. 1.5. Note that S-factors are used purely for convenience and have no physical significance. The S-factor is defined by Eq. 1.6 (see Ref. [1]),

$$\sigma(E) = \frac{1}{E} \exp(-2\pi\eta) S(E), \quad (1.6)$$

where $\sigma(E)$ is the angle-integrated cross section and E is the centre-of-mass energy of the system. The quantity η is called the Sommerfeld parameter, given by Eq. 1.7 (Ref. [1], Ref. [2] pg.267),

$$\eta = \frac{Z_1 Z_2 e^2}{\hbar v}, \quad (1.7)$$

where Z_1 and Z_2 are the numbers of protons in the two particles, e is the charge of an electron and \hbar is Planks constant divided by 2π . Here, v is the relative velocity, given by Eq. 1.8 (Ref. [2] pg.267):

$$v = \hbar k / \mu \quad (1.8)$$

where k is the wave number given by Eq. 1.9

$$k = \left(\frac{2\mu|E|}{\hbar^2} \right)^{1/2}. \quad (1.9)$$

At low energies the Coulomb barrier penetrability can be approximated by Eq. 1.10.

$$P \approx \exp(-2\pi\eta). \quad (1.10)$$

We also note that the S-factor only offers an approximation to the entrance channel Coulomb barrier penetrability. The penetration through the angular momentum barrier is not included in this approximation, which would affect reactions with $l \neq 0$.

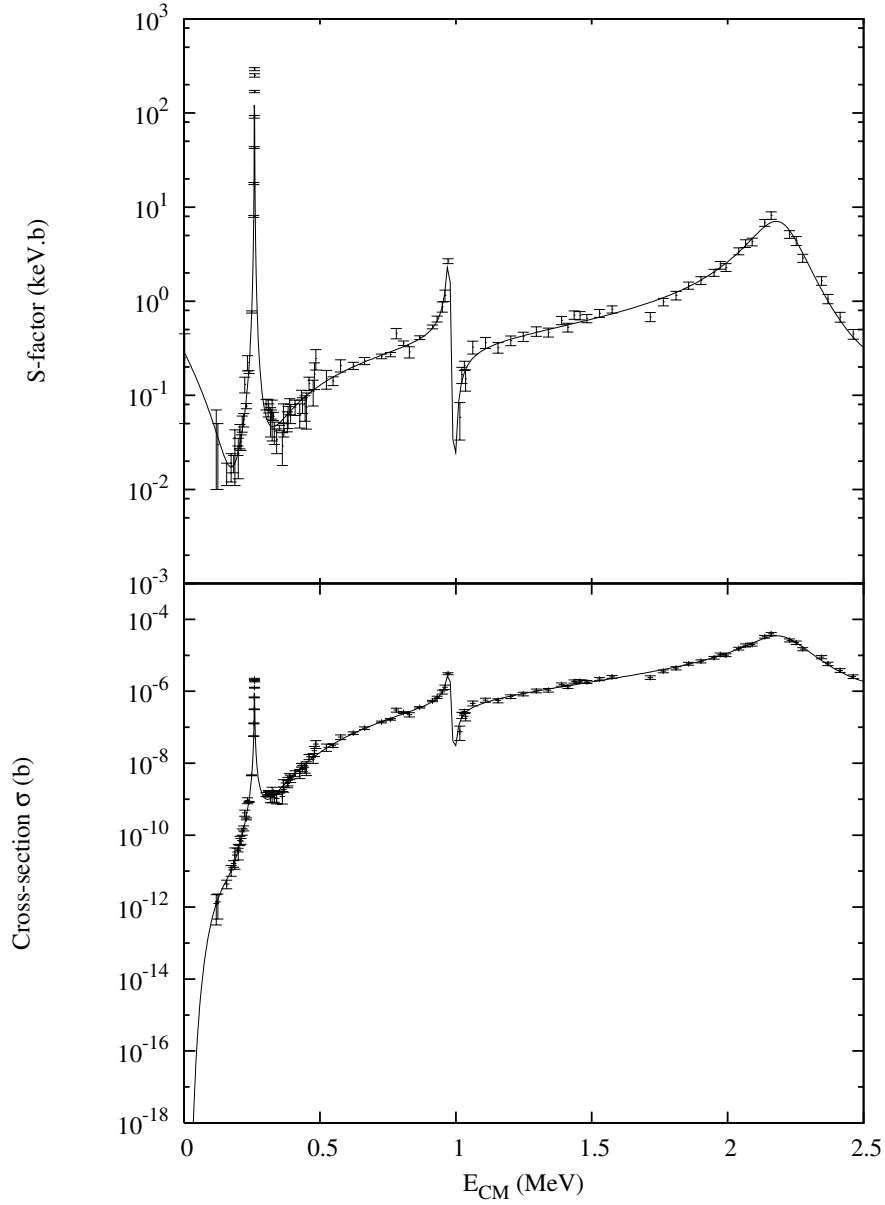


Figure 1.5: Comparison of the cross-section and S-factor for the $^{14}\text{N}(p, \gamma_{g.s.})^{15}\text{O}$ reaction. The cross-section varies by more than ten orders of magnitude over the whole energy range, whereas the S-factor varies by just four orders of magnitude. Note that the cross-section falls by many orders of magnitude below 0.2 MeV, which is the region of interest for nuclear astrophysics.

1.3 Breit-Wigner cross-section formula

The Breit-Wigner formula gives a first description of resonance reactions, using a simple compound nucleus mechanism. A projectile a is incident on a target A . The two form a compound nucleus C in an excited or ‘resonant’ state, which decays into final particles b and B , where b is projectile-like and B is target-like. This is illustrated in Fig. 1.6.

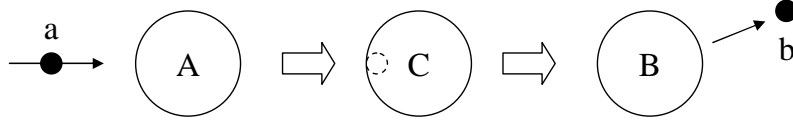


Figure 1.6: A simple compound nucleus reaction.

For the reaction $A+a\rightarrow C\rightarrow B+b$, the Breit-Wigner, angle integrated cross section for a single resonance is given by Eq. 1.11 (see Refs. [3] and [1]),

$$\sigma(E) = \pi\lambda^2 \frac{2J+1}{(2J_a+1)(2J_A+1)} (1 + \delta_{Aa}) \frac{\Gamma_a(E)\Gamma_b(E)}{(E - E_R)^2 + (\Gamma(E)/2)^2}, \quad (1.11)$$

where J is the angular momentum of the compound state, J_a and J_A are the spins of particles a and A respectively, δ_{Aa} is a Kronecker delta which corrects the expression for cases of identical particles, E is the projectile energy and E_R is the energy of the resonance in question in the centre-of-mass system. $\pi\lambda^2$ is the geometric cross-section (Eq. 1.12) and, except for statistical effects, gives the maximum possible value for the cross-section.

$$\pi\lambda^2 = \frac{656.6}{\mu E} \text{ barns}, \quad (1.12)$$

The experimental partial widths $\Gamma_a(E)$ and $\Gamma_b(E)$, and the total experimental width $\Gamma(E)=\Gamma_a(E)+\Gamma_b(E)$ vary with energy. They are related to the reduced width amplitudes γ by the penetrability P (Eq. 1.13).

$$\Gamma = 2P\gamma^2. \quad (1.13)$$

The Breit-Wigner equation can give an accurate description of the cross-section for several resonances providing that they are well isolated (i.e. the energy between them is greater than their widths), by simply summing the contributions. Interference effects can be taken into account. However in situations with broader resonances the Breit-Wigner equation works less well.

The experimental partial width for γ -ray emission Γ_γ is connected to the lifetime of the state in question by Eq. 1.14. Measurements of the lifetimes τ of states place constraints on the Γ_γ width (see for example Ref. [4]).

$$\tau = \frac{\hbar}{\Gamma_\gamma} \tag{1.14}$$

1.4 R-matrix theory

1.4.1 Overview

The R-matrix theory was first proposed by Wigner in 1941 and is detailed in depth in the encyclopaedic review paper by Lane and Thomas (Ref. [2], referred to as LT). The derivations described here follow those of Lane and Thomas and of E. W. Vogt (Ref. [5], referred to as EV).

Consider an incident particle a on target A . These two particles are the initial particle pair, denoted by α . The incident particle and target nucleus form a compound nucleus, which then decays into various final states, b and B . This final particle pair is denoted by α' .

As an example, we consider reactions involving a proton incident on a ^{15}N target. Figure 1.7 gives an illustration. The proton and nitrogen spins couple to channel spin s and have relative angular momentum l . This is the entrance channel. In a similar way the particles in the exit channel couple to channel spin s' and have relative orbital angular momentum l' .

The proton and ^{15}N target form a compound (excited) state of ^{16}O , which then decays

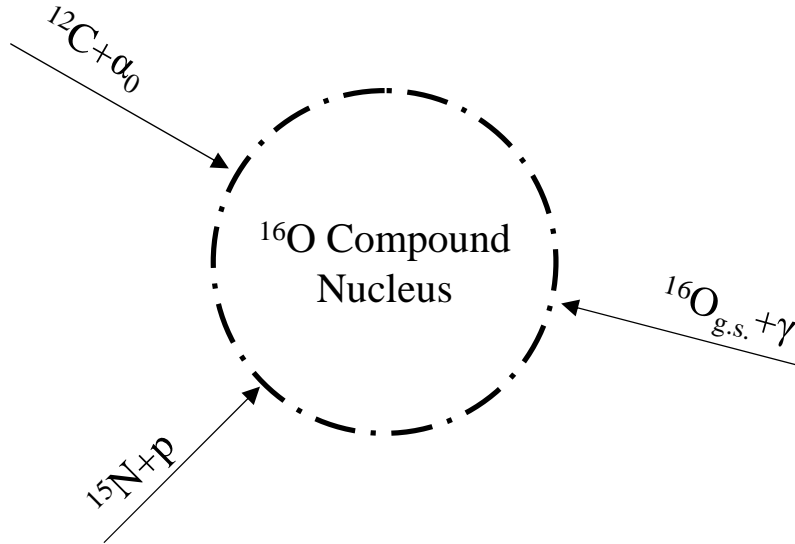


Figure 1.7: The ^{16}O compound nucleus and the relevant channels.

into one of several exit channels, emitting a photon to form ^{16}O in the ground state, or emitting an α particle to form ^{12}C for example. One can consider elastic scattering as the absorption of an incident particle to form a compound nucleus, and the re-emission of the incident particle. The α , s and l indices are often abbreviated by a channel index c , such that $c \equiv [\alpha sl]$.

Note that due to the symmetry of the matrices involved, each final particle pair α' can be treated as an initial particle pair α . In most cases we only consider a single initial particle pair.

Critical to R-matrix theory is the channel radius a . This radius represents a division between the internal region, where we consider only the short range nuclear force and where the nuclear potential has an effect, and the external region, outside the nuclear potential, where we assume no strong nuclear interactions take place between the two particles. To begin the discussion of the theory, we first consider the internal (within the channel radius) and external (outside the channel radius) wavefunctions.

1.4.2 Internal wavefunctions

The total wavefunction for the internal region, Ψ_{JM} , satisfies the wave equation Eq. 1.15 (LT pg.270 eq.3.1, EV pg.731 eq.33)

$$\hat{H}\Psi_{JM} = E\Psi_{JM}, \quad (1.15)$$

where \hat{H} is the Hamiltonian of the system and E the total energy of the system. Ψ_{JM} can be expanded in terms of a mutually orthonormal set of eigenfunctions, $X_{\lambda JM}$, defined in the internal region, Eq. 1.16 (LT pg.270 eq.3.2, EV pg.731 eq.36) .

$$\Psi_{JM} = \sum_{\lambda} C_{\lambda J} X_{\lambda JM}. \quad (1.16)$$

The eigenfunctions also satisfy the wave equation Eq. 1.17 (LT pg.270 eq.2.2, EV pg.731 eq.34),

$$\hat{H}X_{JM\lambda} = E_{\lambda}X_{JM\lambda}. \quad (1.17)$$

To give some intuitive physical meaning to the eigenvalues E_{λ} of the internal region, we arbitrarily associate the lowest energy eigenfunctions with energy levels in the compound nucleus. However, there are an infinite number of such eigenfunctions and to accurately calculate the cross-section, we must include all levels in the compound nucleus to take account of all the possible eigenfunctions. This would be computationally impossible, so in practice we include all the levels in the energy range of interest and add a background resonance for each of the relevant spin-parity J^{π} groups to simulate the tails of the higher energy resonances.

The coefficients C_{λ} are given by Eq. 1.18 (EV pg.731 eq.37), where the integration is over the whole internal volume.

$$C_{\lambda} = \int X_{\lambda}^* \Psi dV. \quad (1.18)$$

We impose the boundary condition (Eq. 1.19) which must be satisfied on the nuclear surface at the channel radius a_c (EV pg.731 eq.35),

$$r_c \frac{dX_\lambda}{dr_c} = b_c X_\lambda. \quad (1.19)$$

We then multiply the complex conjugate of Eq. 1.15 by Ψ , Eq. 1.17 by X_λ^* , subtract and integrate over the nuclear volume. Using Green's theorem we can convert the volume integral to an integral over the containing nuclear surface. The external wavefunction can be described by Eq. 1.20 (EV pg.729 eq.27),

$$\Psi = \sum_c \psi_c \phi_c, \quad (1.20)$$

where ψ_c is the channel wavefunction and ϕ_c is a radial wavefunction. Making use of the imposed boundary condition Eq. 1.19 and Eq. 1.20 gives Eq. 1.21 (EV pg.731 eq.38),

$$\begin{aligned} (E_\lambda - E) \int_V X_\lambda^* \Psi dV &= \sum_c \int_{S_c} \left(\frac{\hbar^2}{2m_c r_c} \right) \times [X_\lambda^* \Psi' - \Psi X_\lambda'^*] dS_c \\ &= \sum_c \frac{\hbar^2}{2m_c r_c} \gamma_{\lambda c} (\phi_c' - b_c \phi_c), \end{aligned} \quad (1.21)$$

where primes indicate logarithmic derivatives and $\gamma_{\lambda c}$ are the reduced width amplitudes given by Eq. 1.22 (LT pg.271 eq.4.8a, EV pg.731 eq.39), where the integral is now over the internal/external dividing surface,

$$\gamma_{\lambda c} \equiv \left(\frac{\hbar^2}{2m_c r_c} \right)^{1/2} \int \phi_c^* X_\lambda dS. \quad (1.22)$$

The reduced width amplitude is the overlap integral of the internal eigenfunction X_λ and the external radial wavefunction over the nuclear surface. In a sense it is how much the internal eigenfunction, associated with a resonant state, 'looks like' the external wavefunction at the nuclear surface. If the compound system looks like the particles in the channel the reduced width amplitude is large, so the resonance will be stronger, giving

a larger cross-section.

The coefficients C_λ are given by Eq. 1.23 (EV pg.731 eq.40).

$$C_\lambda = (E_\lambda - E)^{-1} \sum_c \gamma_{\lambda c} (\phi'_c - b_c \phi_c) (\hbar^2/2m_c r_c)^{1/2}. \quad (1.23)$$

Using this value of C_λ in Eq. 1.17 and evaluating Eq. 1.17 over the nuclear surface, we obtain Eq. 1.24 (EV pg.731 eq.41),

$$(\hbar/2m_c r_c)^{1/2} \phi_c = \sum_{c'} R_{cc'} [\phi'_{c'} - b_{c'} \phi_{c'}] \times (\hbar/2m_{c'} r_{c'})^{1/2}, \quad (1.24)$$

where the $R_{cc'}$ are the R-matrix elements given by Eq. 1.25 (LT pg.283 eq.2.8a, EV pg.731 eq.42).

$$R_{cc'} = \sum_\lambda \frac{\gamma_{\lambda c} \gamma_{\lambda c'}}{E_\lambda - E}. \quad (1.25)$$

Here E is the energy of the particles and E_λ is the energy eigenvalue, associated with an energy level in the compound nucleus. To calculate the reaction cross-section, we must derive an expression for the channel wavefunction in the external region ϕ_c .

1.4.3 External wavefunctions

We can write the radial wave function in terms of incoming and outgoing waves, giving the full external wavefunction Eq. 1.20 as Eq. 1.26 (EV pg.731 eq.43). We note that this equation may contain a typographical error; the $-1/2$ should be superscript. The factor ' $\nu^{-1/2}$ ' is referred to later on EV pg.731.

$$\Psi = \sum_c (1/v_c)^{1/2} (A_c I_c - B_c O_c) \psi_c \quad (1.26)$$

The incoming and outgoing wavefunctions have the asymptotic behaviour of Eq. 1.27 (LT pg.269 eq.2.10b, EV pg.731 eq.44).

$$I_c^* = O_c \approx \exp[i(k_c r_c - \frac{1}{2}l_c \pi - \eta_c \ln 2k_c r_c)] \quad (1.27)$$

It is convenient to express the incoming and outgoing wavefunctions for positive energy channels in terms of regular F and irregular G wavefunctions Eq. 1.28 (LT pg.269 eq.2.13a eq.2.13b).

$$\begin{aligned} I_c^+ &= (G_c - iF_c)\exp(i\omega_c) \\ O_c^+ &= (G_c + iF_c)\exp(-i\omega_c) \end{aligned} \quad (1.28)$$

If we consider the completely general external wavefunction Eq. 1.26, we can connect the coefficients of the incoming and outgoing wavefunctions A and B using the collision matrix, or U-matrix. This gives Eq. 1.29 (EV pg.731 eq.46),

$$B_c = \sum_{c'} U_{cc'} A_{c'}. \quad (1.29)$$

Using Eq. 1.29 in Eq. 1.26, multiplying by ϕ_c^* and integrating over the nuclear surface S , we obtain Eq. 1.30 (EV pg.731 eq.47), the radial wavefunction in terms of the collision matrix.

$$\phi_c = v_c^{1/2} (A_c I_c - \sum_{c'} U_{cc'} A_{c'} O_{c'}) \quad (1.30)$$

Taking the derivative of Eq. 1.30 and matching it and the value of ϕ_c to that of Eq. 1.24, we get Eq. 1.31 which connects the U-matrix to the nuclear parameters (i.e. the γ reduced width amplitudes and level energies) through the R-matrix (LT pg.289 eq.1.5, EV pg.732 eq.48).

$$U = (kr)^{1/2} O^{-1} (1 - RL)^{-1} (1 - RL^*) I (kr)^{-1/2} \quad (1.31)$$

The cross-section can be calculated from the U-matrix.

1.4.4 The W-matrix

The W-matrix is a convenient way to calculate the U-matrix and is used in AZURE. It relates to the U-matrix by Eq. 1.32 (LT pg.289, eq.1.5). Here, bold quantities are channel-matrices.

$$\mathbf{U}^J = \mathbf{\Omega} \mathbf{W}^J \mathbf{\Omega}. \quad (1.32)$$

The W-matrix is calculated by Eq. 1.33 (LT pg.289, eq.1.6a),

$$\mathbf{W}^J = \mathbf{1} + \mathfrak{B}^{\frac{1}{2}} (\mathbf{1} - \mathbf{R}^J \mathbf{L}^0)^{-1} \mathbf{R}^J \mathfrak{B}^{\frac{1}{2}} \mathbf{w}. \quad (1.33)$$

w is the Wronskian of the Coulomb wavefunctions (equal to $2i$ for positive energy channels, LT pg.271 eq.4.7c). L^0 is given by Eq. 1.34 and is a surface diagonal matrix, connected to the surface diagonal matrices L_c , the logarithmic derivative of the O -type wavefunction given by Eq. 1.35 (LT pg.289 eq.1.6a) and B_c the boundary condition matrix (Eq. 1.36).

$$L_c^0 = L_c - B_c \quad (1.34)$$

$$L_c \equiv (\rho_c O'_c / O_c)_{r_c = a_c} = S_c + iP_c \quad (1.35)$$

$$B_c = \frac{D_{\lambda c}}{V_{\lambda c}} \quad (1.36)$$

$V_{\lambda c} \equiv \gamma_{\lambda c}$ (referred to as the value function, LT pg.271 eq.4.8a) and $D_{\lambda c}$ (referred to as the derivative function, LT pg.271 eq.4.8b) is given by Eq. 1.37.

$$D_{\lambda c} = \gamma_{\lambda c} + (a_c \hbar^2 / 2M_c)^{1/2} \int \phi_c^* \nabla_n X_{\lambda JM} dS. \quad (1.37)$$

The logarithmic derivative L_c can be split into real shift S and imaginary penetrability P parts, which are given for positive energy channels by Eq. 1.38 and Eq. 1.39 (LT pg.271

eq.4.4a eq.4.4b, EV pg.732 eq.58).

$$S_c^+ = \left[\rho_c \frac{(F_c F_c' + G_c G_c')}{F_c^2 + G_c^2} \right], \quad (1.38)$$

$$P_c^+ = \left[\frac{\rho_c}{F_c^2 + G_c^2} \right]. \quad (1.39)$$

The penetrability for γ -ray channels is given by Eq. 1.40

$$P = E_\gamma^{2L+1} \quad (1.40)$$

This is derived from the average power output of an electric or magnetic multipole of multipolarity L (see Ref. [6]). The elements of the channel matrix \mathfrak{B} are the channel penetrabilities ($\mathfrak{B}_c = P_c$). ρ_c is a dimensionless length given by Eq. 1.41 (LT pg.267),

$$\rho_c = \rho_\alpha = k_\alpha r_\alpha, \quad (1.41)$$

where k_α is the wave number given by Eq. 1.42 (LT pg.267)

$$k_c \equiv k_\alpha = \left(\frac{2\mu_\alpha |E_\alpha|}{\hbar^2} \right)^{1/2}. \quad (1.42)$$

Ω is calculated by Eq. 1.43 (LT pg.271 eq.4.5a, EV pg.732 eq.61):

$$\Omega_c^+ \equiv \Omega_{\alpha l}^+ = \exp i(\omega_c - \phi_c^+) \quad (1.43)$$

Note that Ω_c is defined slightly differently in LT and EV (LT pg.271 eq.4.5a, EV pg.732 eq.61). The LT version is the exponential of the EV version, which is exponentiated in the definition of the U-matrix (EV pg.732 eq.62). $-\phi_c^+$ is the hard-sphere scattering phase shift Eq. 1.44 (LT pg.271 eq.4.5b). In EV the hard-sphere scattering phase shift is incorporated into the definition of Ω_c .

$$\phi_c^+ \equiv \phi_{\alpha l}^+ = \tan^{-1}(F_c/G_c) \quad (1.44)$$

ω_c is the Coulomb phase shift given by Eq. 1.45 (LT pg.269 eq.2.13c, EV pg.732 eq.56).

$$\omega_c \equiv \omega_{\alpha l} = \sum_{n=1}^l \tan^{-1}(\eta_{\alpha}/n) \quad (1.45)$$

1.4.5 The T-matrix

Once the U-matrix has been calculated using the W-matrix, it can be used to calculate the transition matrix, or T-matrix (LT pg.292, eq.2.3) using Eq. 1.46:

$$T_{\alpha's'l',\alpha sl}^J = e^{2i\omega_{\alpha's'}} \delta_{\alpha's'l',\alpha sl} - U_{\alpha's'l',\alpha sl} \quad (1.46)$$

The T-matrix can be used to calculate the angle integrated cross-section directly using Eq. 1.47 (LT pg.293, eq.3.2a, eq.3.2b).

$$\sigma_{\alpha,\alpha'} = \frac{\pi}{k_{\alpha}^2(2s+1)} \sum_{Jl'l'ss'} g_J |T_{\alpha's'l',\alpha sl}^J|^2, \quad (1.47)$$

where g_J is the statistical spin factor (LT pg.293, eq.3.2a, eq.3.2c):

$$g_J = \frac{2J+1}{(2I_1+1)(2I_2+1)}. \quad (1.48)$$

where I_1 and I_2 are the spins of particles 1 and 2 and J is the angular momentum of the intermediate state.

The angle-integrated cross-section can then be used to calculate the S-factor with Eq. 1.6. Further calculations are required to get the differential cross-section (LT pg.292 eq.2.1-2.8b). The resultant equation for differential cross-section is given by Eq. 1.49 (LT

pg.292 eq.2.7 corrected by C. Ugalde)

$$\begin{aligned}
(2s+1)\frac{k_\alpha^2}{\pi}d\sigma_{\alpha s,\alpha' s'}d\Omega_{\alpha'} &= (2s+1)|C_{\alpha'}(\theta_{\alpha'})|^2\delta_{\alpha s,\alpha' s'} \\
&+ \frac{1}{\pi}\sum_L B_L(\alpha s,\alpha' s')P_L(\cos\theta_{\alpha'}) \\
&+ \delta_{\alpha' s'\nu',\alpha sl}(4\pi)^{-1/2}\sum_{Jl}(2J+1) \\
&\times 2\text{Re}[iT_{\alpha' s'\nu',\alpha sl}^*C_{\alpha'}(\theta_{\alpha'})P_L(\cos\theta_{\alpha'})], \quad (1.49)
\end{aligned}$$

Note that there is an error in Eq. 1.49 in Lane and Thomas (Ref. [2]). The correction used in the AZURE code was derived by C. Ugalde, though the authors of Ref. [7] offer a different correction (see Appendix A). Here,

$$\begin{aligned}
B_L(\alpha s,\alpha' s') &= \frac{1}{4}(-)^{s-s'}\sum_{J_1 J_2 l_1 l_2 l'_1 l'_2} \bar{Z}(l_1 J_1 l_2 J_2, sL) \\
&\times \bar{Z}(l'_1 J_1 l'_2 J_2, s'L)(T_{\alpha' s'\nu',\alpha sl}^{J_1})(T_{\alpha' s'\nu',\alpha sl}^{J_2})^* \quad (1.50)
\end{aligned}$$

$$\begin{aligned}
\bar{Z}(l_1 J_1 l_2 J_2, sL) &= (2l_1+1)^{1/2}(2l_2+1)^{1/2}(2J_1+1)^{1/2} \\
&\times (2J_2+1)^{1/2}(l_1 l_2 00|L0)W(l_1 J_1 l_2 J_2 sL) \quad (1.51)
\end{aligned}$$

There is a subtlety to Eq. 1.49 in that the Coulomb cross-section part $|C_{\alpha'}(\theta_{\alpha'})|^2$ is added once for every $\alpha s \rightarrow \alpha' s'$ (provided $\alpha=\alpha'$ and $s=s'$), despite the fact that it has no dependence on the channel spin s . This is cancelled by the $(2I_1+1)(2I_2+1)$ factor in Eq. 1.52. To get the total differential cross-section for a given reaction $\alpha \rightarrow \alpha'$ we must then sum over the possible $s \rightarrow s'$ combinations. These are given by LT pg. 292 eq.2.1 and eq.2.2.

$$d\sigma_{\alpha,\alpha'} = \frac{(2s+1)}{(2I_1+1)(2I_2+1)} \times \sum_{ss'} d\sigma_{\alpha s,\alpha' s'} \quad (1.52)$$

1.4.6 The A-matrix

The A-matrix method offers an alternative way of calculating the U-matrix. Whilst the R-matrix is a matrix of channels, the A-matrix is a matrix of levels. Using the A-matrix the inversion of the complex matrix $(\mathbf{1}-\mathbf{RL}^0)$, which is computationally expensive, can be avoided. The A-matrix method can be significantly quicker in situations of many channels and few levels (LT pg.294 eq.1.4, EV pg. 732 eq.50-54).

1.4.7 Alternative parameterization of R-matrix theory

An alternative parameterization of R-matrix theory has been developed by C. R. Brune of Ohio University (Ref. [8]). This was a generalisation, to multiple channels, of the work of C. Angulo and P. Descouvemont (Ref. [9]) and gives a direct link between formal R-matrix reduced width amplitudes and experimentally observed widths Γ . The R-matrix parameters are connected to the experimental width parameters by Eq. 1.53.

$$\Gamma_{\lambda c}^0 = \frac{\Gamma_{\lambda c}(E_{\lambda})}{1 + \sum_c \gamma_{\lambda c}^2 \left(\frac{dS_c}{dE}\right)_{E_{\lambda}}} = \frac{2\gamma_{\lambda c}^2 P_c(E_{\lambda})}{1 + \sum_c \gamma_{\lambda c}^2 \left(\frac{dS_c}{dE}\right)_{E_{\lambda}}}. \quad (1.53)$$

If the resonances are narrow and well spaced, then the simple conversion (Eq. 1.13) can give reasonable estimates of the R-matrix reduced width amplitudes.

1.5 Direct reaction theories

Direct reactions proceed by a fundamentally different mechanism to that of resonance reactions. Instead of forming a compound nucleus and then decaying via one of several exit channels, the incident particle and target proceed directly to the final state.

The cross-section for direct reactions depends on how much the initial state 'looks like' the final state. For instance for the $^{14}\text{N}(p,\gamma)^{15}\text{O}$ reaction, the more the final state of ^{15}O looks like that of a ^{14}N core with a proton, the higher the reaction cross-section. This involves calculating the overlap integral of the initial wavefunction, made up of regular

and irregular Coulomb functions, and the final wavefunction which, outside the nucleus is described by a Whittaker function.

Direct reaction models have been described by several authors (see Refs. [10, 11, 12]). F. C. Barker and T. Kajino (Ref. [13]) report a method of incorporating nonresonant channel contributions into an R-matrix framework. C. Angulo and P. Descouvemont (Ref. [9]) describe a method of incorporating radiative direct capture into an R-matrix framework, also including an alternative parameterization of the R-matrix formalism.

1.5.1 Barker and Kajino nonresonant channel contributions

Barker and Kajino describe R-matrix formulae for radiative capture reactions (Ref. [13], referred to as BK). The cross-section for the general reaction $A + a \rightarrow B^* \rightarrow B + \gamma$ is given by Eq. 1.54 (BK pg.370 eq.3)

$$\sigma_{J_i J_i} = \frac{\pi}{k_a^2} \frac{2J_i + 1}{(2I_a + 1)(2I_A + 1)} \sum_{s_e l_i} |U_{s_e l_i, J_f}^{J_i}|^2, \quad (1.54)$$

where k_a is the wavenumber given by Eq. 1.42, J_i is the initial state, J_f is the final state, I_a and I_A are the spins of the particles a and A , s_e is the channel spin and l_i is the angular momentum between a and A . The U-matrix of Barker and Kajino Eq. 1.55 is divided into resonant and nonresonant parts (BK pg.371 eq.4),

$$\begin{aligned} U_{s_e l_i, J_f}^{J_i} = & -i e^{i(\omega_i - \phi_i)} 2P_{l_i}^{1/2} k_\gamma^{L+1/2} \left[\sum_{\lambda\mu} \gamma_{\lambda s_e l_i}^{J_i} \gamma_{\mu\gamma l_i}^{J_i} A_{\lambda\mu}^{J_i} \right. \\ & + \frac{2\mu_e^{1/2} \bar{e}_L}{\hbar k_a} \left[\frac{(L+1)(2L+1)}{L} \right]^{1/2} \frac{1}{(2L+1)!!} N_f^{1/2} a_e^L F_{l_i}(a_e) G_{l_i}(a_e) \\ & \left. \times \sum_{l_f} i^{l_i+L-l_f} \theta_{f\alpha_e s_e l_f}^{J_f} (I_i L 0 0 | I_f 0) U(L I_f J_i s_e; I_i J_f) J'_L(I_i, I_f) \right], \quad (1.55) \end{aligned}$$

where ω_i is the Coulomb phase shift given by Eq. 1.45, $-\phi_i$ is the hard-sphere scattering phase shift given by Eq. 1.44, P_{l_i} is the entrance channel penetrability, k_γ is the γ -

ray wavenumber, L is the multipolarity of the radiation, $\gamma_{\lambda s_e l_i}^{J_i}$ are the reduced width amplitudes, $A_{\lambda\mu}^{J_i}$ are the A-matrix elements and μ_e is the reduced mass of the projectile and target. F_l and G_l are the regular and irregular coulomb wavefunctions. N_f is a normalisation factor given by:

$$N_f^{-1} = 1 + \sum_{\alpha s l'_f} \frac{2(\theta_{f\alpha s l'_f}^{J_f})}{a_\alpha} \int_{a_\alpha}^{\infty} dr \left[\frac{W_{\alpha s l'_f}(r)}{W_{\alpha s l'_f}(a_\alpha)} \right]^2 \quad (1.56)$$

where $\theta_{f\alpha s l'_f}^{J_f}$ is the dimensionless reduced width of the final state given by Eq. 1.57 (BK pg.372 eq.15),

$$\theta_{\lambda c}^J = \gamma_{\lambda c}^J (\hbar/\mu_c a_c^2)^{-1/2}, \quad (1.57)$$

where a_c is the channel radius. \bar{e}_L is the effective charge given by Eq. 1.58 (BK pg.372 eq.17)

$$\bar{e}_L = \mu_e^L \left[\frac{Z_a}{M_a^L} + (-)^L \frac{Z_A}{M_A^L} \right] e, \quad (1.58)$$

J'_L is given by Eq. 1.59 (BK pg.372 eq.12),

$$J'_L(I, I'_f) = \frac{1}{a_c^{L+1}} \int_{a_c}^{\infty} dr r^L \frac{W_{\alpha s l'_f}(r)}{W_{\alpha s l'_f}(a_c)} \left[\frac{F_l(r)}{F_l(a_c)} - \frac{G_l(r)}{G_l(a_c)} \right]. \quad (1.59)$$

1.5.2 Angulo and Descouvemont direct capture

C. Angulo and P. Descouvemont have developed an alternative parameterization of the R-matrix theory (see Refs. [9], referred to as AD) which includes a version of direct capture. The angle integrated cross-section is given by Eq. 1.60 (AD pg.757 eq.6),

$$\sigma(E, J_i \pi_i \rightarrow J_f \pi_f) = \frac{\pi}{k^2} \frac{2J_i + 1}{(2I_1 + 1)(2I_2 + 1)} |M_{int} + M_{ext}|^2, \quad (1.60)$$

and is similar to the equation for the angle integrated cross-section presented in Ref. [2] (Eq. 1.47), except that the U-matrix has been replaced by internal (standard R-matrix) and external (direct capture) components, in much the same way as the Barker and Kajino version (Eq. 1.55).

Note that Eq. 1.60 is limited to a single $J_i\pi_i \rightarrow J_f\pi_f$ (i.e. a single s value). The contributions from different s values can be calculated separately and summed. The internal parts are the modified R-matrix equation, given by Eq. 1.61 (AD pg.757 eq.7)

$$M_{int} = \frac{\sum_{\lambda} \varepsilon_{\lambda} \left[\widetilde{\Gamma}_{\lambda}(E) \widetilde{\Gamma}_{\lambda}(E) \right]^{1/2} / (E_{\lambda} - E)}{|1 - LR(E)|}. \quad (1.61)$$

This is essentially the single channel R-matrix formula, though expressed using experimental widths Γ through the alternative parameterization. The external parts are given by Eq. 1.62 (AD pg.758 eq.8), as

$$M_{ext} = C \left[Z_1 \left(\frac{A_2}{A} \right)^L + Z_2 \left(\frac{-A_1}{A} \right)^L \right] K_{if} \times \int_a^{\infty} [F_{l_i}(kr) \cos \delta + G_{l_i}(kr) \sin \delta] W_{-\eta, l_f + \frac{1}{2}}(2k_f r) r^L dr. \quad (1.62)$$

where Z_1 and Z_2 are the proton numbers of the projectile and target, A_1 and A_2 are the mass numbers, A is the sum of the mass numbers of particles 1 and 2 and W is a Whittaker function. δ is the phase shift, which can be calculated from the U-matrix of Eq. 1.63 (AD pg.757 eq.2, LT pg.273 eq.1.15).

$$U = \frac{1}{1 - RL^0} = \exp(2i\delta) \quad (1.63)$$

The external matrix element contributions are linked to the internal matrix elements as δ is calculated from the internal matrix elements. K_{if} is a geometric factor given by

Eq. 1.64 (AD pg.758 eq.9).

$$\begin{aligned}
 K_{if} &= e \left[\frac{8(L+1)(2L+1)}{L\hbar\nu} k_\gamma^{2L+1} (2l_i+1)(2l_f+1)(2J_f+1) \right]^{1/2} \\
 &\times \frac{1}{(2L+1)!!} \begin{pmatrix} l_f & L & l_i \\ 0 & 0 & 0 \end{pmatrix} \begin{bmatrix} J_i & l_i & I \\ l_f & J_f & L \end{bmatrix}
 \end{aligned} \tag{1.64}$$

In this model one can calculate the U-matrix contributions for the direct capture component and simply add them to the internal matrix components to get the U-matrix. The situation may be more complicated if angular distributions were to be considered.

Chapter 2

The AZURE R-matrix code

R. E. Azuma, E. C. Simpson, C. Ugalde, J. Görres, M. Heil and M. Wiescher have developed a new multi-channel R-matrix computer code called AZURE. It can simultaneously fit as many channels as desired, for all elastic scattering, particle and radiative capture reactions. It is designed to be easily adaptable to a variety of reactions. For each reaction, all allowed spin and angular momentum channels can be calculated.

2.1 Program structure

The AZURE code is written in the FORTRAN 77 programming language. A schematic of the structure of the code is shown in Fig. 2.1. The main file `azure.for`, the subroutine files `minuit200.f` and `azutils_mh.for` and the memory management file `memory.h` are required at compilation. On executing the program the configuration files are read and certain parameters (penetrabilities, coulomb cross-sections etc.) are calculated. The `param.par` file, which contains all the parameters (reduced width amplitudes and level energies) to be fitted by the MINUIT subroutine, is created. The MINUIT subroutine is given the parameters to be fitted, varies them and evaluates the fit against experimental data using the subroutine FCN.

The calculation of cross-sections from R-matrix theory can be computationally ex-

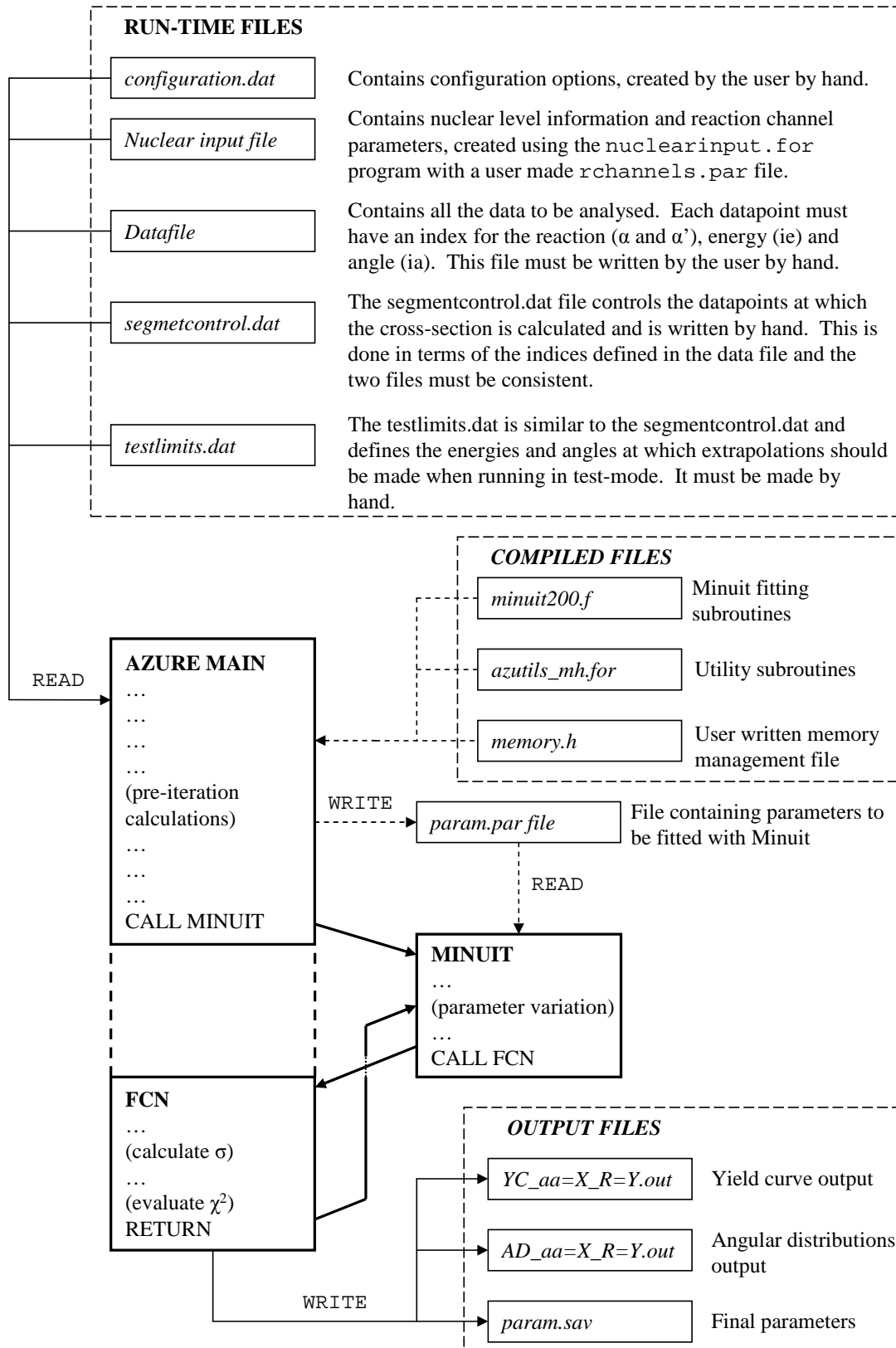


Figure 2.1: An overview of the structure of the AZURE code.

ensive. A fitting procedure must be used to find the reduced width amplitudes which give the best fit to experimental data, so the cross-section calculation must be repeated thousands of times. The code consists of a preliminary section and an iteration section, with the latter containing the cross-section calculations. Removing calculations from the iteration loop to the preliminary section can save CPU time.

Consequently, the iteration section FCN has been stripped down so that only the bare minimum number of calculations are made. This does place some limitations on the code. For example, one cannot have the radius a as a fitted parameter or vary the degree of target integration required. However the increase in efficiency is huge, allowing the code to be used on ordinary desktop computers.

The AZURE code can be used to fit experimental data or make calculations at user defined particle energies and angles. Often the user will want to fit to experimental data and then make an extrapolation based on the fitted parameters. The fitting routine used in the AZURE is MINUIT (see Ref. [14]). It alters the parameters (i.e. the reduced width amplitudes, level energies and normalisation parameters) and calls FCN which calculates the cross-section and compares it to the experimental data using a χ^2 method. The process is then repeated until the lowest χ^2 is found.

2.1.1 Subroutine files

There are two files containing subroutines required by AZURE. `minuit200.f` contains all the subroutines required by the MINUT minimisation package (see Ref. [14]) and `azutils_mh.for` contains a number of subroutines used by AZURE. These subroutines include COULL which is used in calculating regular and irregular coulomb wavefunctions, CALPHA which is used to calculate the coulomb cross-section and MATINV, a matrix inversion algorithm.

2.1.2 Configuration and input files

`memory.h`

The `memory.h` file specifies the limits for the largest arrays used within AZURE. As many parameters (penetrabilities, Coulomb cross-sections etc.) are calculated outside of the fitting iterations, a `COMMON BLOCK` is required to share these parameters between the main program and subroutines. The disadvantage of this is that it requires a large amount of memory. The `memory.h` is a convenient way of managing the size of arrays and thus the memory requirements

It is important to understand the parameters specified in the `memory.h` as if they are too small AZURE will compile, but may produce unexpected and inexplicable results. If they are excessively large, compilation may fail, or the program will fail to run once compiled. The `memory.h` is incorporated into AZURE using an `INCLUDE` statement, meaning that it is read as part of the code at compile time. AZURE must be recompiled for changes to the `memory.h` to have an effect.

`configuration.dat`

The `configuration.dat` file contains many setup parameters and flags which control the operation of AZURE. Examples of options set in this file are the value of the nuclear radius a , whether to use R-matrix or A-matrix methods and whether fit to experimental data or make extrapolations. `configuration.dat` is read at run-time, so there is no need to recompile if changes are made.

Nuclear input file

The nuclear input file contains all the nuclear parameters of the compound nucleus, including level energies E_λ and J^π , and all the possible reaction channels. It is created using a separate program called `nuclearinput.for` (see Appendix B and Section 2.3.1). The file `nucfile.dat` is a pointer file, which contains the name of the nuclear input file.

Data file

The data file contains the experimental data to be fitted and must be correctly indexed for use with AZURE. Each data point must be assigned the correct `aa` for initial particle pair and `ir` for the final particle pair. Each energy is then assigned an energy index `ie`, and each angle assigned and angle index `ia`.

Different data points can share `ie` and `ia` indices, even if their `ir` are different. The advantage of this will be to reduce the memory requirements of AZURE (providing the `memory.h` is set accordingly). However depending on the complexity of the data set, the `segmentcontrol.dat` file can become prohibitively complex, so where the memory requirements allow, it is easier to give data points of the same energy, but different `ir`, different `ie`. The file `datafile.dat` is a pointer file, containing the name of the data file.

`segmentcontrol.dat` and `testlimts.dat`

The AZURE code calculates the cross-section ‘by segments’. Each segment is a range of energies and angles at which the cross-section should be calculated. The segments in the `segmentcontrol.dat` are described using the indices `aa`, `ir`, `ie` and `ia`. If fits to data are to be made, these indices correspond to the actual channels, energies and angles described in the data file. If one wishes to make extrapolations, the `testlimts.dat` file is used to create an internal dataset for the specified energies and angles. These files also contain further parameters which control the target integration and convolution of the data.

Note that these two files are to be modified to make them entirely independent of each other (see section 2.3.3). The new versions will be called `segmentsdata.dat` and `segmentstest.dat` and will make it easier to switch between fitting and extrapolation modes.

c		c'	$\alpha'=1$			$\alpha'=2$	$\alpha'=3$
			A	B	C	D	E
$\alpha=1$	$^{14}\text{N}+\text{p}, s=1/2, l=2$	A	↑↑↑↑	↑↑↑↑	↑↑↑↑	↑↑↑↑	↑↑↑↑
	$^{14}\text{N}+\text{p}, s=3/2, l=0$	B	↑↑↑↑	↑↑↑↑	↑↑↑↑	↑↑↑↑	↑↑↑↑
	$^{14}\text{N}+\text{p}, s=3/2, l=2$	C	↑↑↑↑	↑↑↑↑	↑↑↑↑	↑↑↑↑	↑↑↑↑
$\alpha=2$	$^{15}\text{O}_{\text{g.s.}}+\gamma, L=1, E1$	D	⊗	⊗	⊗	⊗	⊗
$\alpha=3$	$^{15}\text{O}_{6.79}+\gamma, L=1, M1$	E	⊗	⊗	⊗	⊗	⊗
	$^{15}\text{O}_{6.79}+\gamma, L=3, E2$	F	⊗	⊗	⊗	⊗	⊗

Figure 2.2: An illustration of the reaction pathways system used in AZURE, for the $^{14}\text{N}(\text{p},\gamma)^{15}\text{O}$ reactions, populating a $J^\pi=3/2^+$ resonance. Each reaction pathway is indicated by an arrow. Here we consider only the $\alpha=1$ entrance channels, but in principle every channel can be treated as an entrance and exit channel. The indexes in AZURE for α is aa and α' is ir.

2.2 Code concepts

2.2.1 Reaction pathways

To improve efficiency, AZURE sorts all the possible channels into reaction pathways, which give all the possible combinations of entrance and exit channels. In terms of the T-matrix, one can envisage a pathway as entering a particular row, and exiting through particular column. Examining Eq. 1.49, only pathways with the same $\alpha s \rightarrow \alpha' s'$ need to be added coherently, so the reaction pathways are grouped according to their $\alpha s \rightarrow \alpha' s'$. Each reaction pathway populates a specific J^π group of levels, but different J^π level groups can interfere with each other.

The coherently added $\alpha s \rightarrow \alpha' s'$ groups are indexed by \mathbf{k} , and the subindex \mathbf{m} indexes each of the coherently added pathways within the \mathbf{k} group. As different J^π levels can interfere, the \mathbf{k} index runs continuously for all pathways regardless of the populated J^π group. The reaction pathways are illustrated in Fig. 2.2.

2.2.2 Background poles

The R-matrix theory necessarily involves some truncation of the number of energy levels due to the infinite number of energy eigenfunctions. It would be computationally impossible to include every level within a given compound nucleus, so background resonances above the energy range of interest must be included to simulate the tails of higher energy resonances.

2.3 Development of the code

The main developments of the code made during the course of this project are summarised below. In addition to these modifications, many smaller changes were made. A great many checks of the code were made and numerous bugs were discovered and corrected.

2.3.1 Longform input code

The input code of AZURE was rewritten to allow the inclusion of all calculated spin and angular momentum channels in the nuclear input file. Previously only one reduced width amplitude γ could be specified for each energy level for each $\alpha \rightarrow \alpha'$. If the user wanted to alter the reduced width amplitudes for the different s and l channels, the `param.par` file had to be edited by hand. The nuclear input file must now be created using a special program, which calculates the appropriate spin and angular momentum combinations in exactly the same way as AZURE, according to the limits set in the `configuration.dat` file.

The new system allows specification of the reduced width amplitude for each $c \rightarrow c'$ in the nuclear input file. This was not a trivial change. The old system, which initially referred to the information in the nuclear input file by the line number, was embedded into much of the pre-iteration section. These changes have made the nuclear input file read-in easier to understand, simplified the creation of the nuclear input file and made AZURE easier to use.

To create the new form of input file the user must first create a reaction channels file, `rchannels.par`. This file specifies all the information required for the initial and final states, α and α' (`aa` and `ir`).

The user then runs `nuclearinput.exe` (see Appendix B). The program reads the parameters from the `rchannels.par` into arrays and asks the user to enter the appropriate J , π and excitation levels to define the compound nucleus. The program then calculates the allowed s and l combinations based on the limits in `configuration.dat`, and combines this information with the `rchannels.par` information to create the AZURE nuclear input file. The program requires that the `memory.h` is consistent with the `rchannels.par`, as values in the `memory.h` are used to define several array bounds. If the `memory.h` is incorrect, the program will give strange errors.

The calculation of the spin and angular momentum calculations works exactly the same in AZURE. For example, the $^{14}\text{N}(p,\gamma)^{15}\text{O}$ reactions. The ^{14}N nucleus has spin $s_h=1^+$ and the proton has spin $s_l=\frac{1}{2}^+$. We wish to populate a state of $J^\pi=\frac{3}{2}^+$ in the ^{15}O compound nucleus. When choosing the angular momentum between the ^{14}N and proton, we must ensure that we conserve parity. In this case, the parity does not change; we go from initial positive parity to positive final parity. This means that the angular momentum between the ^{14}N and proton must be even.

If we couple the ^{14}N and proton spins as $1^+ - \frac{1}{2}^+$, we can populate the state with an angular momentum coupling between the ^{14}N nucleus and the proton of $l = 2$ only. If we couple the ^{14}N and proton spins to $1^+ + \frac{1}{2}^+$, we can form the compound state by having angular momentum $l = 0$ or $l = 2$. This gives us three channels which can populate a $\frac{3}{2}^+$ state in the ^{15}O nucleus.

The `configuration.dat` file contains two flags to limit the possible number of channels for a given α . These limits are `lmax`, the maximum l value for a given spin, and `nlmax` the maximum number of l channels for a given a spin.

We then consider the γ -decay from the $\frac{3}{2}^+$ excited state to the $\frac{1}{2}^-$ ground state. There is a parity change, so the multipolarity L of the gamma-ray must be odd for electric

radiation and even for magnetic radiation. The value of L must be between $|I_f - I_i|$ and $|I_f + I_i|$. We allow one L value, if the lowest possible L value gives electric radiation (i.e. E1) and two if the lowest L value is magnetic (i.e. M1 and E2).

This discussion is related to a ‘longform’ type input file. Previously, the input file had not specified the spin and angular momentum for each channel, but were calculated in AZURE. A flag has been added to AZURE to allow input in either new ‘longform’ or old ‘shortform’. The flag is `inputstyle` and is found in `configuration.dat`. The main purpose of this is to allow backwards compatibility with older files to enable checking of the new system. Future users are expected to use the ‘longform’ version input.

2.3.2 Output code

The output code has been changed to make it more scalable, so that the user should have to make few modifications to get the output as desired. The output files are named logically, so that for $aa = x$, $ir = y$ the output file will be named `YC_aa=x_R=y.out` for yield curves (energy vs. cross-section, constant angle) and `AD_aa=x_R=y.out` for angular distributions (angle vs. cross-section, constant energy).

2.3.3 Changes to `segmentcontrol.dat` and `testlimits.dat`

The `segmentcontrol.dat` and `testlimits.dat` files, which control at what energies and angles the cross-section is calculated, were altered to make them entirely independent. Previously the user had to modify the `segmentcontrol.dat` to make it consistent with the `testlimits.dat` when switching between fitting and extrapolation modes. The modifications made make the change between modes as simple as changing the flag in the `configuration.dat`.

Flags have been added so that the user can simultaneously fit a number of different data types. Previously this would have involved messy modifications to the code, which would be prohibitive to the average user. In an effort to allow as many data formats as pos-

AZURE variable	AZURE value	Property	Intype summation value	Outtype summation value
Etype	1	LAB	0	0
	0	CM	8	2
Sigmatype	1	σ	0	0
	0	S-factor	4	1
Difftype	1	Angle-Integrated	0	-
	0	Differential	2	-
SigEtype	1	LAB	0	-
	0	CM	1	-

Table 2.1: Intype and Outtype property summing table

sible, the `intype` and `outtype` flags were added to the new forms of `segmentcontrol.dat` and `testlimits.dat`, `segmentsdata.dat` and `segmentstest.dat`.

The value for `intype` written in the segment control files should be the sum of the numbers for the required data type (see Table 2.1). This system identifies all the possible combinations with one simple number. This associated properties are deduced by AZURE. `Etype` specifies the coordinate system of the particle energies, `Sigmatype` specifies whether the data is cross-section or S-factor format, `Difftype` specifies whether the data is angle-integrated or differential with respect to angle and `SigEtype` specifies the coordinate system of the data and given angles. These properties are used in the data read in, where the S-factor conversion factors are calculated and in the χ^2 calculation.

The output data takes the differential option from the `intype` data and the cross-section is always in the centre of mass system (there exists no `dsig` or `sig_ang_int` for the lab system at present). Note that there is still some work to be done on these modifications. These changes to the segment control naturally lead to an ‘autoextrapolation’ mode, where AZURE fits to data and then calculates the extrapolation automatically, though this facility is still to be implemented.

Chapter 3

Nonresonant contribution development code

A FORTRAN code has been written to calculate the nonresonant channel contribution to the U-matrix elements as described by Barker and Kajino (Ref. [13], see Appendix C). The initial emphasis of this code has been to accurately calculate the energy dependent parts of the cross-section. The absolute scaling of the cross-section has not yet been fully taken into account. This development code will be integrated into the AZURE R-matrix code, though this has not yet been completed. It has already been partially integrated so that simple comparisons can be made with other calculations.

3.1 Energy dependence of nonresonant channel contributions

This investigation aimed to understand the difference in energy dependence between nonresonant channel contributions as described in Ref. [13] and the tails of high energy R-matrix resonances. If one excludes the penetrability factors, an R-matrix calculation based on a high energy pole should be virtually energy independent at the tails, though there may be some slight energy dependence in \mathbf{L}^0 and $\mathbf{\Omega}$. The penetrability factors are

identical for R-matrix and nonresonant channel contributions. If the energy dependence of nonresonant channel contributions is to be the same as a background pole, the U-matrix of Ref. [13] should be energy independent if the penetrability factors are excluded.

The energy dependence is determined by the J'_L term Eq. 3.1, which involves an integral of Coulomb wavefunctions and Whittaker functions over the radius r . The Coulomb wavefunctions are particle energy-dependent, but binding energy independent. The Whittaker function is particle energy independent, but dependent on the binding energy. Here, the binding energy is the energy that the final state is below the threshold energy

$$J'_L(I, I'_f) = \frac{1}{a_c^{L+1}} \int_{a_c}^{\infty} dr r^L \frac{W_{\alpha sl'_f}(r)}{W_{\alpha sl'_f}(a_c)} \left[\frac{F_l(r)}{F_l(a_c)} - \frac{G_l(r)}{G_l(a_c)} \right]. \quad (3.1)$$

When we look at this integral for a range of particle energies, at different binding energies, we see that the energy dependence changes with binding energy, despite the particle energy dependent Coulomb wavefunctions being binding energy independent.

3.1.1 Whittaker functions for various binding energies

The Whittaker functions take the form of a decaying exponential, whose rate of radial decay is related to the binding energy. The further the final state is below the threshold energy, the faster in terms of radius the Whittaker function decays. This makes qualitative sense; ^{15}O in a loosely bound state might look like a ^{14}N core and a proton, giving it a wavefunction which extends further outside the nucleus (see Fig. 3.1). We arbitrarily define the attenuation radius $r_{\text{Whittaker}}$, as the radius at which the Whittaker function is 0.00001 of its initial value. Table 3.1 gives examples of this radius for various binding energies.

3.1.2 Energy dependence

Now we examine the radial dependence of the Coulomb wavefunctions for various incoming particle energies (shown in Fig. 3.2). Note that the Coulomb wavefunctions do

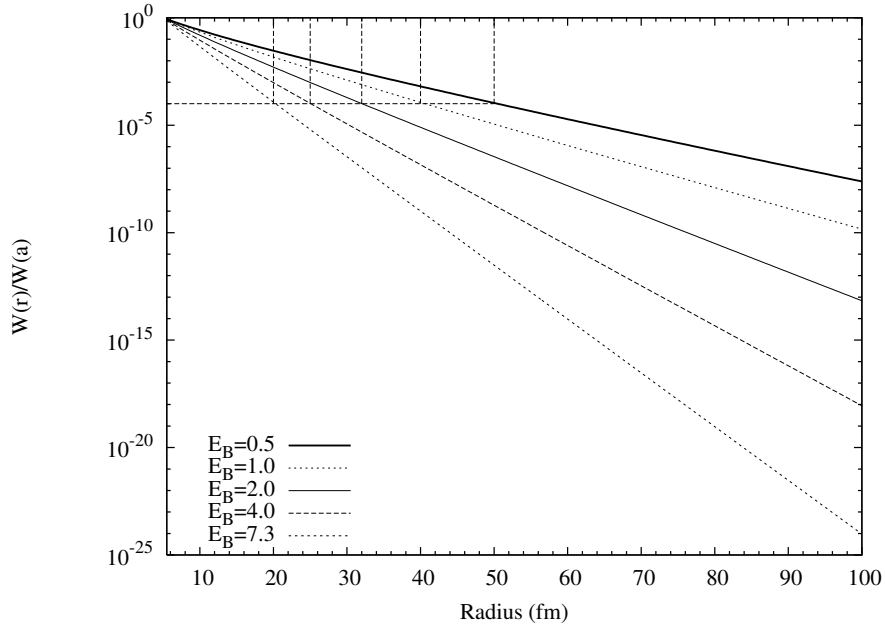


Figure 3.1: Whittaker functions for different binding energies, showing the approximate radius at which the Whittaker function has fallen to 0.0001 it's initial value. Calculated using the WHITT subroutine (found in `azutils_mh.for`) written by M. Heil.

Binding Energy (MeV)	Approximate Attenuation Radius (fm)
0.5	48
1.0	40
2.0	32
4.0	25
7.3	20

Table 3.1: Approximate attenuation radii for Whittaker functions for final states of different binding energies.

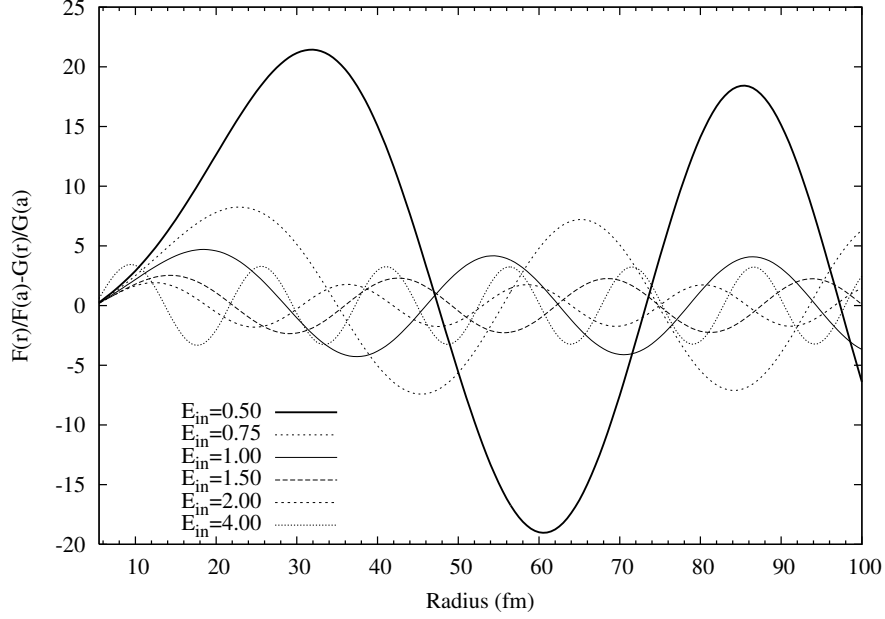


Figure 3.2: The incoming and outgoing coulomb wavefunction part of J'_L (see Eq. 1.59).

not decay. An integral over the Coulomb wavefunctions from a_c to ∞ would yield zero (or close to zero). Also, as the particle energy increases, the radial period of oscillation, $r_{coulomb}$, decreases and that over the energy range of interest the radial period of oscillation is similar to the attenuation radius. Some examples of the integral J'_L are shown in Figs. 3.3 and 3.4.

The observed energy dependence is the result of the product of the Coulomb wavefunctions and the Whittaker functions. Higher energy Coulomb wavefunctions oscillate over a shorter radius and larger binding energy Whittaker functions decay in shorter radius. The Coulomb wavefunction contribution oscillates between positive and negative, but at the lowest energies the Coulomb wavefunctions are attenuated entirely within the positive part of the oscillation. As the particle energy increases, the oscillation radius $r_{Coulomb}$ decreases rapidly, meaning more of the negative part of the Coulomb wavefunction oscillation is included in the J'_L integral (see Fig. 3.2).

Once $r_{Coulomb} \ll r_{Whittaker}$ the particle energy dependence is weak as $r_{Coulomb}$ varies more slowly as particle energy increases, so that J'_L has a weaker energy dependence. As higher binding energies have faster attenuation, they tend to be less sensitive to changes in

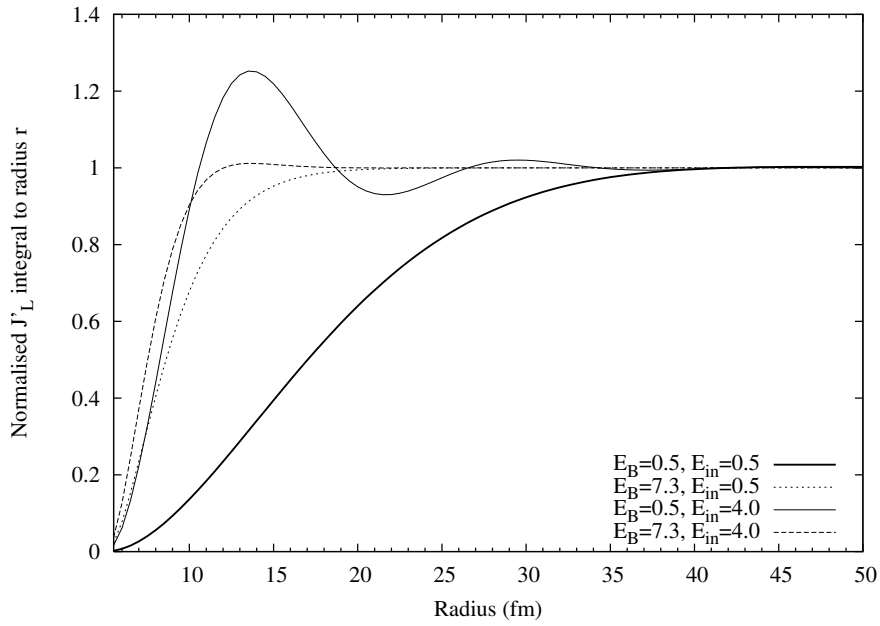


Figure 3.3: The integral J'_L , normalised to its asymptotic value. The values with the higher binding energy reach their asymptotic values at a smaller radius, and oscillations can be seen for the higher incident particle energies.

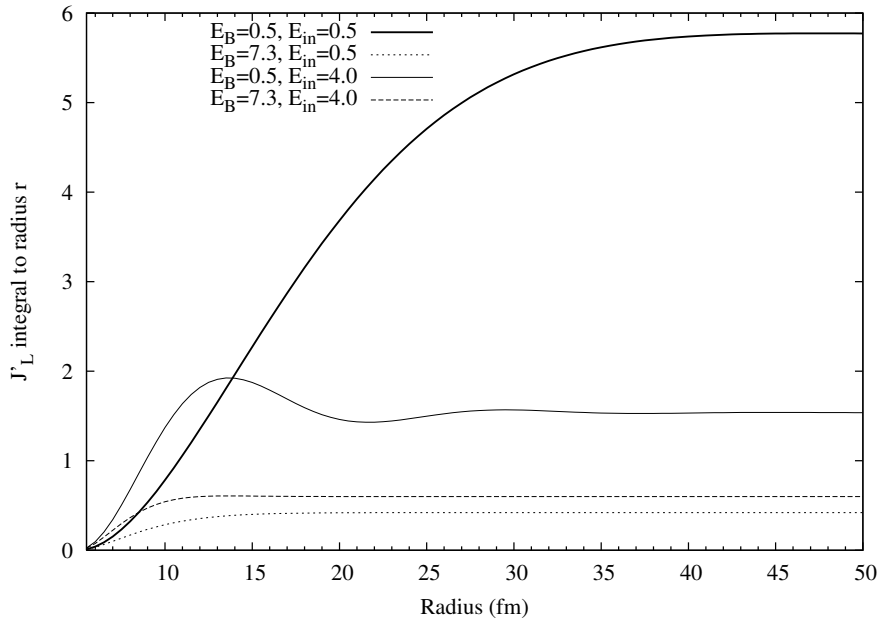


Figure 3.4: The integral J'_L . Notice that the ratio of the asymptotic values for different incident particle energies is close to one for higher binding energies, but for lower binding energies, the integral is much larger at low incident particle energy than at high incident particle energy. This indicates that low binding energies may have a stronger particle energy dependence for the U-matrix elements.

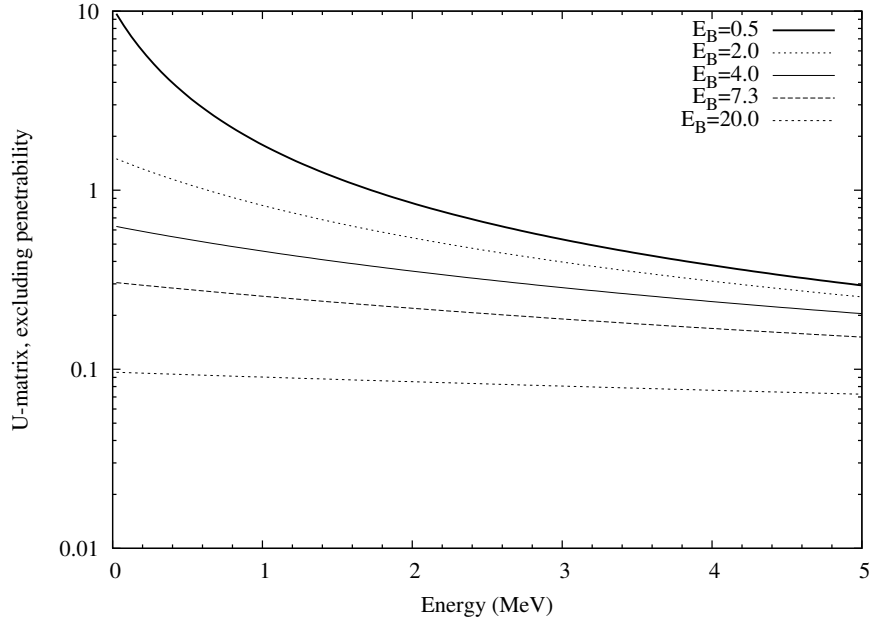


Figure 3.5: The incident particle energy dependence is dependent on the binding energy of the final state. For higher binding energies, the penetrability-less U-matrix is essentially energy independent, but climbs steeply at lower particle energies for lower binding energies.

$r_{Coulomb}$, so that lower binding energies give J'_L a stronger energy dependence. Examples of the energy dependence of U-matrix (excluding the penetrability) for different binding energies are shown in Fig. 3.5.

The Astrophysica code (see Ref. [15]) is a general purpose R-matrix and direct capture code. It has been used to make comparisons with the development code, shown in Fig. 3.6.

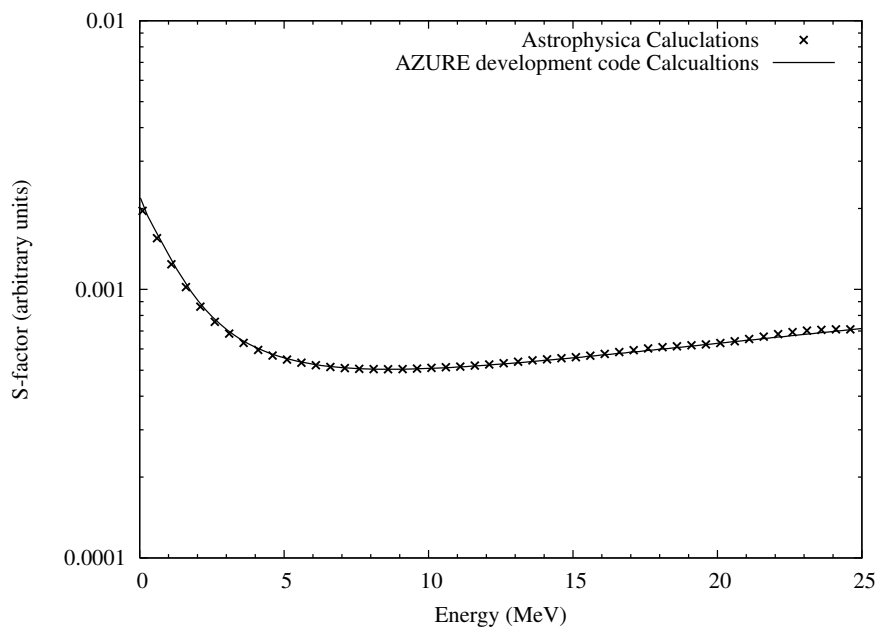


Figure 3.6: Comparison of calculations made with the `BarkerKajino.for` development code (see Appendix C and Astrophysica Ref. [15]). The agreement is good over a wide range of energies.

Chapter 4

$^{14}\text{N}(\text{p},\gamma)^{15}\text{O}$ reactions

The $^{14}\text{N}(\text{p},\gamma)^{15}\text{O}$ reaction determines the overall rate of the CNO cycle and has recently been measured and analysed using an R-matrix method (see Refs. [9, 16, 17, 18]). It is an excellent test of the radiative capture parts of the AZURE code and the recent analysis allows useful comparisons.

This analysis also sought to investigate the additional constraint on the radiative capture channels offered by $^{14}\text{N}(\text{p},\text{p})^{14}\text{N}$ elastic scattering measurements, suggested by Ref. [19]. It has been an excellent test of the elastic scattering code and has identified errors which other elastic scattering analyses had failed to find.

4.1 Summary of experimental measurements

4.1.1 ^{15}O compound nucleus

When a proton interacts with a ^{14}N nucleus, a ^{15}O compound nucleus is formed. The Q-value for the reaction, which is related to the mass of the particles, is +7.297 MeV. The relevant excited states of the ^{15}O compound nucleus, which correspond to resonances in the $^{14}\text{N}(\text{p},\gamma)^{15}\text{O}$ cross-sections, are shown in Fig. 4.1. Once formed the compound nucleus deexcites by emitting a γ -ray, the energy of which is determined by the energy of the compound state and the energy of the final state. The main transitions are those

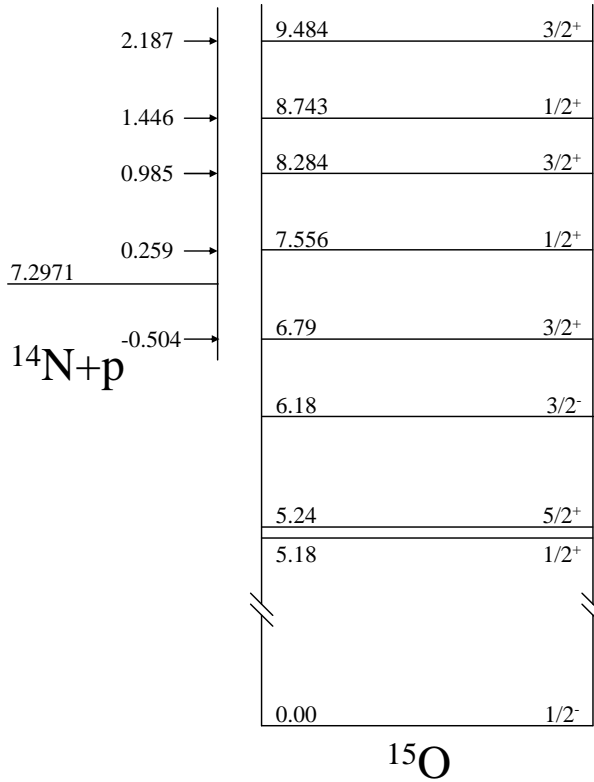


Figure 4.1: The ^{15}O level scheme for the energy range of interest. States present in the γ -ray transitions studied are shown.

to the ground, 6.18 and 6.79 MeV states, though transitions to the 5.18, 5.24, 6.86, 7.28 and 7.56 MeV states have also been observed, but are thought to contribute negligibly to the low energy cross-section (see Ref. [20]).

The 0.259 MeV $1/2^+$ state appears in all γ -ray transitions. The 0.985 MeV $3/2^+$ state appears in the ground state and 6.18 MeV transitions. The 2.187 MeV $3/2^+$ state is broad, and appears in the ground state transition. The 1.446 MeV $1/2^+$ state appears in the 6.18 transition only.

4.1.2 Experimental measurements

The authors of Ref. [20] studied the $^{14}\text{N}(\text{p},\gamma)^{15}\text{O}$ reaction over a wide range of energies. The ground, 5.18, 5.24, 6.18, 6.79, 6.86, 7.28 and 7.56 MeV transitions were measured using gas and solid targets.

However, it was later discovered that the data presented in Ref. [20] did not take

summing corrections into account (Ref. [21]). Summing effects are the result of two sequential γ -rays reaching a detector simultaneously. The energy detected is the sum of the individual γ -ray energies. For instance, γ -ray emission to an excited state is quickly followed by another γ -ray emission to leave the compound nucleus in the ground state. If both γ -rays were detected simultaneously, it would appear that there had been a capture to the ground state rather than the excited state. Corrections to the data of Ref. [20] were made by H. -P. Trautvetter.

Measurements have more recently been made at the Laboratori Nazionali del Gran Sasso, Italy, using the 400keV LUNA (Laboratory for Underground Nuclear Astrophysics) accelerator facility (Refs. [16, 22, 18]). The laboratory is situated under a mountain with 1400m of rock cover, which reduces the background by three orders of magnitude at energies $E_\gamma < 5$ MeV when compared to a detector on the surface (Ref. [18]). The reduction of background is critical when measuring very small cross-sections. A germanium detector placed at 55° to the beam direction was used to derive the angle integrated cross-section.

Summing effects were taken into account by considering the detection efficiencies at the ground state, primary and secondary transition energies, and the branching ratios of the transitions.

Measurements at the Laboratory for Experimental Nuclear Astrophysics (LENA), Tri-Universities Nuclear Lab, North Carolina were made using a 1 MV Van de Graff accelerator with a HPGe detector at 0° (Ref. [17]). The target and detector were surrounded in an annulus of NaI(Tl), which vetoed cosmic ray background by detecting coincidences in the Ge and NaI detectors, and suppressed cascades. The geometry of the experiment was fixed, so angular distributions could not be measured, but the transitions to the ground, 5.18 and 6.18 MeV states were believed to be nearly isotropic in the energy range of interest. The 6.79 MeV transition was expected to have angular distributions, so the isotropic secondary γ -ray was used to determine the cross-section.

A new measurement has been made for the transition to the 6.79 MeV state at energies above the the 0.259 $1/2^+$ resonance (Ref. [23]). Due to the large non-resonant

Dataset	E_{CM} Range (MeV)		
	0.00 MeV	6.18 MeV	6.79 MeV
Schröder 1987 [20]	0.32-3.35	0.18-3.35	0.38-1.53
LUNA 2004 [16]	0.127-0.393	0.127-0.393	0.127-0.393
LENA 2005[17]	0.187-0.485	0.134-0.485	0.164-0.436
Klug 2005 [23]	-	-	0.548-1.307

Table 4.1: Data ranges for recent measurements.

contribution in this transition which determines the low energy cross-section, this study was made to check the data of Ref. [20]. Table 4.1 shows the energy ranges for the three most important transitions for each of the data sets.

The elastic scattering channel has been studied by a number of authors (see Refs. [24, 25, 26, 27]). For the analysis of the elastic channel presented here it was decided to use the data from Ref. [25] as it contains angular distributions at eleven angles for 105 energies in the range 1-2.5 MeV, for a total of 1155 data points.

4.1.3 Previous analysis

The authors of Ref. [20] fit their data using a combination of resonant contributions calculated using a one-level Breit-Wigner formula and direct capture contributions, calculated using a method similar to that described in Ref. [12]. The results suggest that the most significant contributions to the low energy S-factor come from the ground state and 6.79 MeV transitions and that both contribute a similar amount to the S-factor.

The R-matrix fits of Ref. [9] were made using the data of Ref. [20]. It was assumed that for each J^π a single channel spin and single l value would contribute. This assumption is expected to be valid at low energies where only the lowest l values will contribute. In the ground-state fits they included the $1/2^+$ at 0.259 MeV and $3/2^+$ resonances at -0.504, 0.985 and 2.187 MeV. They also included $1/2^+$ and $3/2^+$ ($l_i=0$) background resonances at 5.0 MeV and an external direct capture contribution. All proton and Γ -widths were left as free parameters. The fitted $S(0)$ for the ground state transition was a factor of 19 smaller than the value suggested by Ref. [20].

For the 6.18 MeV transition the authors of Ref. [9] included resonance contributions from the $1/2^+$ resonances at 0.259 and 1.446 MeV and $3/2^+$ resonances at -0.504, 0.985 and 2.187 MeV. They also included background poles for each J^π component. The free parameters were the Γ_p and Γ_γ widths. The transition to the 6.79 MeV state included the $1/2^+$ resonance at 0.259 MeV and a direct capture contribution. All fits were made using a radius parameter $a=6.5$ fm, though it was noted that the sensitivity of the results to the choice of radius parameter was rather low. The results for the 6.18 and 6.79 MeV transitions were in reasonable agreement with those of Ref. [20].

The R-matrix fits of Ref. [16] used the corrected data of Ref. [20] and the new data published in that paper to fit the transitions to the 6.79 MeV and ground states. The 6.79 MeV transition was fitted with the 0.259 $1/2^+$ MeV resonance and an external direct capture contribution.

A fit of the ground state transition data from Ref. [16] and Ref. [20] was then made using the $3/2^+$ subthreshold state, the 0.259 MeV $1/2^+$, 0.987 MeV $3/2^+$ and 2.187 MeV $3/2^+$ resonances and a background pole at 6 MeV. The fit parameters were the Γ_γ of the subthreshold state, the 0.987 and 2.187 MeV resonances and the Γ_p and Γ_γ of the background pole. The γ^2 of the subthreshold state was fixed using the fits to the transition to the 6.79 MeV state. An external direct capture contribution was also included.

The authors of Ref. [17] performed an R-matrix analysis of the data published in the paper, using the method described in Ref. [9]. They did not include the higher energy data from Ref. [20] in their fits. The fits for the 6.79 MeV transition included the 0.259 MeV $1/2^+$ resonance and a direct capture contribution. The Γ_γ of the resonance was fixed $\Gamma_\gamma=9.2\pm 0.1$ meV, deduced from the observed resonance strength and the relevant branching ratio. The ANC of the direct capture component and Γ_p of the 0.259 MeV resonance were left as free parameters.

For the ground state transition the 0.259 MeV $1/2^+$ resonance and $3/2^+$ resonances at -0.504, 0.985 and 2.187 MeV are included. Also included is a $3/2^+$ ($l = 1$) background pole at 4 MeV. The parameters for the 0.985 and 2.187 MeV resonances were fixed using

values from Ref.[9], the proton width for the background pole was fixed $\Gamma_p=4$ MeV and the Γ_γ width of the 0.259 MeV resonance was fixed using the observed resonance strength. The ANC of the direct capture was also fixed. The free parameters were the Γ_p of the 0.259 MeV resonance and the Γ_γ of the subthreshold state and background pole.

For the fits of the transition to the 6.18 MeV state include contributions from a $1/2^+$ resonance at 0.259 MeV, the subthreshold state and a background pole. Fits were made for different values of the Γ_γ parameters of the subthreshold state and background resonance and an intermediate value of the $S(0)$ adopted.

An R-matrix analysis of the transitions to the 5.18 and 6.18 MeV states was published in Ref. [18]. This analysis included data from both the LUNA and the LENA experiments. The fits for the 5.18 MeV transition included $1/2^+$ resonances at 0.259 and 1.446 MeV and a $3/2^+$ resonance at 0.987 MeV. The fits of the transition to the 6.18 MeV state included $1/2^+$ resonances at 0.259 and 1.446 MeV, $3/2^+$ resonance at 0.987 MeV and an external direct capture contribution, which interferes with the two $1/2^+$ resonances.

This paper also includes an analysis of the transition to the 5.24 MeV state, fitting an exponential, representing the external direct capture contribution, to the data. A reanalysis of the transition to the 6.79 MeV state was also performed using the LUNA and LENA data and a recent remeasurement of this transition for $E_{CM}=0.548-1.307$ MeV (Ref. [23]). The fits are in much better agreement with the data from Ref. [23] than the data from Ref. [20]. A summary of the components included in each analysis is shown in Table 4.2 and the results are shown in Table.4.3

There is a large discrepancy between the recent $S(0)$ estimate for the ground state transition between Ref. [16] and Ref. [17], though the data published in these papers is in excellent agreement. The authors of Ref. [18] point out that the major difference in the analyses was that the data above the 0.259 MeV resonance was not include in the analysis of Ref. [17], and suggest that this might have allowed the $S(0)$ to be higher than it should. This indicates that higher energy data is important in constraining the $S(0)$.

Transition (MeV)	Author	Resonance States (MeV)						
		-0.504	0.259	0.985	1.446	2.187	BG Pole	DC
0.00	Schröder [20]	✓	✓	✓	-	✓	-	✓
	Angulo [9]	✓	✓	✓	-	✓	5 MeV $\frac{3}{2}^+$	-
	LUNA [16, 18]	✓*	✓*†	✓*	-	✓*	6 MeV $\frac{3}{2}^+$	✓
	LENA [17]	✓*	✓†	(✓*†)	-	(✓*†)	4 MeV $\frac{3}{2}^+$	✓
6.18	Schröder [20]	-	✓	✓	✓	-	-	-
	Angulo [9]	✓	✓	✓	✓	✓	$\frac{1}{2}^+$	✓
	LUNA [16, 18]	-	✓	✓	✓	-	-	✓
	LENA [17]	✓*	✓*†	-	-	-	✓*	-
6.79	Schröder [20]	-	✓	-	-	-	-	✓
	Angulo [9]	-	✓	-	-	-	-	✓
	LUNA [16, 18]	-	✓	-	-	-	-	✓
	LENA [17]	-	✓†	-	-	-	-	✓

Table 4.2: Summary Table of recent analyses. *Proton-width fixed, † γ -width fixed.

Transition to (MeV)	Schröder [20]	Angulo [9]	Formicola [16]
0.00	1.55±0.34	0.08 $^{+0.13}_{-0.06}$	0.25±0.06
5.18	0.014±0.004	-	-
6.18	0.14±0.05	0.06 $^{+0.11}_{-0.02}$	-
6.79	1.41±0.02	1.63±0.17	1.35±0.05
Total	3.20±0.54	1.77±0.20	1.7±0.1±0.2
	Runkle [17]	Imbriani [18]	
0.00	0.49±0.08	-	
5.18	-	0.010±0.003	
6.18	0.04±0.01	0.08±0.03	
6.79	1.15±0.05	1.21±0.05	
Total	1.68±0.09	-	

Table 4.3: The results (S(0) in units of keV.b) of recent analyses of the $^{14}\text{N}(p,\gamma)^{15}\text{O}$ reaction.

4.2 R-matrix analysis

4.2.1 The ground state and 6.18 MeV transitions

Simultaneous fits to the ground state and 6.18 MeV transitions were made using the AZURE code. Included in the ground state fits were the $3/2^+$ subthreshold state at -0.504 MeV, the 0.259 MeV $1/2^+$, 0.985 MeV $3/2^+$ and the 2.187 $3/2^+$ resonances, a $3/2^+$ background pole to simulate the direct capture component and a $1/2^+$ background resonance to simulate the tails of higher energy resonances. Both background poles were at 10 MeV.

The fits for the transition to the 6.18 MeV state include the 0.259 MeV $1/2^+$, 0.985 MeV $3/2^+$ and 1.446 MeV $1/2^+$, as well as $1/2^+$ and $3/2^+$ background resonances at 10 MeV. All possible channels were included. The data in the 6.18 MeV transition does not constrain the 0.985 MeV and 1.446 MeV resonances very well.

Initial estimates of the reduced width amplitudes were made by varying them manually. During the fitting process all reduced width amplitudes were free to vary, but the narrow resonances at 7.556 MeV and 8.284 MeV were restricted to $l = 0$ channels in order to reduce the number of free parameters somewhat. This restriction did not appear to affect the minimum χ^2 in either channel, though future analysis might consider the affect of the inclusion of the $l = 2$ channels for these narrow resonances, particularly in the 6.18 MeV transition.

The energies of the background poles were fixed, as was the energy of the subthreshold state. Other level energies were free to vary, but did not vary significantly from the initial values. Sample fits are shown in Figs. 4.2, 4.3, 4.4 and 4.5.

Components of the ground state transition

The low energy S-factor in the ground state transition is the result of the interference between the tail of the subthreshold state, the 9.484 MeV $3/2^+$ resonance and the direct capture component, in this case modelled using a $3/2^+$ background pole (see Fig. 4.6).

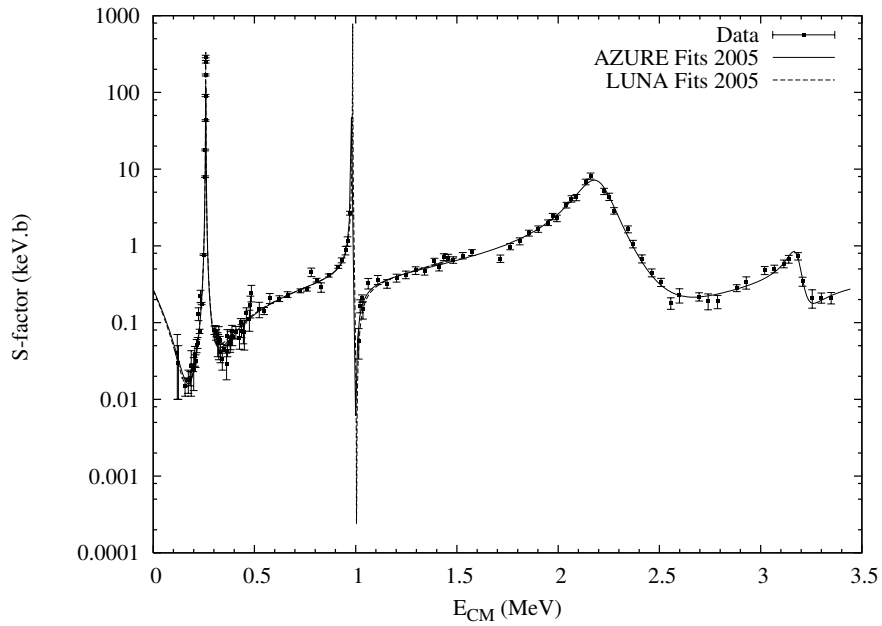


Figure 4.2: The $^{14}\text{N}(p, \gamma_{g.s.})^{15}\text{O}$ reaction. The dotted line shows the latest fits from the LUNA collaboration (Ref. [21]). The fits seem to agree well, particularly above 0.5 MeV.

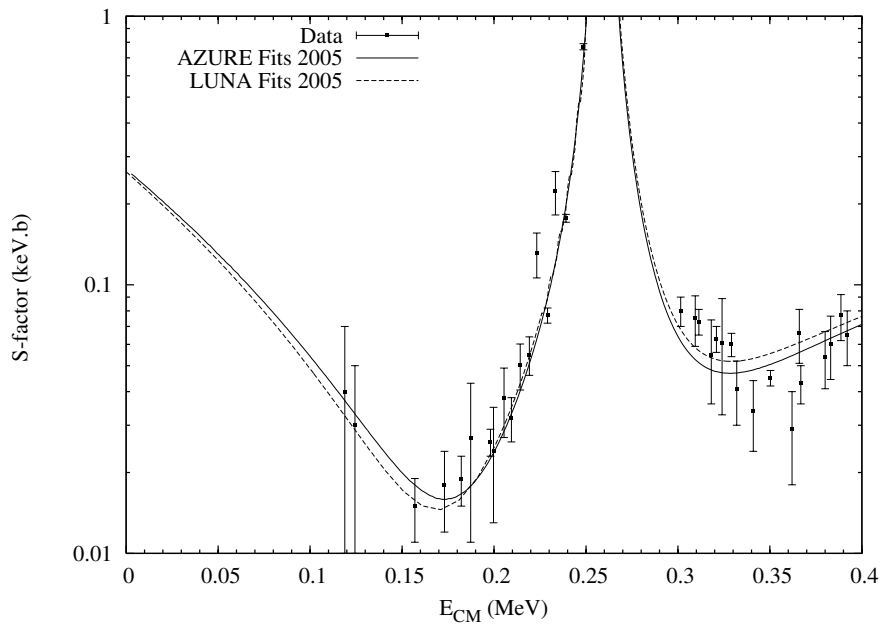


Figure 4.3: The $^{14}\text{N}(p, \gamma_{g.s.})^{15}\text{O}$ in the low energy region. The agreement is good, but not exact. The extrapolated $S(0)$ is essentially identical, but the gradient of the S-factor in the 0-0.15 MeV region is slightly different. This may be due to the use of a background pole instead of direct capture methods.

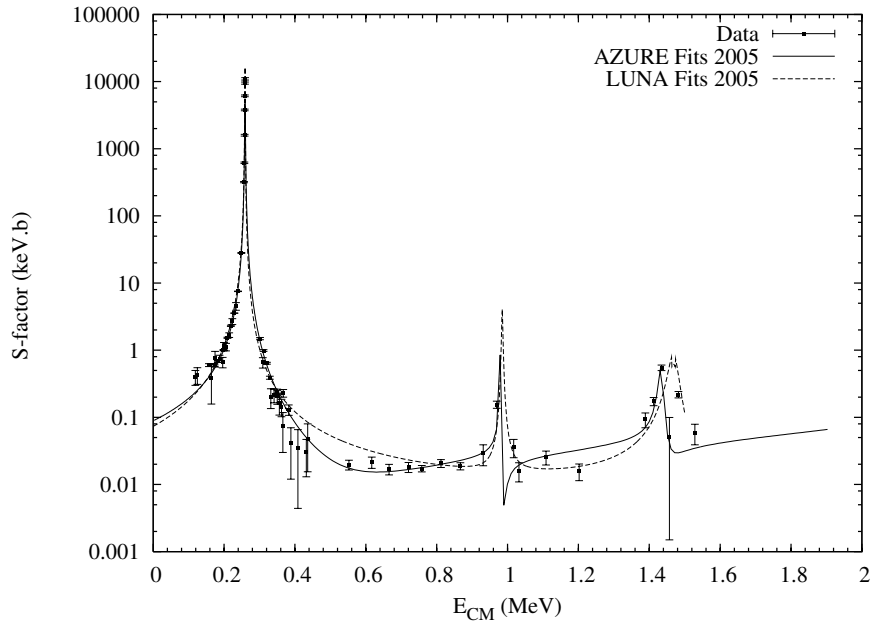


Figure 4.4: The $^{14}\text{N}(p,\gamma_{6.18})^{15}\text{O}$ reaction. The dotted line shows the latest fits from the LUNA collaboration (Ref. [21]). The AZURE fits seem to give better results in the 0.3-1.0 MeV region. This is likely to be caused by a $1/2^+$ background resonance, which seems to interfere destructively with the 0.259 MeV resonance at higher energies and constructively at lower energies.

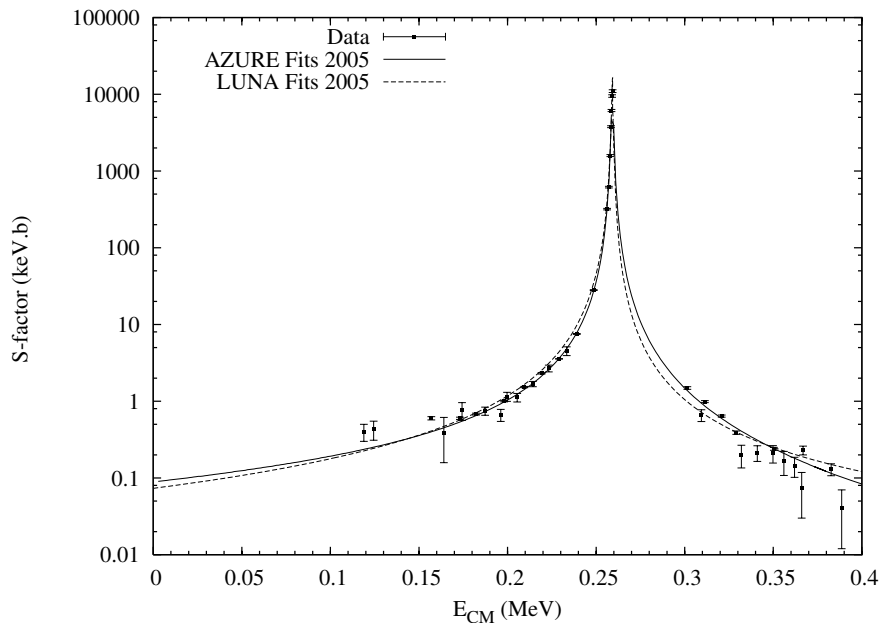


Figure 4.5: The $^{14}\text{N}(p,\gamma_{6.18})^{15}\text{O}$ S-factor in the low energy region. The effect of the interference is more clearly seen. Both the AZURE and LUNA fits seem to disregard the three lowest energy data points, going significantly below them. They would appear to suggest the fit should be somewhat higher. If there is some interference with some nonresonant process, additional data in the 0.3-1.0 MeV region might help clarify the situation.

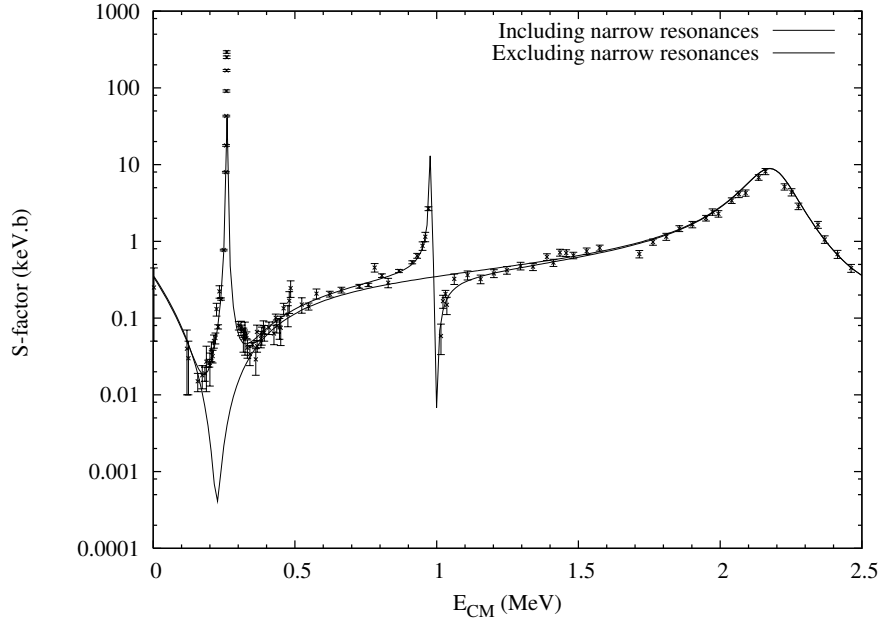


Figure 4.6: A fit to the data for the ground state transition was made. The γ reduced width amplitudes for the narrow resonances were then set to zero, leaving just the contributions from the sub-threshold state, the 9.484 MeV resonance and the background resonance. The S-factor was then recalculated using the modified fitted parameters.

It appears that the most recent data around the 0.259 MeV resonance probably does little to constrain the $S(0)$, but also indicates that additional data in the region $0.3 < E_{CM} < 0.8$ MeV may be the most effective way of constraining the ground state $S(0)$.

Estimation of $\Delta S(0)$

Other analyses (Refs. [16, 17]) have made error estimates based on best fits at different values of the radius parameter a . Here we aim to investigate the constraint on the $S(0)$ from present data (LUNA, LENA and Schröder). This is done by using a low energy data point to force the fits to take a value of $S(0)$. The χ^2 value of the fit will give an indication of the suitability of a given $S(0)$. If the $S(0)$ is well constrained by the current data, we should see a distinct minimum in the χ^2 as a function of $S(0)$, with the rate of deviation from this minimum χ^2 giving an estimate in the error. The results of this process are shown in Fig. 4.7.

From this analysis, it appears that the transition to the 6.18 MeV state is better constrained than the ground state. The ground state transition is determined by the

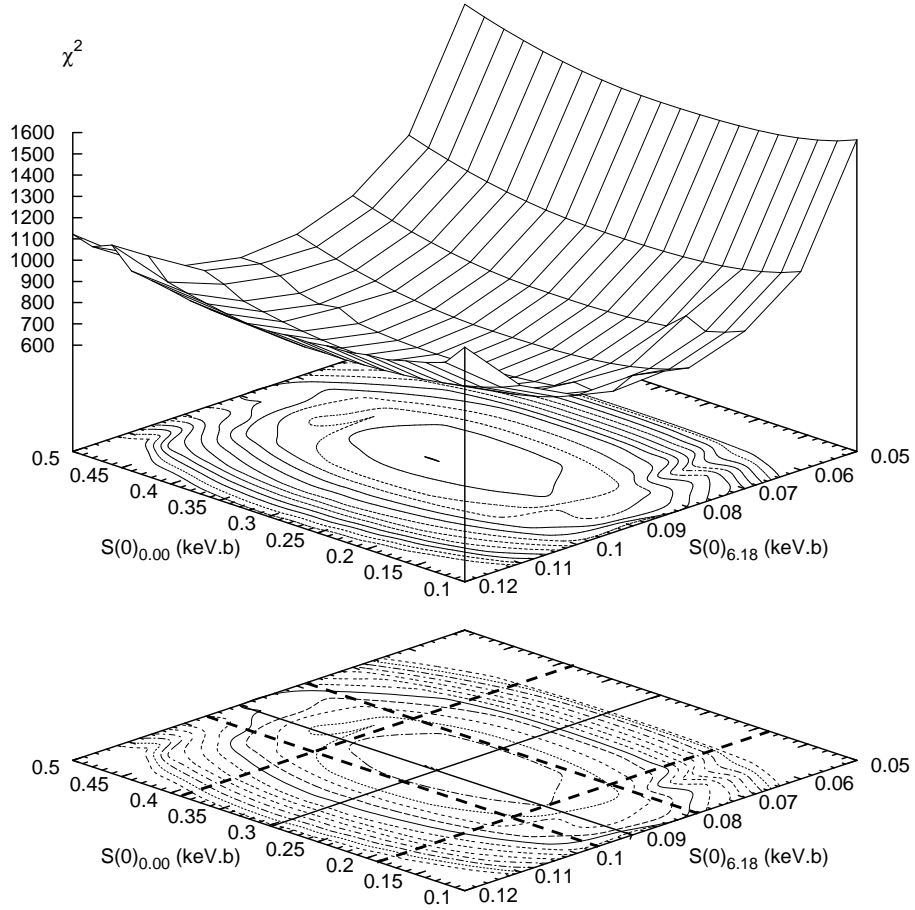


Figure 4.7: The $S(0)$ of the ground state and 6.18 MeV transitions were fixed by using a low energy data point with a small error. A minimisation was then made for these fixed $S(0)$ values. The fitted χ^2 gives an estimate of the appropriateness of a given value of $S(0)$. The contour lines are plotted for increases in the χ^2 of 5%. The error is taken as a change in the total χ^2 of 5%. The minimum χ^2/N were 2.1 and 5.7 for the ground state and 6.18 MeV transitions respectively.

interference between the subthreshold state, the background pole and the 9.484 MeV broad state. The data which constrains these contributions is essentially the data from Ref. [20], which typically has larger errors than those from Refs. [16] and [17]. Each of these states has several free parameters, so there may be considerable flexibility in the fitting.

The $S(0)$ for the 6.18 MeV transition is determined principally by the interference between the tail of the 0.259 MeV resonance and the background pole. The parameters of the 0.259 MeV resonance are well determined by the data from Refs. [16] and [17] and the data on the higher energy tail of this resonance seems to constrain the interference and hence the $S(0)$.

Note that though the χ^2/N values are > 1 , they are consistent with those published in Ref. [17]. Though Ref. [17] considered only the low energy data published in that paper, the fitted χ^2/N values were ≈ 0.54 and ≈ 5.4 for the ground state and 6.18 MeV transitions respectively. The lower χ^2/N value for the ground state transition is likely to be due to the exclusion of higher energy data.

In both channels a large proportion of the χ^2 is the result of the data points around the narrow resonance at 0.259 MeV resonance, which typically have very small errors. The fitting routine may have problems around narrow resonances, as a tiny error in the energy can result in a very large χ^2 contribution. This is a particular problem in the ground state transition, as the fitting routine will concentrate on improving the fit around the 0.259 MeV resonance, which has little bearing on the $S(0)$ value. Future fits might exclude the χ^2 contribution from the data points directly on this resonance, though those on the tails are critical in the 6.18 MeV transition.

It should be noted that the $S(0)$ values presented here were calculated at a low energy (≈ 1.3 keV), not strictly at zero energy. However, any systematic error resulting from this is expected to be < 0.0015 keV.b. This will be more significant in the 6.18 MeV transition, but is still approximately an order of magnitude smaller than the estimated error.

The energy of the background pole and its γ_p reduced width amplitude might have

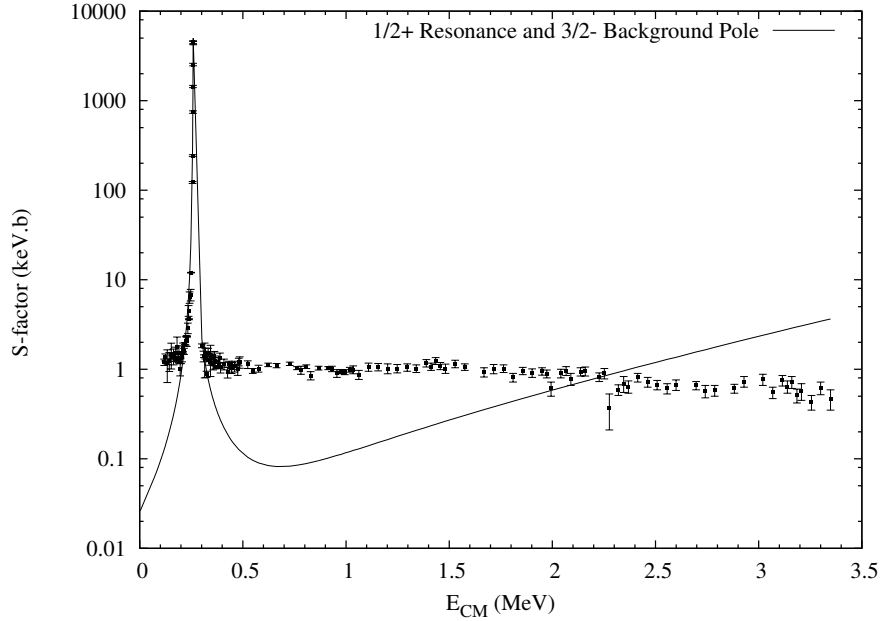


Figure 4.8: The $^{14}\text{N}(p,\gamma_{6.79})^{15}\text{O}$ using a $3/2^-$ background pole and the $1/2^+$ resonance. The $3/2^-$ background pole gives E1 radiation as expected by direct capture, but the energy dependence does not agree with the data. Changing the parameters of the background pole does not make a significant difference to the calculated energy dependence.

some affect $S(0)$ value at which the minimum χ^2 occurs. The $S(0)$ value may also be affected by the initial values of the reduced width amplitudes. Further investigation of these effects is required.

4.2.2 The 6.79 MeV transition

The transition to the 6.79 MeV state is dominated by a non-resonant component. For transitions to states at several MeV below the incident particle threshold the nonresonant capture can be reasonably simulated using a background pole. However, for the transition to the 6.79 MeV state, which is just 0.504 MeV below the threshold, the simulation is poor, as shown in Fig. 4.8.

The nonresonant channel contribution development code (see Appendix C) has been used to calculate the nonresonant contribution for the transition to the 6.79 MeV state for the $^{14}\text{N}(p,\gamma)^{16}\text{O}$ reaction. It was patched into the AZURE code with the nonresonant contribution being added to the resonant contribution where the angle-integrated

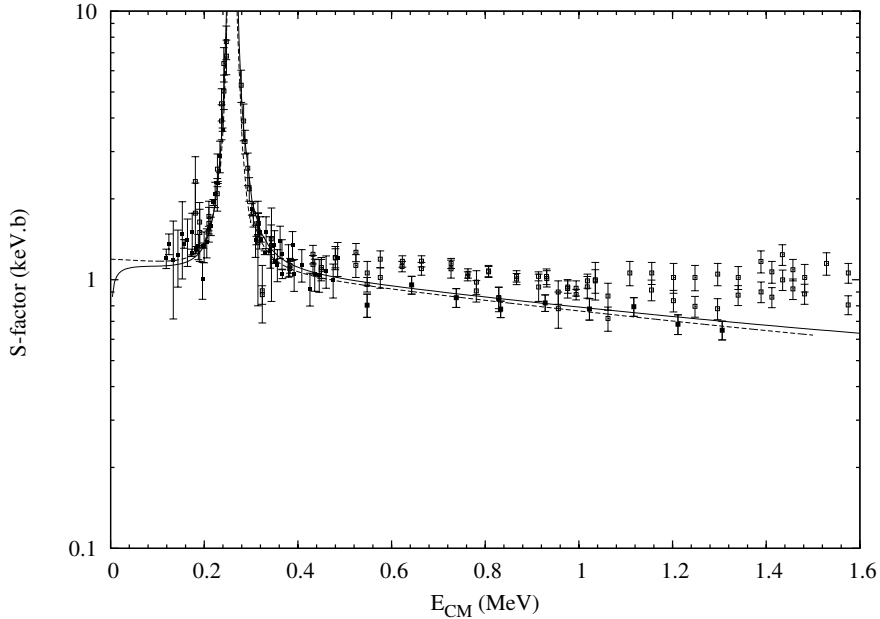


Figure 4.9: Comparison of the results from the direct capture development code (solid line) to those of Ref. [18] (dotted line). The energy dependence is in good agreement. For these calculations, $l_i = 1$, $l_f = 0$. Note the data from Refs. [16, 17, 23] is displayed as crosses, the data from Ref. [20] is displayed as faint squares. The newer data from Ref. [23] (0.5-1.4 MeV crosses) agrees better with the fit than the data from Ref. [20].

cross-section is calculated (section 30A of the code). Note that this is a patch to AZURE and can only calculate the angle integrated cross-section. Integration into the fitting procedure has not yet been completed; the fits shown use a manually varied scaling parameter for the nonresonant channel contributions. The arbitrary scaling factor includes contributions from Clebsch-Gordan coefficients and other factors which have yet to be fully implemented. A more full treatment is being developed.

The agreement with the fits of Ref. [18] is excellent above the 0.259 MeV resonance (see Figure 4.9). The deviation below the 0.259 MeV resonance is suspected to be due to numerical inaccuracies in the calculation, which should be corrected with further development of the code. At these low energies, the calculations often involve very large and very small numbers, the manipulation of which can cause problems. The agreement above the resonance is such that one would expect the agreement to be good below the resonance also, and consequently the $S(0)$ should be very similar to that of Ref. [18].

4.2.3 Elastic scattering

It was proposed that an R-matrix analysis of the elastic scattering channel might help constrain the $S(0)$ in the radiative capture channels (Refs. [19] and [28]). The AZURE code can be used to analyse the γ -channels and elastic scattering channels simultaneously, with the elastic scattering channel providing additional constraint on the γ_p reduced width amplitudes. However, the use of a background pole to simulate direct capture in the ground state transition may prevent good fits in the elastic channels when the two are fitted simultaneously. The elastic scattering fits presented here were fitted independently of the radiative capture channels.

It should also be noted that the analysis of the $^{14}\text{N}(p,p)^{14}\text{N}$ reaction was also an excellent test of the elastic scattering code. Previously the $^{12}\text{C}(\alpha,\alpha)^{12}\text{C}$ had been successfully analysed, but as both ^{12}C and α particles have 0^+ spin-parity, certain problems with the code were not highlighted. These were connected to the implementation of Eq. 1.49

In addition to the resonances included in the γ -channel fits, some extra resonances are required. The resonances used are shown in Table 4.4. Background poles were included at 5 MeV for $J^\pi = \frac{1}{2}^+, \frac{1}{2}^-, \frac{3}{2}^+, \frac{3}{2}^-$ and $\frac{5}{2}^-$. The free parameters were the reduced width amplitudes and energies of the resonances and background poles. In order to reduce the number of free parameters, the narrower resonances were restricted to $l = 0$. Further analysis should investigate the affect of this restriction. It should be noted that the broader resonances (notably at 9.484 MeV) and the background poles were not restricted. Even with these restrictions, the fits included ~ 35 free parameters.

A normalisation parameter for these fits was allowed to vary freely, with the fitted value being 0.973. This may indicate slight inaccuracies in the data, a missing component in the fits or an error in the code. The authors of Ref. [25] suggest that some beam spread may be present in the data, though do not specify how much. The target integration code of AZURE was used to help correct this. A spread of 5 keV was found to improve the fits considerably, but this may not be the most appropriate value. It may be difficult to improve the fits, particularly around the narrow resonances, due to this energy spread.

Level (MeV)	J^π	Resonance Energy (MeV)
6.793	$\frac{1}{2}^+$	-0.504
7.556	$\frac{1}{2}^+$	0.259
8.284	$\frac{3}{2}^+$	0.987
8.748	$\frac{1}{2}^+$	1.451
8.92	$\frac{1}{2}^+$	1.62
8.92	$\frac{3}{2}^+$	1.62
8.98	$\frac{3}{2}^-$	1.68
9.484	$\frac{1}{2}^+$	2.187
9.488	$\frac{3}{2}^-$	2.1918
9.609	$\frac{3}{2}^-$	2.312
9.662	$\frac{1}{2}^-$	2.365

Table 4.4: Table of resonances present in the $^{14}\text{N}(p,p)^{14}\text{N}$ elastic scattering cross-section.

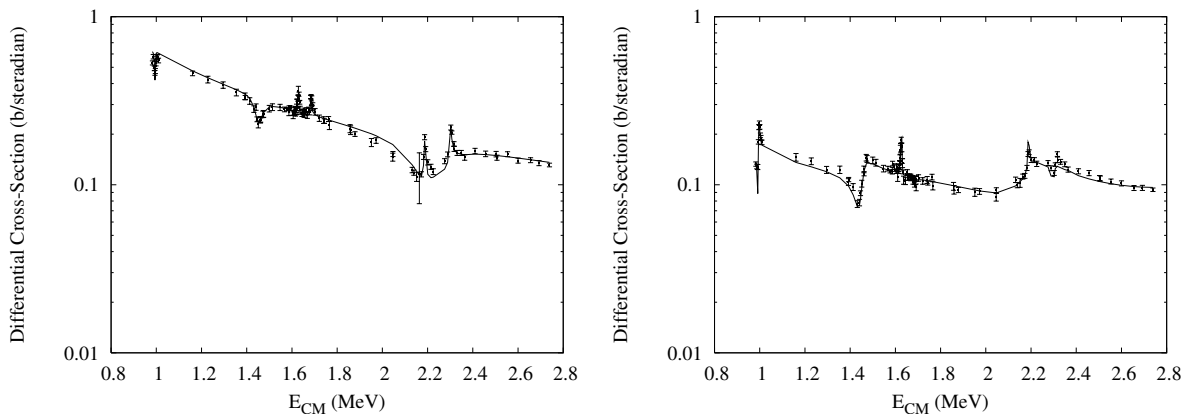


Figure 4.10: Sample of elastic scattering fits for $\theta=70^\circ$ and $\theta=153^\circ$. The χ^2/N value for these fits was 4.00.

Examples of elastic fits are shown in Fig. 4.10.

The elastic scattering fits may offer some additional constraint on the γ_p reduced width amplitudes, though more analysis is required. The ground state $S(0)$ is determined by the sub-threshold tail, the 9.484 MeV $3/2^+$ resonance and the direct capture component. The subthreshold state was removed from the fits shown in Fig. 4.10 and a calculation made. The result is shown in Fig. 4.11. This shows that the 6.79 MeV state is required for the elastic channel fits, so the elastic channel could offer constraint on the γ_p of this state which is crucial for the ground state γ -ray transition. Similarly, the 7.556 MeV

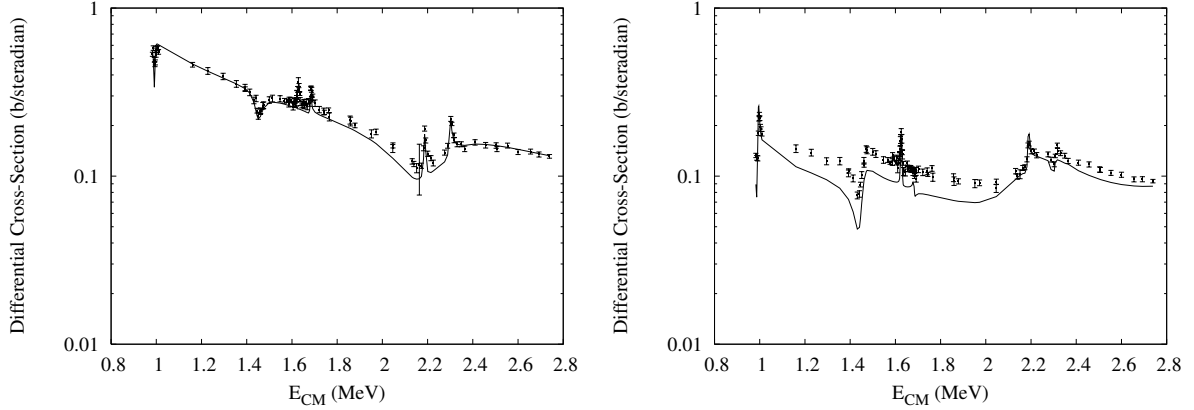


Figure 4.11: Sample elastic fits at $\theta=70^\circ$ and $\theta=153^\circ$, with the subthreshold state contribution removed. The subthreshold state clearly has an effect in the energy range of this data, with the contribution being more important at larger angles.

state is required for the elastic fits, though this state seems to be well constrained by the γ -channel data.

We note that the flat areas in the measured cross-section should be largely resulting from Coulomb scattering alone. However, the importance of the sub-threshold and 7.556 MeV states to the elastic scattering can be seen by comparing the Coulomb scattering calculation alone, to a calculation including both Coulomb scattering and these resonances. This is shown in Fig. 4.12.

The elastic channel requires that the 9.484 MeV state has both $l = 0$ and $l = 2$ components, meaning that both components should be taken into account in the ground state transition. If the 9.484 MeV state is constrained to just $l = 0$, poorer fits are attained, particularly at larger scattering angles (shown in Fig. 4.13). This was suggested by the authors of Ref. [9], though they made the assumption that the $l = 2$ contribution was negligible.

The elastic channel might also help constrain the resonance at 1.446 MeV which appears in the transition to the 6.18 MeV state, though it is unlikely that this will affect the low energy S-factor.

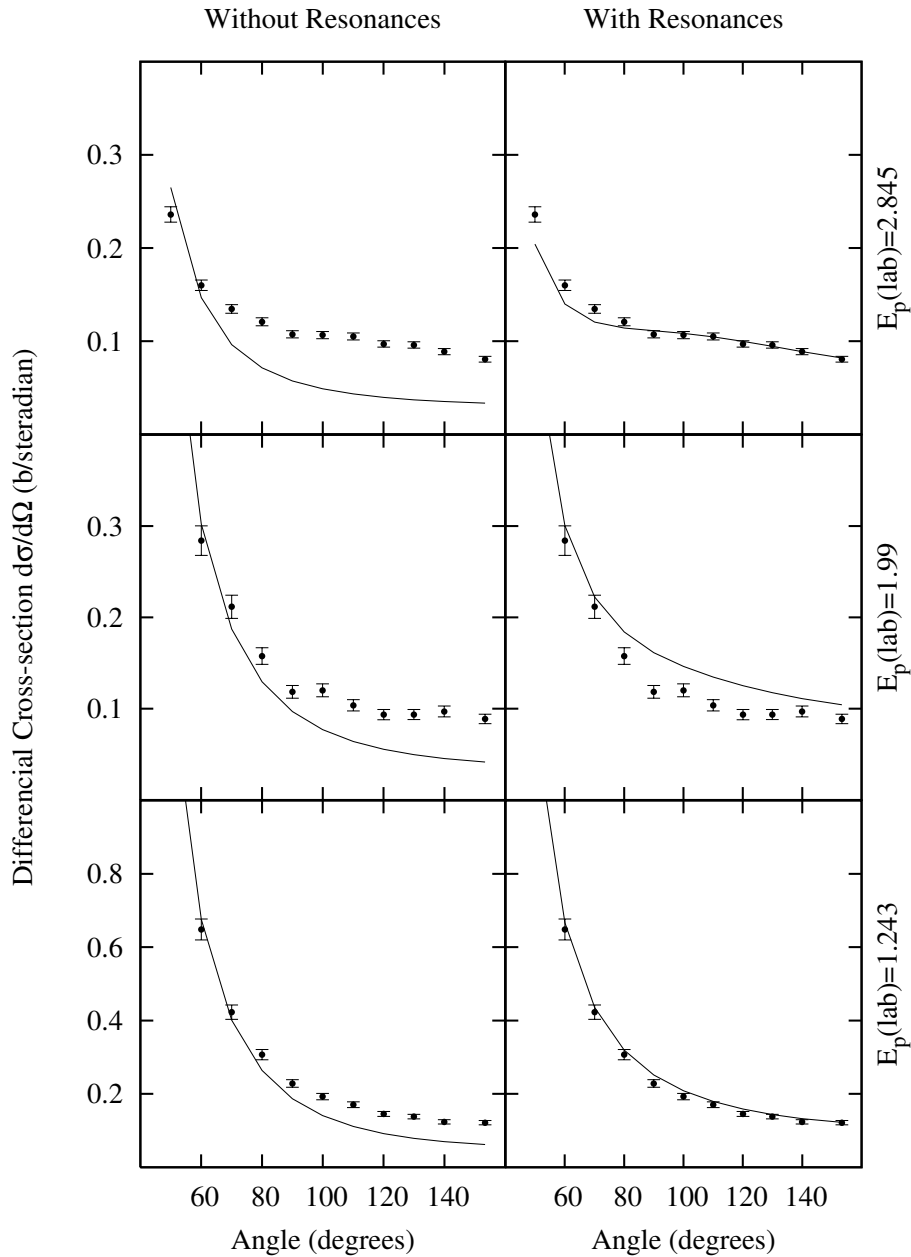


Figure 4.12: Selected angular distributions at energies where the non-resonant contributions appear to dominate, plotted for the Coulomb cross-section alone and the Coulomb cross-section with the sub-threshold and 7.556 MeV resonances. The agreement with the data improves when the resonances are included (though note that they were not fitted). The relatively poor agreement for $E_p=1.99$ MeV with the resonances included is likely to be due the broad resonance at 2.187 MeV. The contributions from the tails of the low energy resonances are more important at higher energies and larger scattering angles.

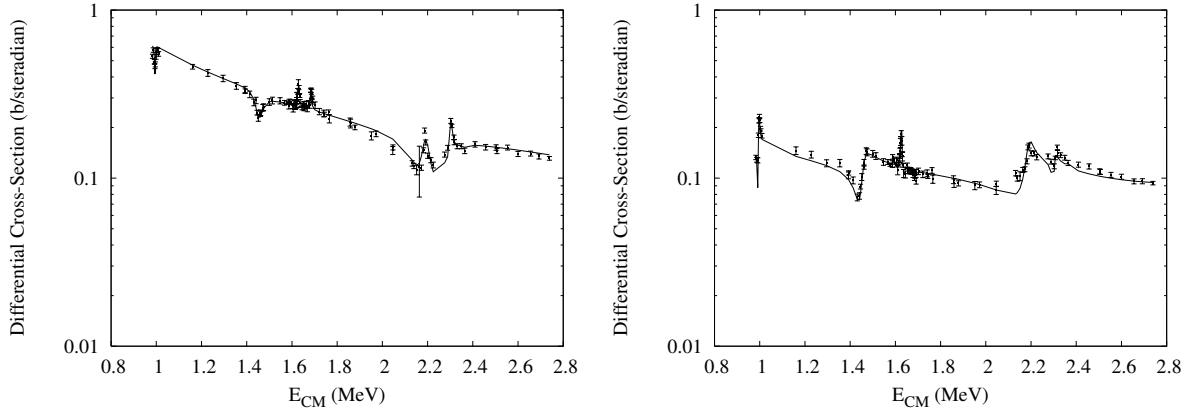


Figure 4.13: Sample elastic fits at $\theta=70^\circ$ and $\theta=153^\circ$, with the 9.484 MeV state constrained to $l = 0$. The fits around this broad resonance are poorer when the $l = 2$ component is excluded (see Fig. 4.10), particularly at larger scattering angles. The χ^2/N for these fits was 4.77, which is considerably poorer than $\chi^2/N=4.00$ if this restriction is not made.

4.3 Comparisons of results

4.3.1 Comparison of fitted $S(0)$ values

The fitted $S(0)$ values for various radiative capture transitions are presented in Table 4.5. The results for the ground state transition are in good agreement with those of Ref. [29], but not in agreement with the estimate from Ref. [17]. The analysis presented here has highlighted the importance of the higher energy data (see Fig. 4.6), the exclusion of which (as suggested by Ref. [18]) may have contributed to the large $S(0)$ value in Ref. [17].

We note that the errors for the $S(0)$ values presented here were determined using a different method to that used in Refs. [16] and [17]. In these papers, the error was determined by fitting at different values of the radius parameters and noting the spread of $S(0)$ values. Here we have chosen a fixed value for the radius parameter and attempted to estimate how appropriate the data is given a certain value of $S(0)$. If a variation in the radius a was also considered, the error estimates may be somewhat larger.

The error in the ground state transition is larger than the error offered by Ref. [16]. This might suggest that the error presented in Ref. [16] is underestimated; having con-

Transition to (MeV)	Schröder Ref. [20]	Angulo Ref. [9]	Formicola Ref. [16]
0.00	1.55±0.34	0.08 ^{+0.13} _{-0.06}	0.25±0.06
5.18	0.014±0.004	-	-
6.18	0.14±0.05	0.06 ^{+0.11} _{-0.02}	-
6.79	1.41±0.02	1.63±0.17	1.35±0.05
Total	3.20±0.54	1.77±0.20	1.7±0.1±0.2
	Runkle Ref. [17]	Imbriani Ref. [18]	AZURE
0.00	0.49±0.08	-	0.29±0.1
5.18	-	0.010±0.003	-
6.18	0.04±0.01	0.08±0.03	0.09±0.01
6.79	1.15±0.05	1.21±0.05	-
Total	1.68±0.09	-	-

Table 4.5: The results ($S(0)$ in keV.b) of recent analyses of the $^{14}\text{N}(p,\gamma)^{15}\text{O}$ reaction.

sidered only one value for the radius parameter, we have seen a large spread of possible $S(0)$ values. The apparent agreement between the fits (see Fig. 4.2) perhaps encourages this line of thought.

However, the fits of Ref. [16] fixed the γ^2 for the sub-threshold state using their fits of the 6.79 MeV transition and used a full implementation of direct capture. They also fixed the Γ_p width of the 9.484 MeV state and restricted it by using an $l = 0$ approximation. In the AZURE fits the free parameters were the γ_p and γ_γ reduced width amplitudes of each of the states and the energy of 9.484 MeV resonance, whilst also allowing an $l = 2$ contribution. The number of free parameters in the fits presented here may allow for greater flexibility.

4.4 Further constraints

4.4.1 Subthreshold state lifetime measurements

Measurements of the lifetime of the 6.79 MeV subthreshold state are presented in Ref. [4]. The lifetime a state can be related to it's experimental Γ_γ using Eq. 1.14 so limits

could be placed on the γ_γ reduced width amplitude of the subthreshold state. This is one of the critical factors determining the low-energy S-factor in the ground state transition.

However, the errors on current lifetime measurements are large and may not constrain the low-energy S-factor significantly, though they can provide a check on the fitted values.

4.4.2 Total cross-section measurements

The total cross-section for radiative capture reactions has recently been measured at the group in Bochum, Germany (see Refs. [30] and [21]). Here the cross-section for all $^{14}\text{N}(p,\gamma)^{15}\text{O}$ reactions was measured down to 70keV, which is significantly lower than the individual γ -ray transitions.

One of the main advantages of the AZURE code is that it can simultaneously analyse multiple channels. In principle all relevant γ channels could be fitted and their sum compared to the total cross-section measurements. This might help constrain the $S(0)_{total}$ and perhaps the separate transitions. In addition to the ground, 6.18 and 6.79 MeV state transitions, the transition to the 5.18 MeV state would be required as it has a contribution around the 0.259 MeV resonance, though it is not thought to have a contribution to the low energy S-factor.

However, to do this accurately AZURE would require the nonresonant code to be fully implemented to allow accurate analysis of the 6.79 MeV transition and, to a lesser extent, the ground state transition. Some further modifications would also be required so that the sum of the contributions can be compared to the data in the χ^2 calculation. Ref. [30] offered a speculative value of $S_{total}(0) = 1.3 \text{ keV}\cdot\text{b}$, which is significantly lower than the values suggested by Refs. [16] and [17], so further analysis seems essential.

4.4.3 Elastic scattering data

Initial analysis has already shown that the elastic scattering channel may help constrain the radiative capture channels, particularly the ground state transition as the γ_p reduced

width amplitudes for the sub-threshold and 9.484 MeV $3/2^+$ states appear to be constrained somewhat. It is difficult to judge the degree of additional constraint on the low-energy S-factor in the radiative capture channels from this initial analysis.

4.5 Conclusions and astrophysical implications

Astrophysical S-factor estimates

In general, the fits are in very good agreement with those of Refs. [16] and [18]. Once the direct reaction code is completed, a more complete analysis can be undertaken, involving the ground state, 5.18, 6.18 and 6.79 MeV radiative capture transitions, the recent $^{14}\text{N}(p,\gamma_{total})^{15}\text{O}$ data (Ref. [23], [21]) and the elastic scattering data. This analysis may show that the low energy S-factor is well constrained and will help guide the next generation of experiments.

Globular clusters

The $^{14}\text{N}(p,\gamma)^{15}\text{O}$ reaction rate is connected to the age of globular clusters. Globular clusters are formed from the collapse of molecular clouds and are among the oldest observable star population, thought to have formed in the first epoch of star formation. They consist of 10^4 to 10^6 stars, all of which form from the same material, so the difference in their evolutionary states is solely due to their differing initial masses.

The age of globular clusters can be determined from the Hertzsprung-Russell diagram, which plots the surface temperature of a star against its luminosity. The end of hydrogen burning is marked by a stars transition off the main sequence branch, so as the cluster ages the main-sequence branch will become gradually depopulated of stars. The estimate of the age is gauged by calculating the time it would take for the cluster to evolve to its current form (see Refs. [31, 32, 33]).

According to these rates should increase by 0.7-1 Gyr (Ref. [29]). Ref. [34] suggests the age could increase by 0.5-1.0 Gyr, depending on the methods for determining the turn-

off luminosity and cluster metallicity. Ref. [17] state that the age of the main-sequence turnoff is 0.8 Gy older than previously thought. The estimates of the age of globular clusters represents a lower limit on the age of the universe, as they cannot possibly be older than the universe itself.

Solar neutrinos

Reactions in the p-p chain and CNO cycles in the Sun produce neutrinos which can be observed on Earth. When the first measurements of solar neutrinos were made, it was discovered that only 1/3 of the expected flux was detected. This large disagreement between experiment and theory came to be known as the solar neutrino problem. The problem was solved with the idea of neutrino oscillations; the neutrinos change flavour during the journey to Earth.

The theoretical predictions for the number of solar neutrinos must carefully account for how hydrogen is burnt in the Sun. Change to the $^{14}\text{N}(p,\gamma)^{15}\text{O}$ reaction rate has a direct effect on the number of neutrinos produced by the CNO cycle in the Sun. This affect is important despite the fact that the CNO cycle only accounts for $\approx 1.5\%$ of energy production. The new S-factors alleviates, though does not eliminate, the slight discrepancy between chlorine detector measurments and model predictions (see Ref. [34]).

Improvement of future fits

The analysis presented here is incomplete, but it has been an excellent test of the AZURE code and provided useful insight into the $^{14}\text{N}(p,\gamma)^{15}\text{O}$ reaction. The ideal situation would be to analyse all possible γ -channels, the (p,γ_{total}) data and the elastic scattering channel simultaneously, implementing full direct capture. The largest error is in the ground state transition, which would benefit most from the inclusion of elastic scattering data. A monte carlo error analysis could provide a better estimate of the errors for each transition. The affect of changing the radius parameter should also be included in this analysis. This complete analysis would be an excellent guide to future experiments.

The preliminary fits to the elastic channel indicate that there may be some benefit from new elastic scattering measurements, particularly on the γ_p reduced width amplitude of the subthreshold state. They may also help constrain the contributions from $l = 0$ and $l = 2$ for the 9.484 MeV $3/2^+$ resonance present in the ground state radiative capture transition.

The AZURE code currently lacks the nonresonant capture elements required. Improvements should also be made to allow true extrapolations to zero energy, as there is currently a limit on the accuracy at very low energies (approximately 1.3 keV). This could be done by improving the accuracy of critical variables or by introducing an additional extrapolation routine.

Also of benefit would be a complete multi-channel code to convert R-matrix reduced width amplitudes to experimental partial widths using the alternative parametrisation reported in Ref. [8]. This would make finding initial reduced width amplitude values easier, allow more direct comparisons to other fits and be an excellent check on the AZURE code. Such a code could be integrated into AZURE to provide experimental partial widths as output. This would also allow easier implementation of limits on R-matrix parameters from limits on experimental widths, which would have been beneficial in this analysis.

The analysis described above may go some way in improving the accuracy of $S(0)$. Further measurements below 0.2 MeV may be of benefit, but also measurements in the 0.3-0.8 MeV range. Further analysis of the current elastic scattering data may indicate the benefit of future $^{14}\text{N}(p,p)^{14}\text{N}$ measurements.

Chapter 5

$^{15}\text{N}(\text{p},\gamma)^{16}\text{O}$ and $^{15}\text{N}(\text{p},\alpha)^{12}\text{C}$ reactions

The $^{15}\text{N}(\text{p},\gamma)^{16}\text{O}$ and $^{15}\text{N}(\text{p},\alpha)^{12}\text{C}$ reactions are the branching point between the first and second CNO cycles, and though they have been measured several times, they have never been analysed using a multi-channel R-matrix approach. This analysis is a good test of the particle and radiative capture code and demonstrates the benefit of multi-channel fitting.

5.1 Summary of experimental measurements

5.1.1 The ^{16}O compound nucleus

The level structure of the ^{16}O compound nucleus for the energy range of interest is shown in Fig. 5.1. The Q-value for the $^{15}\text{N}+\text{p}$ reactions is +12.1276 MeV and is +7.167 MeV for the $^{12}\text{C}+\alpha$ reactions. The 1^- levels at 12.44 and 13.09 MeV and their interference dominate the low energy cross-section in both reactions. The interference is constructive in the low energy region in the γ -channel, but destructive in the α_0 -channel. There is thought to be some non-resonant contribution in the γ decay channel (Ref. [35]).

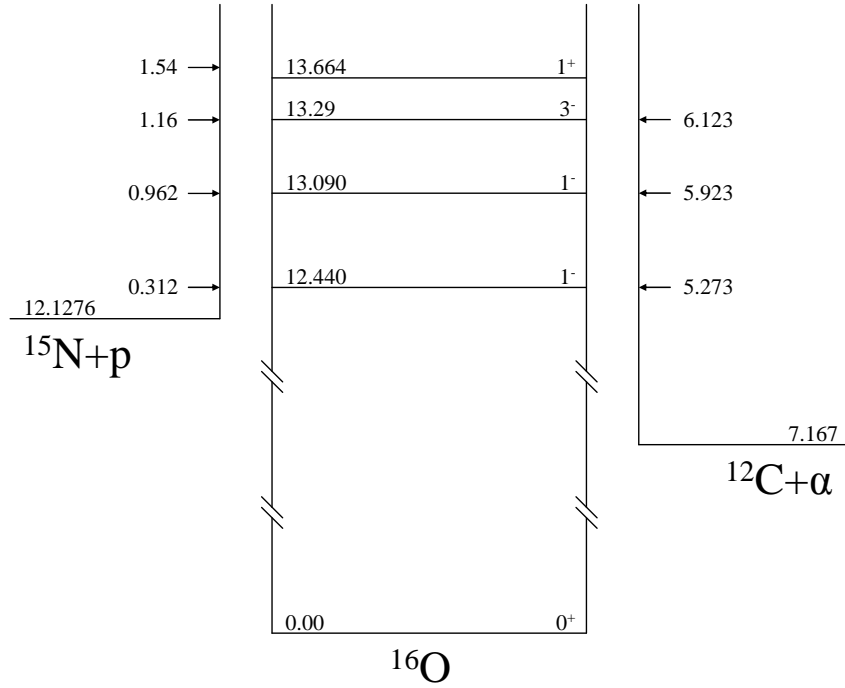


Figure 5.1: The ^{16}O level scheme, showing the levels involved in the $^{15}\text{N}+p$ reactions. The 12.44 and 13.09 MeV 1^- levels are present in both reactions. The 13.664 MeV 1^+ level is present in the γ channel and the 13.29 MeV 1^- level is present in the α_0 channel, though neither appear to have a significant contribution to the low-energy cross-section.

5.1.2 Experimental measurements

The authors of Ref. [36] measured the $^{15}\text{N}(p,\alpha_0)^{12}\text{C}$ reaction at $\theta_\alpha=90^\circ$ for proton energies 0.1-0.8 MeV and at $\theta_\alpha=138^\circ$ for $E_p=0.8-1.6$ MeV. They assumed isotropic angular distributions.

The authors of Ref. [37] measured the differential cross-section of $^{15}\text{N}(p,\alpha_0)^{12}\text{C}$ at $0.087 \text{ MeV} \leq E_{CM} \leq 0.39 \text{ MeV}$ using a silicon detector placed at $E_{lab}=135^\circ$. The cross sections were normalised to the peak cross-section of 90 mb at $E_p \approx 0.350 \text{ MeV}$. This was then converted to angle-integrated S-factor using angular distribution data to parametrize the angular dependence.

The authors of Ref. [38] measured the $^{15}\text{N}(p,\alpha_0)^{12}\text{C}$ excitation function using a 360keV accelerator with a gas target and five or six Si detectors positioned in the angular range $\theta_{lab}=22.5^\circ$ to 150° . Measurements with solid targets had suffered from reduced accuracy at low energies due to target deterioration. Higher energy measurements were made

Dataset	E_p α -channel (MeV)	E_p γ -channel (MeV)
Schardt 1952 [36]	0.1-1.6	-
Hebbard 1960 [40]	-	-
Brochard 1973 [39]	0.25-1.10	0.22-1.23
Rolfs 1974 [35]	-	0.15-2.50
Zyskind 1979 [37]	0.093-0.418	-
Redder 1982 [38]	0.077-0.91	-

Table 5.1: Energy ranges of the data sets for the $^{15}\text{N}(p,\gamma_0)^{16}\text{O}$ and $^{15}\text{N}(p,\alpha_0)^{12}\text{C}$ reactions.

using a 1 MV accelerator using an Silicon detector at $\theta_\alpha=90^\circ$. The angular distribution measurements indicated that the observed yield at 90° represented the angle-integrated reaction yield. The absolute cross-section was determined relative to the Rutherford scattering cross-section at $E_p=0.3534$ MeV for $\theta_{lab}=22.5^\circ$ to 150° .

The authors of Ref. [35] measured the $^{15}\text{N}(p,\gamma_0)^{16}\text{O}$ reaction at energy $E_p=0.15$ -2.5 MeV and angle $\theta_\gamma=45^\circ$ using a Ge(Li) detector. The $^{15}\text{N}(p,\alpha_1\gamma_1)^{12}\text{C}$ reaction was also measured and the observed relative intensity of γ -rays used to normalise the $^{15}\text{N}(p,\gamma_0)^{16}\text{O}$ reaction. The γ -rays are assumed to be nearly isotropic, so only small corrections were required to obtain the angle-integrated cross-section.

The (p,γ_0) and (p,α_0) reactions were also measured by the authors of Ref. [39]. The α -channel data is in very good agreement with the data published in Refs. [37] and [38]. However, there appears to be a disagreement between the γ -channel data of Refs. [39] and [35], particularly around the 12.44 MeV 1^- resonance, where the Ref. [39] set is somewhat lower than that of Ref. [35]. The data from Ref. [39] was scanned from the paper, which may have introduced some error. As the Ref. [35] data set covers a wider range of energies, it was decided to use this dataset alone in the fitting that follows. The energy ranges of these measurements are shown in Table 5.1.

5.1.3 Previous analysis

The authors of Ref. [36] analysed their α -channel data using single level Breit-Wigner shapes, estimating the effects of interference by taking the difference of the amplitudes.

The extrapolation to low energies was made by approximating the tail of the cross-section curve by an exponential. They note that their extrapolated value may be a factor of two too large due to interference effects. The authors of Ref. [40] analysed their γ -channel data using a multi-channel two level Breit-Wigner expression given in Ref. [2], but no additional direct capture contributions.

The authors of Ref. [35] fit their data for the $^{15}\text{N}(p,\gamma_0)^{16}\text{O}$ reaction using a two level Breit-Wigner calculation and a contribution from direct capture, as described by Ref. [12]. The inclusion of the direct capture component gives a much better fit to the data and results in an $S(0)$ which is a factor of two higher than the earlier estimates of Ref. [40]. They note that the S-factor at stellar energies is primarily constrained by the data points on the tails of the two 1^- resonances, particularly the region of interference between them.

The authors of Ref. [37] fit their $^{15}\text{N}(p,\alpha_0)^{12}\text{C}$ data using a two-level Breit-Wigner calculation in a similar way to Ref. [35]. The region below 0.1 MeV was fit using a second order polynomial. The uncertainty was determined from the relative uncertainties in the measured data points and the absolute uncertainty in the overall normalization.

The authors of Ref. [38] analysed their data with a two-level Breit-Wigner calculation. They note that the observed angular distributions suggest some additional, slowly varying amplitude in the reaction mechanism, resulting either from a broad 0^+ or 2^+ background resonance or a direct capture mechanism. They state that the background mechanism is weak and has no affect on the angle-integrated cross-section.

The $S(0)$ is dominated by the tail of the 12.44 MeV 1^- resonance, which interferes destructively with the 13.09 MeV 1^- resonance on the high energy side (between the resonances) and constructively below the resonance. The 12.44 MeV 1^- resonance interferes constructively with a non-resonant contribution on the low energy side. This effect was taken into account in Ref.[35] but not in Ref. [40] and may increase the $S(0)$ by a factor of two. Table 5.2 summarises the results of recent analyses.

Dataset	$S(0)_\gamma$ (keV.b)	$S(0)_{\alpha 0}$ (MeV.b)
Schardt 1952 [36]	-	64
Hebbard 1960 [40]	32	72
Brochard 1973[39]	-	-
Rolfs 1974 [35]	64 ± 6	-
Zyskind 1979 [37]	-	78 ± 6
Redder 1982 [38]	-	65 ± 4

Table 5.2: $S(0)$ values from previous analyses.

5.2 R-matrix analysis

A multi-channel R-matrix analysis of the $^{15}\text{N}(p,\gamma_0)^{16}\text{O}$ and $^{15}\text{N}(p,\alpha_0)^{12}\text{C}$ reactions was made using the AZURE code. The γ -channel included the 0.312 MeV and 0.962 MeV 1^- resonances and the 1.54 1^+ resonance. The α -channel included the 0.312 MeV and 0.962 MeV 1^- resonances and the 1.16 MeV 3^- resonance. Both channels included 1^- and 3^- background poles at 15 MeV. All reduced width amplitudes and level energies were left as free parameters.

5.2.1 Identifying the correct minimum

In any multi-parameter fitting, one must be careful to avoid local minima in χ^2 . MINUIT is an excellent fitting routine, but it can get caught in local minima. During this analysis it was suggested that there might be local minima in the fits for the $^{15}\text{N}+p$ reactions, stemming from the γ_p and γ_{α_0} reduced width amplitudes for the 13.09 MeV 1^- state. Certain combinations of these parameters gave excellent fits in the $^{15}\text{N}(p,\alpha_0)^{16}\text{O}$ channel, but much poorer fits in the $^{15}\text{N}(p,\gamma_0)^{16}\text{O}$ channel, with the greatest difference coming between the two 1^- resonances. Examples of these fits are shown in Figs. 5.2 and 5.3.

Fits were made for fixed values for the γ_p and γ_α reduced width amplitudes of the 13.09 MeV 1^- state, with all other parameters varying freely, and the final χ^2 was recorded for each of the channels. This is plotted in Figures. 5.4 and 5.5. If local minima exist as suspected, we should see minima in the χ^2 at the appropriate parameter values, with at

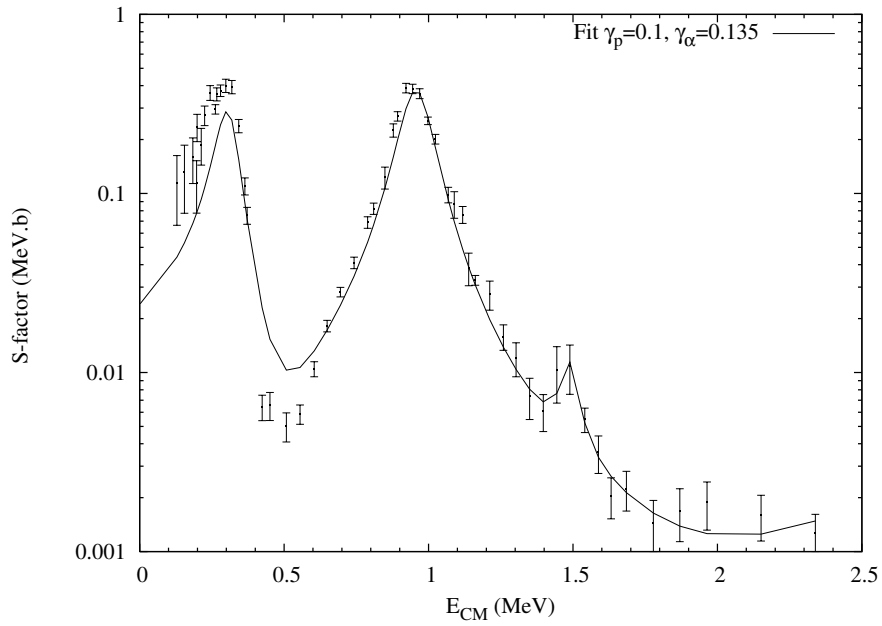


Figure 5.2: For this combination of parameters, the fit in the γ -channel is poor in the region in between the resonances, though is reasonable elsewhere ($\chi^2/N \sim 12.9$). Note that the extrapolated $S(0)$ is significantly lower than previous results $\approx 24 \text{ keV.b}$ as opposed to previous results of $\approx 65 \text{ keV.b}$.

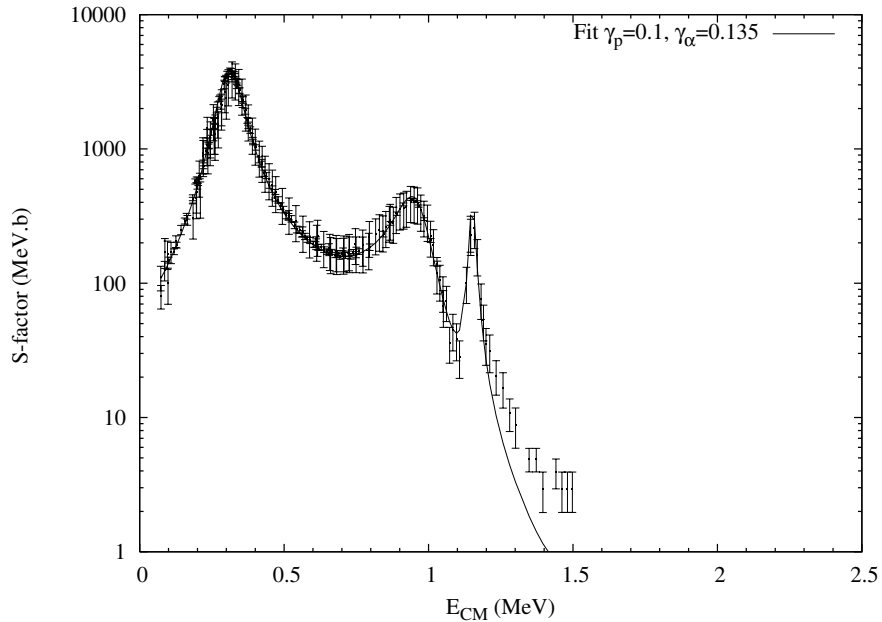


Figure 5.3: For this combination of parameters the fits in the α -channel appear to be very good ($\chi^2/N \approx 1.2$). As the α -channel is entirely determined by the γ_p and γ_α reduced width amplitudes, we might assume that these parameters must be correct due to the reasonable quality of the fits.

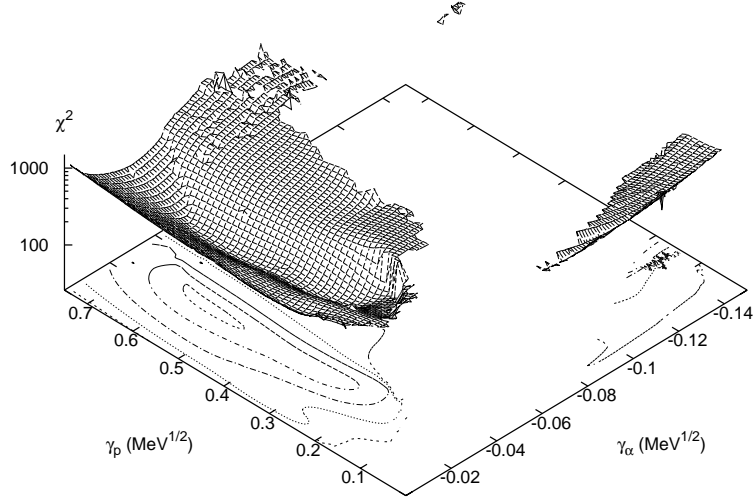


Figure 5.4: χ^2 for the γ -channel for different reduced width amplitude values γ_p and γ_α . We see a minimum on the left hand side of the plot, for $\gamma_p \approx 0.55$ and $\gamma_\alpha \approx 0.02$. The contours are to guide the eye and are spaced such that each one is a factor of 1.5 larger than the previous, with the lowest being a factor of 1.5 larger than the lowest χ^2 .

least two minima in the α -channel and one less minimum in the γ -channel.

It is not immediately obvious why the γ -channel should be affected by changes in the γ_α reduced width amplitude. In terms of the Breit-Wigner resonance formula (see Eq. 1.11), the cross-section is related to the product of the widths for a reaction divided by the sum of the widths squared. Each level has widths Γ_p , Γ_γ and Γ_α . In this case the proton- and α -widths are of the same order of magnitude, but the γ -channel widths are much smaller. The total width will be approximately equal to $\Gamma_p + \Gamma_\alpha$ and the Γ_γ width will act like a scaling parameter in the γ -channel, whilst having a negligible effect on the α -channel. The α reduced width amplitude will be as critical to the γ -channel as it is to the α -channel.

This might also explain why the α -channel has a deeper, sharper minimum. The shape of the 13.09 MeV resonance in the α -channel is entirely determined by the γ_p and γ_α reduced width amplitudes which are fixed. The fitting routine therefore has no control over this resonance in this channel. In the γ -channel the resonance shape is determined

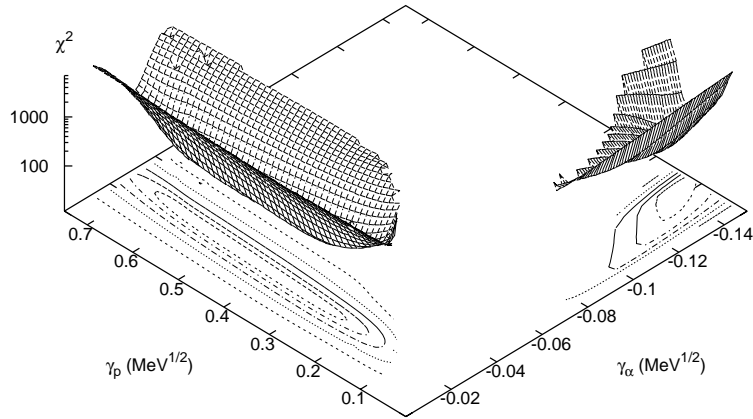


Figure 5.5: Map of χ^2 in the α -channel. Here we see two minima, of similar depth. Notice that the left minimum is significantly steeper than in the γ -channel, indicating that the parameters are better constrained by the data in the α -channel. Each contour is a factor of two larger than the previous.

by γ_p and γ_α , but also the γ_γ reduced width amplitude, which gives the fitting routine more flexibility to improve the χ^2 .

The vast majority of reduced width amplitude combinations do not give a good fit to the data and those above a certain χ^2 are not plotted (though all combinations in the range of the plot were tried). However, there are two definite minima in the α -channel. Notice that the left minimum is elongated over a wide range of γ_p values, but narrower in γ_α , which indicates that the γ_α reduced width amplitude may be better constrained by the current data than the γ_p . If one were to simultaneously analyse an elastic scattering reaction, it would seem that there would be more benefit analysing the $^{15}\text{N}(p,p)^{15}\text{N}$ reaction to constrain the γ_p reduced width amplitude, rather than the $^{12}\text{C}(\alpha,\alpha)^{12}\text{C}$ to constrain the γ_α reduced width amplitude.

The differences between the two minima can clearly be seen by comparing Figs. 5.7 and 5.8 to Figs. 5.2 and 5.3. Though it is difficult to tell from the plots, there was a significant improvement in the α -channel, as well as the more obvious improvement in

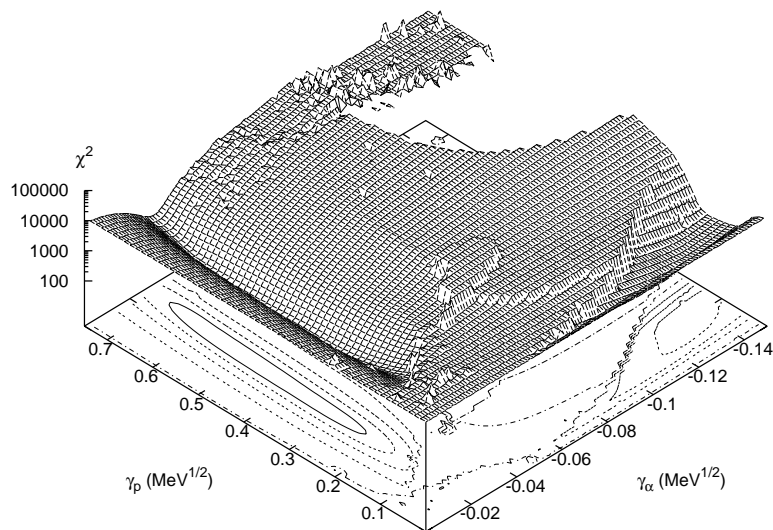


Figure 5.6: Map of χ^2 in both channels. We see that if the initial parameter values were near the right minimum, it would be difficult for the fitting routine to reach the left minimum. This would require a simultaneous factor of seven reduction in the γ_α parameter and a factor of two increase in the γ_p parameter. Incremental steps in the parameters would give no indication that the second minimum existed. Each contour is a factor of two larger than the previous.

the γ -channel.

Although it was not thought that there was a similar local minimum relating to the 12.44 MeV 1^- state, a similar scan was made to confirm this. The parameters of this state (γ_p and γ_α) were fixed at various values, a minimization was made and the χ^2 was recorded. The results are shown in Fig. 5.9. There is no indication of local minima.

5.2.2 $S(0)$ estimates

Having confirmed the correct minimum, estimates of $S(0)$ and its error are desired. Fits are made using initial parameters which will ensure the correct minimum is found. Fixing the $S(0)$ using a low energy data point with a very large error forces the minimisation procedure to take a certain $S(0)$. This procedure is done at different values of $S_\gamma(0)$ and $S_\alpha(0)$, with the χ^2 value of the fit giving an indication of the appropriateness of a given $S(0)$ value. We would expect there to be a minimum χ^2 value at the physical $S(0)$ and

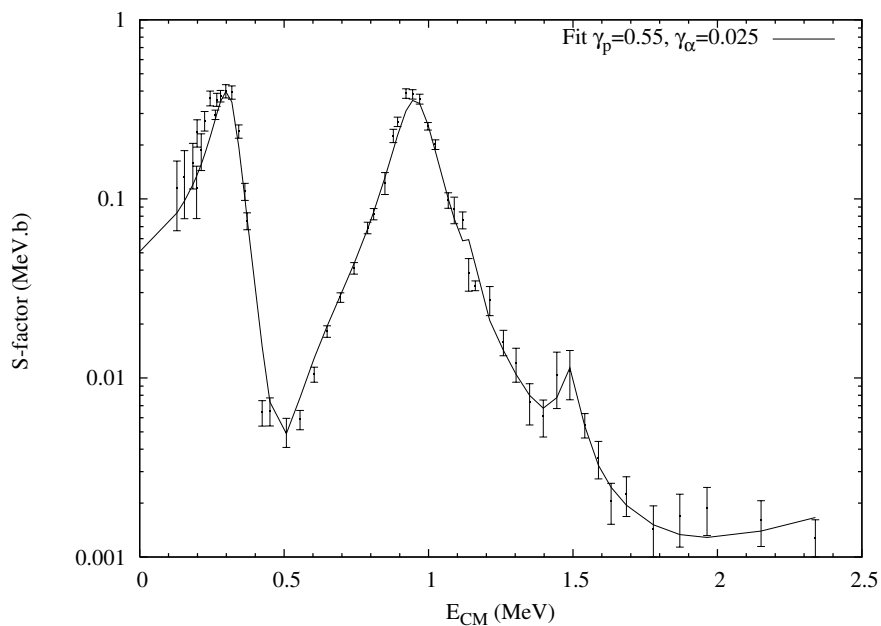


Figure 5.7: The second combination of parameters gives much better fits, particularly between the two resonances. $\chi^2/N \approx 2.93$, a factor of 4 improvement.

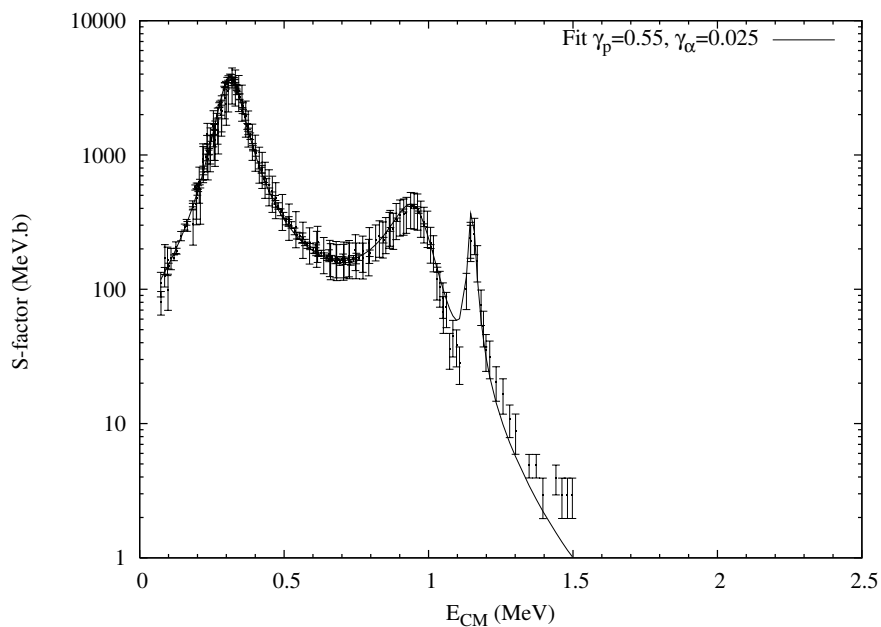


Figure 5.8: On initial inspection, the fits in the α channel are as good for the second pair of parameters as the first. However, in this case $\chi^2/N \approx 0.80$, which is a large improvement considering the already low χ^2 .

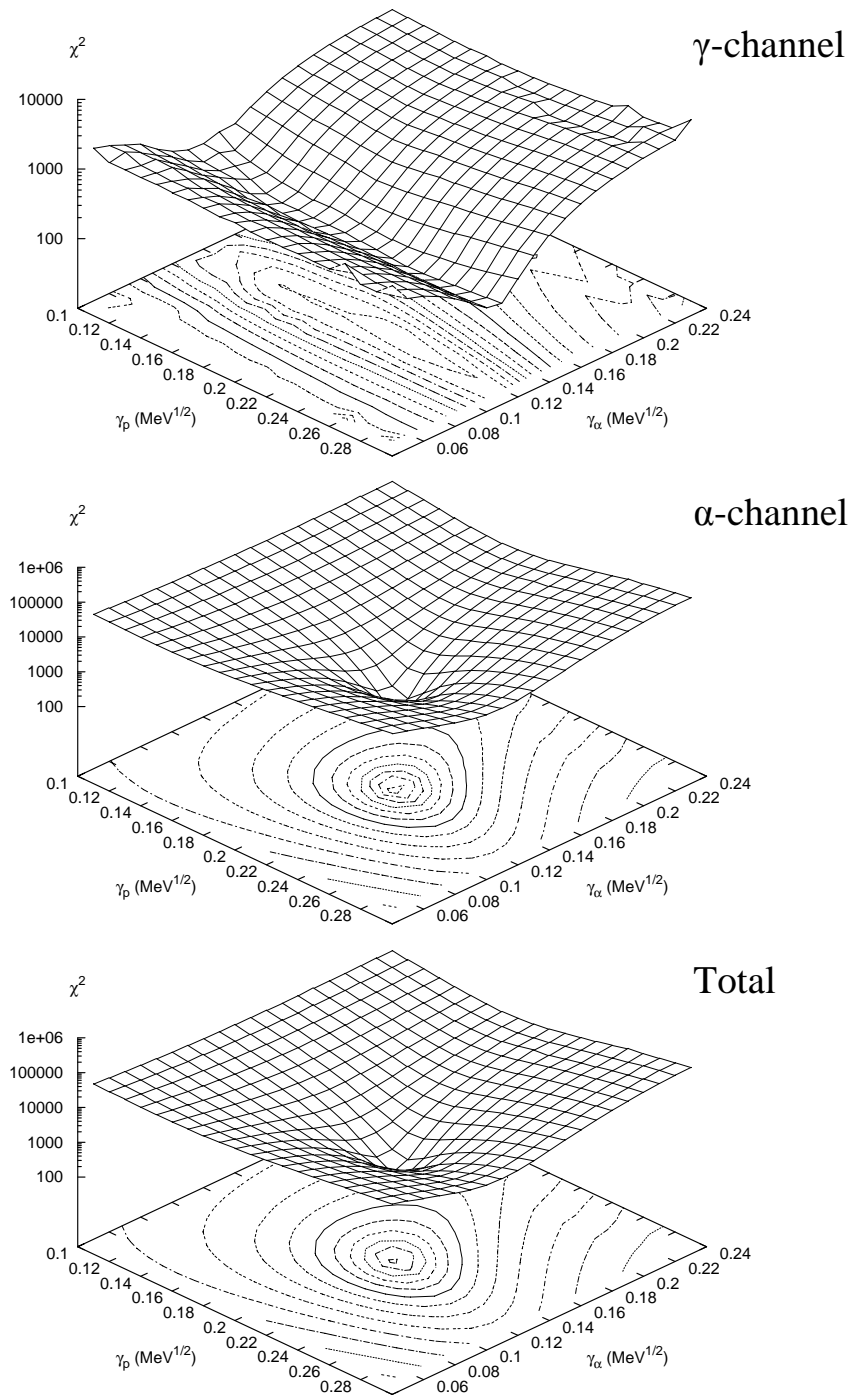


Figure 5.9: A map of χ^2 for the γ - and α -channels and the total for fits at fixed γ_p and γ_α reduced width amplitudes of the 12.44 MeV 1^- state. The γ_p parameter is less well defined than the γ_α parameter in the γ -channel, again indicating that a simultaneously analysis of the $^{15}\text{N}(p,p)^{15}\text{N}$ reaction might be more beneficial than an analysis of the $^{12}\text{C}(\alpha,\alpha)^{12}\text{C}$. However, the α -channel appears to constrain the γ_p reduced width, illustrating the benefits of multi-channel fitting. The contours shown are to guide the eye.

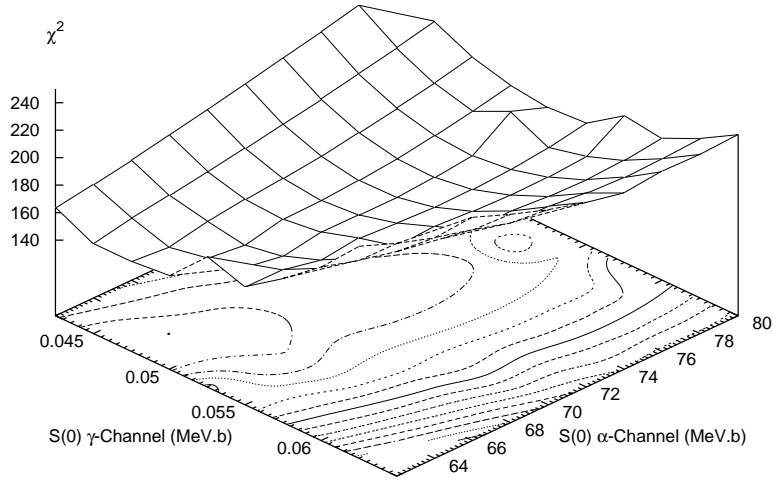


Figure 5.10: Map of χ^2 for the γ channel as a function of fitted $S(0)$. Note that the χ^2 in the γ channel is dependent on the $S(0)$ in the α channel. The minimum χ^2 occurs for $S_\gamma(0) \approx 0.048$ MeV.b and $S_\alpha(0) \approx 64$ MeV.b.

that the further from this value the higher the χ^2 . How quickly the χ^2 deviates from the minimum value will give an estimate of the error in the $S(0)$ values.

It should be noted that the χ^2 maps shown in Figures 5.10 and 5.11 are quite different. The α -channel displays exactly the behaviour we might expect; there is distinct minimum for the $S_\alpha(0)$, but no constraint of the $S_\gamma(0)$. The independence of $S_\gamma(0)$ is due to the higher weight of data in the α -channel, so this α -channel is always fitted in preference to the γ -channel.

The γ -channel is more complicated. We do see a χ^2 minimum, which rises at the extremes of $S_\gamma(0)$ in a similar way to the α -channel. However, the χ^2 in the γ -channel is not independent of the $S_\alpha(0)$, whereas the α -channel χ^2 is independent of the $S_\gamma(0)$. It is interesting to note that the $S(0)$ values deduced from the minimum χ^2 in each channel, are different to those deduced from looking at the total χ^2 , particularly in the γ -channel. This illustrates the benefits of multi-channel analysis, though perhaps suggests further analysis is required.

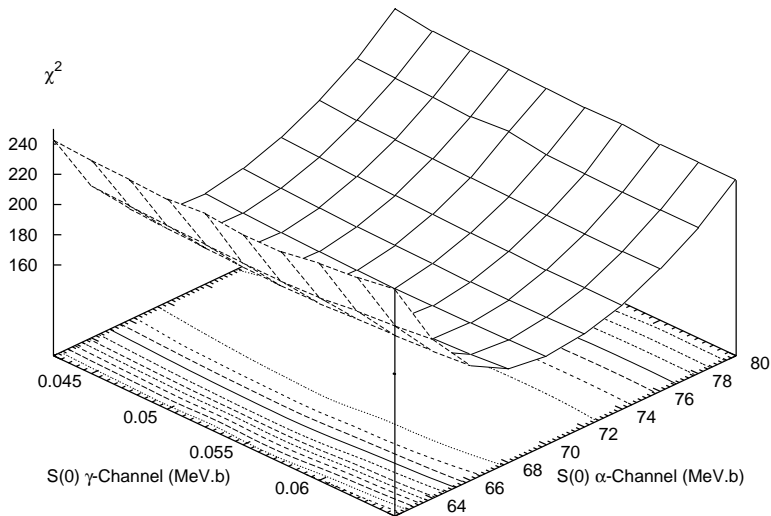


Figure 5.11: Map of χ^2 for the α -channel as a function of fitted $S(0)$ for both the α - and γ -channels. Note that the α -channel is virtually independent of the γ -channel fit. This is perhaps expected, as this channel carries more weight in the χ^2 fitting. In this case the minimum χ^2 occurs for $S_\alpha(0) \approx 69$ MeV.b and the $S_\gamma(0)$ can take a wide range of values.

5.3 Comparison of extrapolated $S(0)$

The results from the AZURE fits are shown in Table 5.3 with estimates from other publications. The $S_{\alpha_0}(0)$ is in good agreement with the most recent estimates from Ref. [38] and Ref. [37], and the weighted average estimate from Ref. [19]. It agrees well with the older estimate from Ref. [40], though it is larger than the estimate from Ref. [36]. The $S_\gamma(0)$ is lower than the most recent estimate Ref. [35]. The authors of Ref. [40] did not consider a non-resonant component, resulting in a low $S_\gamma(0)$ estimate.

The $S_\gamma(0)$ from the fits made with the AZURE code might be lower than the Ref. [35], which used Breit-Wigner resonances with a direct capture contribution, due to the usage of the background pole to model direct capture. However, as the proton threshold is 12.13 MeV above the ^{16}O ground state, the background pole should have a similar energy dependence to direct capture. A comparison is shown in Fig. 5.13.

The fit between the two 1^- resonances, where any direct capture component would have a significant effect, seems good. The AZURE fits were done simultaneously in both

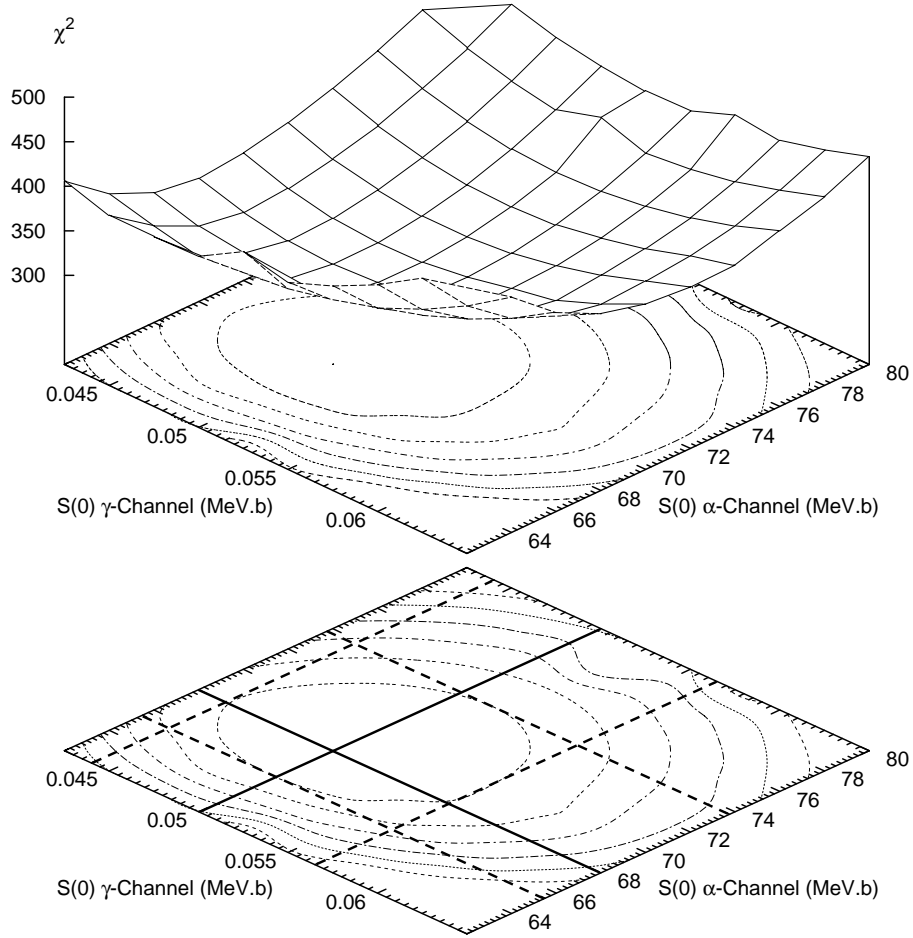


Figure 5.12: Contour plot of χ^2 in both the γ and α channels as a function of fitted $S(0)$. The minimum comes for $\chi^2 \approx 313$ and the contours increase in increments of 5% of the minimum value. The minimum χ^2 occurs for $S_\gamma(0) \approx 0.050$ MeV.b and $S_\alpha(0) \approx 68$ MeV.b.

γ - and α -channels, providing good fits in both channels. However, whilst this provides additional constraint on the parameters of the two 1^- resonances, this would not help clarify the direct capture contribution in the γ -channel.

Once the direct capture upgrade to the code is finished, the results presented here should be checked. The likely affect of the inclusion of a proper direct contribution would be to increase the estimate of the γ -channel $S(0)$ somewhat, though even a 20% increase would still lead to an estimate below the value suggested by Ref. [35].

Work	$S_{\alpha_0}(0)$ (MeV.b)	$S_{\gamma}(0)$ (keV.b)
Schardt 1952 [36]	64	-
Hebbard 1960 [40]	72	32
Brochard 1973[39]	-	-
Rolfs 1974[35]	-	64 ± 6
Zyskind 1979 [37]	78 ± 6	-
Redder 1982 [38]	65 ± 4	-
Adelberger 1998 [19]	$67.5 \pm 4^*$	-
AZURE R-matrix	$68.0^{+5.5}_{-2.5}$	50^{+7}_{-6}

Table 5.3: Summary of the $S(0)$ estimates from the literature and the current AZURE values. * weighted average value of previous results

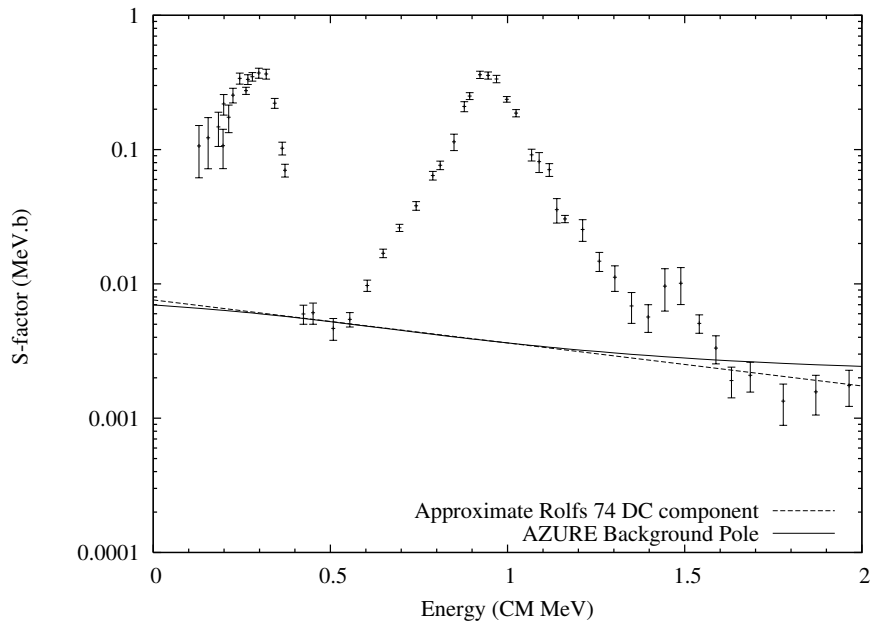


Figure 5.13: The AZURE background pole compared to an estimate of the direct capture contribution of [35]. The agreement is very good between 0.3 and 1.3 MeV. Below 0.3 MeV the background pole is slightly lower than the direct capture estimate, which may cause the AZURE estimate to be lower than that of Ref. [35]. The difference is $\sim 9\%$ at 0 MeV. Above 1.3 MeV the background pole deviates significantly from the direct capture estimate, though this is unlikely to have a large effect on the fitting due to the larger errors on these data points.

5.4 Conclusions and astrophysical implications

S-factors

The R-matrix analysis presented here has verified the $S(0)$ in the α -channel, but suggests that the $S(0)$ in the γ -channel may be smaller than previously thought. Using these values, the ratio $S(0)_\gamma:S(0)_\alpha$ is smaller than previously thought (see Eq. 5.1).

$$\frac{S(0)_\gamma}{S(0)_{\alpha_0}} = \frac{50 \times 10^{-3}}{68.0} = \frac{1}{1360} \quad (5.1)$$

This means that the second CNO cycle will operate once for every 1360 operations of the first cycle, instead of 1000 as was thought previously.

CNO energy production

The second CNO cycle operates at a slower rate than the first cycle as the $^{16}\text{O}(p,\gamma)^{17}\text{F}$ reaction is slower than the $^{14}\text{N}(p,\gamma)^{15}\text{O}$ at stellar energies. If, as this result suggests, more catalytic material remains in the first cycle the overall energy production of the CNO multi-cycle will increase marginally.

Stellar evolution

Detailed network calculations are needed to understand the affect of the changes of these cross-sections will have on stellar evolution and on the production of isotopes such as ^{16}O and ^{17}O (see Ref. [1]).

In a similar way to the $^{14}\text{N}(p,\gamma)^{15}\text{O}$ ground state transition, it is the interference between several contributions which determines the low energy S-factor. In this case there is more constraint placed on the low energy S-factor from the data between the resonances. This is where the interference is strongest, and furthermore the data points have much smaller errors than those at low energies.

Bibliography

- [1] C. E. Rolfs and W. S. Rodney. *Cauldrons in the Cosmos*. The University of Chicago Press, 1988.
- [2] A. M. Lane and R. G. Thomas. R-matrix Theory of Nuclear Reactions. *Reviews of Modern Physics*, 20:257, 1958.
- [3] G. Breit and E. Wigner. Capture of slow neutrons. *Physical Review*, 49:519–531, 1936.
- [4] P. F. Bertone, A. E. Champagne, D. C. Powell, C. Illiadis, S. E. Hale, and V. Y. Hansper. Lifetime of the 6973-keV State in ^{15}O . *Physical Review Letters*, 87:152501, 2001.
- [5] E. W. Vogt. Theory of Low Energy Nuclear Reactions. *Modern Physics*, 34:723, 1962.
- [6] K. S. Krane. *Introductory Nuclear Physics*. John Wiley & Sons, 1987.
- [7] C. Ruiz, T. Davinson, F. Sarazin, I. Roberts, A. Robinson, P. J. Woods, L. Buchmann, A. C. Shotton, P. Walden, N. M. Clarke, A. A. Chen, B. R. Fulton, D. Groombridge, J. Pearson, and A. S. Murphy. Multichannel R-matrix analysis of elastic and inelastic resonances in the $^{21}\text{Na}+p$ compound system. *Physical Review C*, 71:025802, 2005.
- [8] C. R. Brune. Alternative parametrization of R-matrix theory. *Physical Review C*, 66:044611, 2002.
- [9] C. Angulo and P. Descouvemont. The $^{14}\text{N}(p,\gamma)^{15}\text{O}$ low-energy S-factor. *Nuclear Physics A*, 690:755–768, 2001.
- [10] R. F. Christy and I. Duck. γ -Rays from Extranuclear Direct Capture Process. *Nuclear Physics*, 24:89–101, 1960.
- [11] T. A. Tomborello and P. D. Parker. Direct-Capture Model for the $\text{He}^3(\alpha,\gamma)\text{Be}^7$ and $\text{T}^3(\alpha,\gamma)\text{Li}^7$ Reactions. *Physical Review*, 131:2582, 1963.
- [12] C. Rolfs. Spectroscopic Factors from Radiative Capture Reactions. *Nuclear Physics A*, 217:29–70, 1973.
- [13] F. C. Barker and T. Kajino. The $^{12}(\alpha,\gamma)^{16}\text{O}$ Cross Section at Low Energies. *Australian Journal of Physics*, 44:369–396, 1991.

- [14] F. James. *Minuit: Function Minimization and Error Analysis*, 94.1 edition.
- [15] P. Descouvemont. Astrophysica for Windows: a PC software for Nuclear Astrophysics. *Nuclear Physics A*, 688:557c–559c, 2001.
- [16] A. Formicola, G. Imbriani, H. Constantini, C. Angulo, D. Bemmerer, R. Bonetti, C. Brogгинi, P. Convisiero, J. Cruz, P. Descouvemont, Z Fülöp, G. Gervino, A. Guglielmetti, C. Gustavino, G. Gyürky, A. P. Jesus, M. Junker, A. Lemut, R. Menegazzo, P. Prati, V. Roca, C. Rolfs, M. Romano, C. Rossi Alvarez, F. Schümann, E. Somorjai, O. Straniero, F. Strieder, F. Terrasi, H. P. Trautvetter, A. Vomiero, and S. Zavatarelli. Astrophysical S-factor of $^{14}\text{N}(p,\gamma)^{15}\text{O}$. *Physics Letters B*, 591:61, 2004.
- [17] R. C. Runkle, A. E. Champagne, C. Angulo, C. Fox, C. Illiadis, R. Longland, and J Pollanen. Direct Measurement of the $^{14}\text{N}(p,\gamma)^{15}\text{O}$ S-Factor. *Physical Review Letters*, 94:082503, 2005.
- [18] G. Imbriani, H. Constantini, A. Formicola, A. Vomiero, C. Angulo, D. Bemmerer, R. Bonetti, C. Brogгинi, F. Confortola, P. Convisiero, J. Cruz, P. Descouvemont, Z Fülöp, G. Gervino, A. Guglielmetti, C. Gustavino, G. Gyürky, A. P. Jesus, M. Junker, J. N. Klug, A. Lemut, R. Menegazzo, P. Prati, V. Roca, C. Rolfs, M. Romano, C. Rossi Alvarez, F. Schümann, D. Schürmann, E. Somorjai, O. Straniero, F. Strieder, F. Terrasi, and H. P. Trautvetter. S-factor of $^{14}\text{N}(p,\gamma)^{15}\text{O}$ at astrophysical energies. *European Physical Journal A - Hadrons and Nuclei*, 25:455–466, 2005.
- [19] E. G. Adelberger, S. M. Austin, J. N. Bahcall, A. B. Balantekin, G. Bogaert, L. S. Brown, L. Buchmann, F. E. Cecil, A. E. Champagne, L. de Braekeleer, C. A. Duba, S. R. Elliott, M. Gai, G. Goldring, A. Gruzinov, W. C. Haxton, K. M. Heeger, E. Hensley, C. W. Johnson, M. Kamionkowski, R. W. Kavanagh, S. E. Koonin, K. Kubodera, K. Langanke, T. Motobayashi, V. Pandharipande, P. Parker, R. G. H. Robertson, C. Rolfs, R. F. Sawyer, N. Shaviv, T. D. Shoppa, K. A. Snover, E. Swanson, R. E. Tribble, S. Turck-Chieze, and J. F. Wilkerson. Solar Fusion Cross Sections. *Reviews of Modern Physics*, 70:1265–1291, 1998.
- [20] U. Schröder, H. W. Becker, G. Bogaert, J. Görres, C. Rolfs, H. P. Trautvetter, R. E. Azuma, C. Campbell, J. D. King, and J. Vise. Stellar reaction rate of $^{14}\text{N}(p,\gamma)^{15}\text{O}$ and hydrogen burning in massive stars. *Nuclear Physics A*, 467:240, 1987.
- [21] H.-P. Trautvetter. Personal Communication.
- [22] C. Angulo, A. E. Champagne, and H. P. Trautvetter. R-matrix analysis of the $^{14}\text{N}(p,\gamma)^{15}\text{O}$ Astrophysical S-factor. *Nuclear Physics A*, 758:391c–394c, 2005.
- [23] J. Klug et. al. *in preparation*.
- [24] S. Bashkin, R. R. Carlson, and R. A. Douglas. Cross Section for Elastic Scattering of Protons by N^{14} . *Physical Review*, 114:1552–1553, 1959.

- [25] A. J. Ferguson, R. L. Clarke, H. E. Gove, and J. T. Sample. Elastic Scattering of Protons by Nitrogen. Atomic Energy of Canada Report PD-261, 1956.
- [26] G. W. Tautfest and S. Rubin. Elastic Scattering of Protons from B^{11} and N^{14} . *Physical Review*, 103:196–199, 1956.
- [27] F. B. Hagedorn, F. S. Mozer, T. S. Webb, W. A. Fowler, and C. C. Lauritsen. Elastic Scattering of Protons by N^{14} . *Physical Review*, 105:219–226, 1957.
- [28] A. Champagne and P. Betone. Personal Communication.
- [29] G. Imbriani, H. Constantini, A. Formicola, D. Bemmerer, R. Bonetti, C. Brogini, P. Convisiero, J. Cruz, Z Fülöp, G. Gervino, A. Guglielmetti, C. Gustavino, G. Gyürky, A. P. Jesus, M. Junker, A. Lemut, R. Menegazzo, P. Prati, V. Roca, C. Rolfs, M. Romano, C. Rossi Alvarez, F. Schümann, E. Somorjai, O. Straniero, F. Strieder, F. Terrasi, H. P. Trautvetter, A. Vomiero, and S. Zavatarelli. The Bottleneck of the CNO burning and the age of Globular Clusters. *Astronomy and Astrophysics*, 2004.
- [30] D. M. Bremmerer. *Experimental study of the $^{14}N(p,\gamma)^{15}O$ reaction at energies far below the Coulomb barrier*. PhD thesis, der Technischen Universität Berlin, 2004.
- [31] M. H. Jones and R. J. A. Lambourne. *An Introduction to Galaxies and Cosmology*. Cambridge, 2004.
- [32] S. Ryan. *The Life and Death of Stars*. Bath Press, 2002.
- [33] B. W. Carroll and D. A. Ostlie. *An Introduction to Modern Astrophysics*. Addison Wesley Longman, 1996.
- [34] S. Degl’Inocenti, G. Fiorentini, B. Ricci, and F. L. Villante. The $^{14}N(p,\gamma)^{15}O$ reaction, solar neutrinos and the age of globular clusters. *Physics Letters B* 2004, 590:13–20, 2004.
- [35] C. Rolfs and W. S. Rodney. Proton Capture by ^{15}N at stellar Energies. *Nuclear Physics A*, 235:450, 1974.
- [36] A. Schardt, W. Fowler, and C. C. Lauritsen. The disintegration of ^{15}N by protons. *Physical Review*, 86:527, 1952.
- [37] J. L. Zyskind and P. D. Parker. Remeasurement of the low-energy cross section for the $^{15}N(p,\alpha_0)^{12}C$ reaction. *Nuclear Physics A*, 320:404, 1979.
- [38] A. Redder, H. W. Becker, H. Lorenz-Wirzba, C. Rolfs, P. Schmalbrock, and H. P. Trautvetter. The $^{15}N(p,\alpha_0)^{12}C$ Reaction at Stellar Energies. *Zeitschrift für Physik A*, 305:325, 1982.
- [39] F. Brochard, P. Chevallier, D. Disdier, V. Rauch, and F. Scheibling. Étude des Désexcitations Électromagnétiques des Niveaux 1- Situes A 12,44 et 13,09 MeV dans le Noyau ^{16}O . *Le Journal de Physique*, 34:363–367, 1973.
- [40] D. F. Hebbard. Proton Capture by N^{15} . *Nuclear Physics*, 15:289–315, 1960.

Appendix A

Corrections to Lane and Thomas

R-matrix theory

There were some errors in the R-matrix theory as prescribed by A. M. Lane and R. G. Thomas in Ref. [2]. Corrections were derived by C. Ugalde.

A.1 C. Ugalde

The T in the sum of the third component is conjugated and a kronecker delta is added to the third term.

$$\begin{aligned} (2s+1) \frac{k_\alpha^2}{\pi} d\sigma_{\alpha's',\alpha s} d\Omega_{\alpha'} &= (2s+1) |C_{\alpha'}(\theta_{\alpha'})|^2 \delta_{\alpha's',\alpha s} \\ &+ \frac{1}{\pi} \sum_L B_L(\alpha's',\alpha s) P_L(\cos(\theta_{\alpha'})) + \delta_{\alpha's'l',\alpha sl} (4\pi)^{-1/2} \\ &\times \sum_{Jl} (2J+1) 2\text{Re} [i(T_{\alpha's'l',\alpha sl}^J)^* C_{\alpha'}(\theta_{\alpha'}) P_l(\cos(\theta_{\alpha'}))] \end{aligned} \quad (\text{A.1})$$

A.2 L. Buchmann

An alternative correction was published in Ref. [7]. They state that *'Lane and Thomas omitted the Kronecker delta in the third component of the sum, and by not conjugating*

the T in the same term, they had a definite error'.

$$\begin{aligned}
(2s+1)\frac{k_\alpha^2}{\pi}d\sigma_{\alpha's',\alpha s}d\Omega_{\alpha'} &= (2s+1)|C_{\alpha'}(\theta_{\alpha'})|^2\delta_{\alpha's',\alpha s} \\
&+ \frac{1}{\pi}\sum_L B_L(\alpha's',\alpha s)P_L(\cos(\theta_{\alpha'})) - \delta_{\alpha's',\alpha s}(4\pi)^{-1/2} \\
&\times \sum_{Jl} (2J+1)2\text{Re}[i(T_{\alpha's'l',\alpha sl}^J)^*C_{\alpha'}(\theta_{\alpha'})P_l(\cos(\theta_{\alpha'}))](A.2)
\end{aligned}$$

Note that whilst the text of Ref. [7] mentions the Kronecker delta and the conjugation of T , it does not mention that sign of the interference (third) term is changed. The indices of the kronecker delta do not agree with those of the Claudio Ugalde correction (Eq. A.1). However, if $\alpha = \alpha'$ and $s = s'$ then l must equal l' .

Appendix B

NuclearInput.for

NuclearInput.for is the computer code used to create nuclear input files for use with AZURE.

```
c -----
c AZURE Input File Creation Program   July 2005
c Dick Azuma and Ed Simpson
c -----

PROGRAM NuclearInput
IMPLICIT none
INCLUDE 'memory.h'      !MEMORY.h MUST INCLUDE SUFFICIENT MIR AND MAA!!!!!!
INTEGER aa, ir, rclines,i,ii,NJpi,maindo, J2, nlevelsperjpi
INTEGER nRchannels,Lid!, pch, smin, smax  --> declared in memory.h
REAL*8 Rchannels(1:maa,1:mir,1:17), rctemp(1:17)
CHARACTER*15 junk1
CHARACTER*6 rlttemp(1:2), Rlabel(1:maa,1:mir,1:2)

REAL*8 Jpigroup(1:100,1:3), energylevel(1:100,2),slarray(1:100,5)
INTEGER nlevels, is, il, lmax, aamax,  irmax(maa), nch, nl, nlmax
INTEGER nlmax, mpolemin, mpolemax, chp, paritychange, naa, ie

c There is an array called Jpigroup; it will contain:
c   (Jpi Group Number)      J      pi

c Another array called levels which stores energy level info referenced to Jpi group
c   Energy Level      Jpi Group Number

c Another array called slarray holds the s-l combinations for each Jpi
c   Jpi Group Number      aa      R      s      l
c Each Jpi group number can correspond to multiple s-l combinations
c

c The J-pi Group number is taken from "maindo"

c To start with, all J-pi Groups will have ALL reaction channels... for now...

PRINT*, 'NOTE: the program may not work correctly if the same Jpi
+is entered multiple times'

c -----
c Section 0: Stating values for certain parameters
c -----
nlevels=0
aamax=0
irmax=0
slarray=0
nch=0
NJpi=0
naa=0

OPEN(10,file='configuration.dat')
```

```

READ(10,*) junk1
DO i=1,4
  READ(10,*) junk1
END DO
READ(10,*) lmax
READ(10,*) nlmax
READ(10,*) nLlmax
CLOSE(10)

c
c -----
c Section 1: Read in reaction channel parameters
c           from Rchannels.par. This must be created
c           before running this program
c -----

OPEN(10,file='Rchannels.par')
! 1 2 3 4 5 6 7 8 9 10 11 12 13 14 15 16 17
!Alpha R Jlf Plf Jhf Phf Efx Ml Mh Zl Z2 Qin Qout Ji Pi Ei g_type Reaction
! I1 I2 R1 I3 R2 I4 R3 R4 R5 I5 I6 R6 R7 R8 I7 R9 I8

READ(10,*) junk1
READ(10,*) rclines
IF(rclines.gt.mir) WRITE(6,'(/a/)') WARNING: CHECK memory.h HAS C
+ORRECT VALUES FOR maa AND mir. STRANGE ERRORS OFTEN RESULT FROM I
+NCORRECT memory.h FILES!!'
DO i=1, rclines
  READ(10,*) (rctemp(ii),ii=1,17),(rltemp(ii),ii=1,2) !Improve READ in FORMAT
  aa=NINT(rctemp(1))
  ir=NINT(rctemp(2))
  Rlabel(aa,ir,1)=rltemp(1)
  Rlabel(aa,ir,2)=rltemp(2)
  IF(aa.gt.aamax) aamax=aa
  IF(ir.gt.irmax(aa)) irmax(aa)=ir

  DO ii=1,17
    aa=NINT(rctemp(1))
    ir=NINT(rctemp(2))
    Rchannels(aa,ir,ii)=rctemp(ii)
  END DO
END DO

CLOSE(10)

c
c -----
c BEGINNING OF MAIN PROGRAM LOOP
c -----

DO maindo=1,100 !---> Basically a loop over
! Jpi-groups

c
c -----
c Section 2: The user specifies the Jpi group,
c           by giving the program aa, Jpi,
c           nlevels/Jpi Group, and the R-channels
c           used by this group.
c -----
+ PRINT*, 'What is the J value (i.e. 0.5, 1.5) of this J-pi group?'
+ (<0 to end)
READ(5,*) Jpigroup(maindo,1)
IF(Jpigroup(maindo,1).lt.0) GOTO 1914
1916 PRINT*, 'What is the parity of this J-pi group? '
READ(5,*) Jpigroup(maindo,2)
IF(NINT(Jpigroup(maindo,2)).ne.-1.AND.
+ NINT(Jpigroup(maindo,2)).ne.1) THEN
  PRINT*, 'Invalid parity entered. Enter +1 or -1.'
  GOTO 1916
END IF
PRINT*, 'How many levels in this Jpi group? '
READ(5,*) nlevelsperjpi

c
c -----
c Section 3: User inputs the energy levels for
c           the nlevelsperJpi that this Jpi
c           group has. Once done, the program
c           loops back to Section 2 Jpi group
c           can be dealt with.
c -----
PRINT*, Jpigroup(maindo,1)

WRITE(6,1915) 'For the ',Jpigroup(maindo,1),
+ Jpigroup(maindo,2),'Please enter',nlevelsperjpi,'levels'
1915 FORMAT(a,2f5.1,a,i3,a)
DO i=nlevels+1, (nlevels+nlevelsperjpi)
  PRINT*, 'Energy Level ',i,'= '
  READ(5,*) energylevel(i,1)
  energylevel(i,2)=maindo
END DO
nlevels=nlevels+nlevelsperjpi

c
c -----
c Section 4: The program calculates the appropriate
c           s-l channels for the specified Jpi-group
c           (this is taken directly from the same
c           calculation in AZURE).
c -----
DO aa=1, aamax

```

```

DO ir=1, irmax(aa)
c -----
c RESONANCE PARTICLE DECAY CHANNELS
IF(NINT(Rchannels(aa,ir,17)).eq.0) THEN
smin=ABS(2*Rchannels(aa,ir,3)-2*Rchannels(aa,ir,5))
smax=ABS(2*Rchannels(aa,ir,3)+2*Rchannels(aa,ir,5))
pch=0
+ IF(Rchannels(aa,ir,4)*Rchannels(aa,ir,6)*Jpigroup(maindo,2)
.lt.0) pch=2
DO is=smin,smax,2
nl=0
DO il=pch,lmax,4
+ IF((is+il).ge.2*Jpigroup(maindo,1).AND.
ABS(is-il).le.2*Jpigroup(maindo,1)) THEN
nl=nl+1
IF(nl.gt.nlmax) GOTO 1917
nch=nch+1
slarray(nch,1)=maindo
slarray(nch,2)=aa
slarray(nch,3)=ir
slarray(nch,4)=is
slarray(nch,5)=il
END IF
END DO
1917 CONTINUE
END DO
END IF

c -----
c RESONANCE GAMMA CAPTURE: PRIMARIES
IF(NINT(Rchannels(aa,ir,17)).eq.10) THEN
chp=0
mpolemin=2*ABS(Jpigroup(maindo,1)-Rchannels(aa,ir,5))
mpolemax=2*ABS(Jpigroup(maindo,1)+Rchannels(aa,ir,5))
pch=Jpigroup(maindo,2)*Rchannels(aa,ir,6)
DO il=mpolemin,mpolemax,2
IF(il.gt.0) THEN
chp=chp+1
IF(chp.gt.nlmax) GOTO 1918
nch=nch+1
slarray(nch,1)=maindo
slarray(nch,2)=aa
slarray(nch,3)=ir
slarray(nch,4)=chp
slarray(nch,5)=il
paritychange=(-1)**(il/2)
IF(paritychange.eq.pch) THEN
GOTO 1918
ELSE
END IF
END IF
END DO
1918 CONTINUE

c -----
c RESONANCE GAMMA CAPTURE: SECONDARIES ????
----> To be done (REA??)
IF(NINT(Rchannels(aa,ir,17)).ne.10.AND.
+NINT(Rchannels(aa,ir,17)).ne.0) THEN
PRINT*, 'WARNING: Secondary gammas not yet implimented.'
PRINT*, 's-l channels will not be calculated for secondary
+ gammas.'
END IF

c -----
c DIRECT CAPTURE: PRIMARIES ?????
----> To be done (REA??)

END DO !End of ir loop
END DO

c -----
c END OF MAIN DO LOOP
c -----
NJpi=NJpi+1
END DO !end of Jpi loop

c -----
c Section 5: Having got all the information it
c needs, the program writes out the
c input file in full. AZURE requires
c modifications to deal with the new
c format.
c -----

1914 CONTINUE

c PRINT*, 'S-L output', nch
c DO is=1,nch
c WRITE(6,'(4f5.1)') (slarray(is,il),il=1,4)
c END DO
c OPEN(12,file='nucfileoutput.txt')
c WRITE(12,*) 'Jc Pc Ecx aa R s l Lid Y/N Gam Jlf

```

```

+ Plf Jhf Phf Efx Ml Mh Z1 Z2 Qin Qout Ji Pi Ei
+ g_type Reaction'
Lid=1
PRINT*, 'aamax=', aamax
DO aa=1, aamax !loop over aa
DO maindo=1,NJpi !loop over Jpi Groups
DO ie=1,nlevels !loop over energy levels
IF(energylevel(ie,2).eq.maindo) THEN !Selects appropriate energy levels
DO i=1,nch !loop over s-l channels
IF(slarray(i,1).eq.maindo.AND.slarray(i,2).eq.aa) THEN
ir=slarray(i,3)
WRITE(12,1066) Jpigroup(maindo,1),NINT(Jpigroup(maindo,2)),
+energylevel(ie,1),aa,ir,NINT(slarray(i,4)),NINT(slarray(i,5)),
+Lid,' 1', 0.00000',Rchannels(aa,ir,3),NINT(Rchannels(aa,ir,4)),
+Rchannels(aa,ir,5),NINT(Rchannels(aa,ir,6)),Rchannels(aa,ir,7),
+Rchannels(aa,ir,8),Rchannels(aa,ir,9),NINT(Rchannels(aa,ir,10)),
+NINT(Rchannels(aa,ir,11)),Rchannels(aa,ir,12),Rchannels(aa,ir,13),
+Rchannels(aa,ir,14),NINT(Rchannels(aa,ir,15)),Rchannels(aa,ir,16),
+NINT(Rchannels(aa,ir,17)),' ',Rlabel(aa,ir,1),' ',Rlabel(aa,ir,2)
END IF
END DO
WRITE(12,*) ''
Lid=Lid+1
END IF
END DO
END DO
END DO
1066 FORMAT(f4.1,i3,f8.4,5i3,a,a,2(f4.1,i3),f7.4,2f5.1,2i3,2f7.3,f4.1,
+i3,f7.3,i3,a,1a5,a,1a5)
END PROGRAM

```

Below is a sample Rchannels.par file required by the NuclearInput.for program. It must be made by hand by the user, though it is fairly simple.

Alpha R	Jlf	Plf	Jhf	Phf	Efx	Ml	Mh	Z1	Z2	Qin	Qout	Ji	Pi	Ei	g_type	Reaction	
7																	
1	1	0.5	1	1.0	1	0.000	1.0	14.0	1	7	7.2971	7.2971	0.0	1	0.0	0	14N(p,p)14N
1	2	0.0	1	0.5	-1	0.000	0.0	15.0	0	8	7.2971	0.0000	0.5	-1	0.0	10	14N(p,g)15O
1	3	0.0	1	1.5	1	6.793	0.0	15.0	0	8	7.2971	0.0000	1.5	1	6.793	10	14N(p,g)15O
1	4	0.0	1	1.5	-1	6.180	0.0	15.0	0	8	7.2971	0.0000	1.5	-1	6.18	10	14N(p,g)15O
1	5	0.0	1	0.5	1	5.183	0.0	15.0	0	8	7.2971	0.0000	0.5	1	5.183	10	14N(p,g)15O
1	6	0.0	1	2.5	1	5.241	0.0	15.0	0	8	7.2971	0.0000	2.5	1	5.241	10	14N(p,g)15O
1	7	0.0	1	0.5	1	7.557	0.0	15.0	0	8	7.2971	0.0000	0.5	1	7.557	10	14N(p,g)15O

Appendix C

BarkerKajino.for

BarkerKajino.for is a development code, used to calculate the energy dependence of the contributions to the U-matrix elements coming from the nonresonant channel contributions, as described in Ref. [13]. Many thanks to H. Costantini for checking this code.

```
c-----
c   Barker and Kajino Direct Capture
c   Development Code 21/11/2005
c-----
PROGRAM BARKERKajino
IMPLICIT none

INTEGER :: i,factorial, fact1
INTEGER :: ie,nie,r,nrad
INTEGER :: bigL,li,lf,flag
INTEGER, PARAMETER :: z1=7,z2=1,m1=14,m2=1

REAL*8 :: e0,r0,dele,delr,ecm,rad
REAL*8 :: redmass,kin,kout,sigma,Jlp
REAL*8 :: xl,eta,rho,fla,fpla,gla,gpla,pene,phiHS,omega
REAL*8 :: fl,fpl,gl,gpl,whitr,whita,rhoa,etaa
REAL*8 :: integral1,integral2,integral3,integral
REAL*8 :: rhowhit,etawhit,rhowhita,add,percent,Lfactor
REAL*8 :: ebarL,N,Nintegral1,Nintegral2,Nintegral3,Nsum,Nintegral
REAL*8 :: specfact,lowradius,whitratio
REAL*8, PARAMETER :: BE=7.3

COMPLEX*8 :: icmp,Umatrix

c-----
c   Setup and Physical Parameters
c-----
OPEN(10,file='BKXS.txt')
OPEN(11,file='BKradius.txt')
OPEN(12,file='radiusinvestigation.txt')

bigL=1
xl=0
li=0
lf=1
specfact=1.0

nie=50
e0=0.05
dele=0.05
nrad=500
r0=5.5
delr=0.1

redmass=(REAL(m1)*REAL(m2)/(REAL(m1)+REAL(m2)))
icmp=(0.0,1.0)
```

```

flag=1
-----
c
c   Calculation of energy independent factors
c
-----

fact1=factorial(2*bigL+1)
Lfactor=((bigL+1)*(2*bigL+1)/bigL)**0.5)*
+(1.0/(factorial(fact1)))

!ebarL - CHECK THIS
ebarL=redmass*((REAL(z2)/REAL(m2))
+
+((-1.0)**bigL)*(REAL(z1)/REAL(m1)))!*1.6*10**(-19)
-----
c
c   Begining of energy loop
c
-----

DO ie=0,nie
ecm=e0+ie*dele

rhoa=0.2187343d0*r0*sqrt(redmass*ecm)
rhowhita=0.2187343d0*r0*sqrt(redmass*BE)

etaa=0.158052d0*REAL(z1)*REAL(z2)*sqrt(redmass/ecm)
etawhit=0.158052d0*REAL(z1)*REAL(z2)*sqrt(redmass/BE)

eta=0.158052d0*REAL(z1)*REAL(z2)*sqrt(redmass/ecm)

CALL coull(xl,etaa,rhoa,fla,fpla,gl,gpla)

pene=rhoa/((fla**2)+(gl**2))

phiHS=atan(fla/gla)
IF(PhiHS.gt.0) flag=0
IF(PhiHS.lt.0.AND.flag.eq.0) THEN
  add=add+3.1415
  flag=1
END IF
phiHS=phiHS+add

omega=0
IF(li.gt.0) THEN
  DO i=1,li
    omega=omega+atan(etaa/i)
  END DO
ELSEIF(li.eq.0) THEN
  omega=0
END IF

kin=(4.8196*redmass*ecm)**0.5
kout=(ecm+BE)
-----
c
c   Begining of radius loop
c
-----

Jlp=0
Nsum=0

DO r=0,nrad

  rad=r0+REAL(r)*delr

  rho=0.2187343d0*rad*sqrt(redmass*ecm)
  rhowhit=0.2187343d0*rad*sqrt(redmass*BE)
  CALL coull(xl,eta,rho,fl,fpl,gl,gpl)
  CALL whitt(lf,etawhit,rhowhita,whita)
  CALL whitt(lf,etawhit,rhowhit,whitr)
  integral1=(whitr/whita)*((fl/fla)-(gl/gla))*(rad**bigL)
  Nintegral1=(whitr/whita)**2

  whitratio=whitr/whita

  rho=0.2187343d0*(rad+0.5*delr)*sqrt(redmass*ecm)
  rhowhit=0.2187343d0*(rad+0.5*delr)*sqrt(redmass*BE)
  CALL coull(xl,eta,rho,fl,fpl,gl,gpl)
  CALL whitt(lf,etawhit,rhowhita,whita)
  CALL whitt(lf,etawhit,rhowhit,whitr)
  integral2=(whitr/whita)*((fl/fla)-(gl/gla))*
+
+((rad+0.5*delr)**bigL)
  Nintegral2=(whitr/whita)**2

  rho=0.2187343d0*(rad+delr)*sqrt(redmass*ecm)
  rhowhit=0.2187343d0*(rad+delr)*sqrt(redmass*BE)
  CALL coull(xl,eta,rho,fl,fpl,gl,gpl)
  CALL whitt(lf,etawhit,rhowhita,whita)
  CALL whitt(lf,etawhit,rhowhit,whitr)
  integral3=(whitr/whita)*((fl/fla)-(gl/gla))*((rad+delr)**bigL)
  Nintegral3=(whitr/whita)**2

!Simpson's Integration: CHECK!

integral=(delr/6)*(integral1+4*integral2+integral3)
Nintegral=(delr/6)*(Nintegral1+4*Nintegral2+Nintegral3)

```

```

Nsum=Nsum+Nintegral
Jlp=Jlp+integral/(r0**(bigL+1))

!Estimates of Rfinal... when deltaJlp falls below 0.00001*Jlp for 20 consecutive fm

c      IF(ABS(integral/Jlp).gt.0.00001) lowradius=0
c      IF(ABS(integral/Jlp).lt.0.00001) lowradius=lowradius+deler
c      IF(lowradius.gt.20) GOTO 1984

      WRITE(11,'(5e15.5)') ecm,rad,Jlp

      END DO

c1984  WRITE(12,'(5e15.5)') ecm,be,rad
c      WRITE(6,'(5f15.5)') ecm,rad

      WRITE(11,*) ''
      WRITE(11,*) ''

      N=1.0/(1.0+((2*specfact**2)/r0)*Nsum)

c-----
c      Start of U-matrix (end of radius DO loop)
c-----

      Umatrix=fla*gla*Jlp
+      *(r0/rhoa)!*Lfactor*ebarL*(N**0.5)*specfact
+      *(-icmp*exp(icmp*(omega-phiHS)))
+      *2*(kout**(bigL+0.5))*(pene**0.5)
+      *(icmp**(li+bigL-1f)) !Complex bit needs inclusion WITH C-G and Racach??
      sigma=(3.1415/kin**2)*(ABS(Umatrix))**2

      WRITE(10,'(6e15.5)') ecm,sigma
+      *exp(0.99307*z1*z2*((redmass/ecm)**0.5))*ecm

      IF(MOD(ie,10).eq.0)
+      WRITE(6,'(1i5,a)') NINT(100*REAL(ie)/REAL(nie)), '%'

      END DO

      CLOSE(10)
      CLOSE(11)
      CLOSE(12)

      END PROGRAM

c-----
c      Factorial Function
c-----

      INTEGER FUNCTION factorial(x)
      IMPLICIT none
      INTEGER :: x,i

      factorial=1
      DO i=0,100
c      PRINT*,i,x,factorial
      IF(x.eq.i) GOTO 101
      factorial=factorial*(x-i)
      x=x-1
      END DO
101  CONTINUE
      END FUNCTION

```

Appendix D

Tables of fitted parameters

The fitted reduced width amplitudes for typical $^{14}\text{N}(p,\gamma)^{15}\text{O}$ fits are shown in the Table D.1.

Level Energy (MeV)	J^π	α	s	l	$\gamma_{r.w.a.}$ (MeV $^{1/2}$)
7.556	1/2 ⁺	p	1/2	0	0.840
		p	3/2	2	0.00
		γ_0	1	1	6.13×10^{-7}
		$\gamma_{6.18}$	1	1	-7.00×10^{-5}
8.744	1/2 ⁺	p	1/2	0	0.173
		p	3/2	2	0.00
		γ_0	1	1	0.00
		$\gamma_{6.18}$	1	1	-4.00×10^{-5}
17.297	1/2 ⁺	p	1/2	0	0.147
		p	3/2	2	-0.200
		γ_0	1	1	2.90×10^{-5}
		$\gamma_{6.18}$	1	1	9.26×10^{-3}
6.79	3/2 ⁺	p	1/2	2	0.269
		p	3/2	0	-0.737
		p	3/2	2	-0.19
		γ_0	1	1	3.92×10^{-5}
		$\gamma_{6.18}$	1	1	0.00
8.284	3/2 ⁺	p	1/2	2	0.00
		p	3/2	0	0.0673
		p	3/2	2	0.00
		γ_0	1	1	-5.00×10^{-6}
		$\gamma_{6.18}$	1	1	1.57×10^{-5}
9.484	3/2 ⁺	p	1/2	2	-0.310
		p	3/2	0	0.373
		p	3/2	2	0.219
		γ_0	1	1	-3.10×10^{-5}
		$\gamma_{6.18}$	1	1	0.00
17.297	3/2 ⁺	p	1/2	2	0.110
		p	3/2	0	0.992
		p	3/2	2	-0.0780
		γ_0	1	1	-3.3×10^{-4}
		$\gamma_{6.18}$	1	1	5.01×10^{-4}

Table D.1: Fitted reduced width amplitudes for the $^{14}\text{N}(p,\gamma)^{15}\text{O}$ reactions.

The fitted reduced width amplitudes for typical $^{15}\text{N}(p,\gamma)^{16}\text{O}$ and $^{15}\text{N}(p,\alpha_0)^{12}\text{C}$ fits are shown in Table D.2.

Level Energy (MeV)	J^π	α	s	l	$\gamma_{r.w.a.}$ (MeV $^{1/2}$)
13.664	1^+	p	0	1	-0.2
		p	1	2	0.53144
		γ_0	1	1	0.108×10^{-4}
12.44	1^-	p	0	0	0.210
		p	1	2	0.00
		γ_0	1	1	0.487×10^{-4}
		α_0	0	1	0.1325
13.09	1^-	p	0	0	0.495
		p	1	2	0.00
		γ_0	1	1	0.409×10^{-4}
		α_0	0	1	-0.020
27.128	1^-	p	0	0	1.83
		p	1	2	0.00
		γ_0	1	1	0.229×10^{-3}
		α_0	0	1	0.090
13.29	3^-	p	0	0	0.134
		p	1	2	0.00
		γ_0	1	1	0.00
		α_0	0	3	0.137
27.128	3^-	p	0	0	0.851
		p	1	2	0.0022
		γ_0	1	1	-0.25×10^{-5}
		α_0	0	3	-0.02

Table D.2: Fitted reduced width amplitudes for the $^{15}\text{N}(p,\gamma)^{16}\text{O}$ and $^{15}\text{N}(p,\alpha_0)^{12}\text{C}$ reactions.